

Solid-state NMR investigation of phosphonic acid based proton conducting materials

**Dissertation
zur Erlangung des Grades
Doktor der Naturwissenschaften
im Promotionsfach Chemie**

**von Birgit Faßbender
geboren am 10. Januar 1983 in Mainz**

**am Fachbereich Chemie,
Pharmazie und Geowissenschaften
der Johannes Gutenberg-Universität Mainz**

Mainz, den 15. Dezember 2009

Die vorliegende Arbeit wurde von März 2007 bis Januar 2010 am Max-Planck-Institut für Polymerforschung in Mainz angefertigt.

Dekan:

Erster Berichterstatter:

Zweiter Berichterstatter:

Tag der mündlichen Prüfung: 22. Februar 2010

Contents

1	Introduction and Motivation	1
I	THEORETICAL BACKGROUND	5
2	Fundamentals of NMR spectroscopy	7
2.1	Theoretical background	7
2.1.1	ZEEMAN interaction	7
2.1.2	Chemical shielding (CS)	9
2.1.3	Dipole-Dipole interaction	9
2.1.4	Quadrupole interaction	10
2.1.5	Magic Angle Spinning (MAS)	11
2.2	Basic NMR experiments	13
2.2.1	The single-pulse experiment (SPE)	13
2.2.2	Echo experiments	14
2.2.3	Cross-polarisation (CP)	15
2.2.4	Heteronuclear dipole-dipole decoupling	16
2.2.5	Variable-temperature experiments: mobility of protons	17

2.3	Advanced experiments	19
2.3.1	Two dimensional spectra	19
2.3.2	Back-to-Back (BaBa)	19
2.3.3	Heteronuclear dipole-dipole recoupling	22
3	Fuel cells	25
3.1	Polymer electrolyte membrane fuel cell (PEMFC)	25
3.1.1	Direct methanol fuel cells (DMFC)	28
3.1.2	Alkaline fuel cells (AFC)	28
3.1.3	Phosphoric acid fuel cells (PAFC)	28
3.1.4	Molten carbonate fuel cells (MCFC)	29
3.2	Mechanisms of proton transport	30
II	RESULTS AND DISCUSSION	33
4	Phosphonic acid containing ionomers	35
4.1	Bulk proton conductivity	39
4.2	NMR characterization of the hydrogen bonds in the ionomers	44
4.3	Probing the microscopic proton mobility in the ionomers	47
4.3.1	Proton mobility revealed by ^1H DQ MAS NMR	47
4.3.2	Variable temperature ^1H MAS NMR experiments	49
4.3.3	Comparison of macroscopic and microscopic conductivity	55
4.3.4	Water uptake behavior of the HEXAGON	56
4.3.5	Deuteron NMR of the HEXAGON	62

4.3.6	^{31}P NMR studies of the ionomers	67
4.3.7	Dependency of ^{31}P CSA pattern on temperature and RH	74
4.4	Structural features of the ionomers	76
4.4.1	Structure determination using WAXS and computations	76
4.4.2	Temperature dependency of the SQUARE and the SCREW	81
4.4.3	^{31}P MAS NMR spectra of the SCREW	87
4.4.4	Solid state effect on ^1H MAS NMR spectra	91
4.4.5	Structural features from $^{13}\text{C}\{^1\text{H}\}$ MAS NMR	97
4.4.6	Mobility of the aromatic moiety using REPT-HDOR experiments	104
4.5	Conclusion	108
4.6	Spacer concept	110
4.6.1	Crystallinity of the polymers followed by ^{13}C MAS NMR and DSC	112
4.6.2	Local structure from ^1H and ^{31}P MAS NMR	114
4.7	Conclusions	123
5	Summary	125
	Appendix	130
A	Additional spectra	131
B	Methods	135
C	Pulse program	139
	List of Figures	149

List of Tables 153

Bibliography 155

List of abbreviations

AC	alternating current
ADMET	acyclic diene metathesis
BaBa	Back-to-Back double quantum coherence
CH ₃ OH	methanol
CA	carboxylic acid
CP	cross polarization
CPMD	Car-Parrinello molecular dynamics
D	dipolar constant
DC	direct current
δ_{iso}	isotropic chemical shift
D ₂ O	deuteriumoxid
DQ	double quantum
DQF	double quantum filter
DSC	differential scanning calorimetric
E_A	activation energy
IS	impedance spectroscopy
MAS	magic angle spinning
MMFF	molecular-mechanics force field
NICS	nucleus independent chemical shift
NMR	nuclear magnetic resonance
PAA	poly(acrylic acid)
P4VP	poly(4-vinylpyridine)
PE	poly(ethylene)
PE21-CA	poly[ethyl(21-carboxylic acid)]
PE21-Cl	poly[ethyl(21-chloride)]
PE21-Me	poly[ethyl(21-methyl)]
PE21-PA	poly[ethyl(21-phosphonic acid)]
PE9-CA	poly[ethyl(9-carboxylic acid)]
PE9-Cl	poly[ethyl(9-chloride)]
PE9-Me	poly[ethyl(9-methyl)]
PE9-PA	poly[ethyl(9-phosphonic acid)]
PhPA	phenyl phosphonic acid

PVBPA	poly(vinylbenzyl phosphonic acid)
PVPA	poly(vinyl phosphonic acid)
PVTz	poly(vinyl triazole)
REPT-HSQC	recoupled polarization transfer-heteronuclear single-quantum correlation
REPT-HDOR	recoupled polarization transfer-heteronuclear dipolar order
RFDR	radio frequency driven dipolar recoupling
RH	relative humidity
RT	room temperature
SQ	single quantum
SUPER	separation of undistorted powder patterns by effortless recoupling
T _m	melting point
T _g	glass transition point
TGA	thermal gravimetric analysis
VT	variable temperature

Chapter 1

Introduction and Motivation

Today, the limitation of fossil energy and a steadily increasing energy demand comprises a serious challenge. The need for renewable energy sources promotes fuel cells as a potential energy source, since they represent a clean alternative to current technologies based on fossil fuel resources. One of the most frequently used fuel cells is the polyelectrolyte membrane fuel cell (PEMFC), where the central component is its membrane. Currently, the state-of-the-art membrane material is Nafion[®], a perfluorinated polymer containing sulfonic acid groups. Due to its water based conduction, it is limited to a working temperature of $\sim 80^{\circ}\text{C}$. Since operation at higher temperatures can provide increased efficiency, new proton-conducting membranes should not be based on the diffusion of water, but rather on the structural diffusion of protons. To achieve this goal, several conceptual designs have been explored for almost anhydrous proton conducting polymeric electrolytes where a fair proton conductivity at temperatures higher than 130°C has been obtained. For proton conduction based on structural diffusion, phosphonic acid (PA) was used in several compounds as an immobilized phosphoric acid, e.g. in poly(vinylphosphonic acid) (PVPA) [MA 04, BINGOEL 06]. PA is considered to form a moderately strong but dynamic hydrogen-bonding network providing both P=O and P-OH as proton acceptor and proton donor groups. It is anticipated that the observable proton conductivity is based on a GROTHUSS-type mechanism (structural diffusion), where the protons are covalently bound to the matrix [GROTHUSS 75]. In general, the major requirements of PEMFC are high proton conductivity and good mechanical properties based on a low cost material. Further desired properties for application are a

low water diffusion and electroosmosis, low permeability of fuel and oxidant, and finally they should be environment-friendly.

Although a variety of different proton conducting membranes have been synthesized and investigated by manifold of techniques, including solid-state NMR, proton conduction at the molecular level is not yet fully understood. In particular, the relationship between macroscopic bulk proton conductivity and microscopic proton motion cannot be fully explained. Therefore, it is of great importance to relate structural and dynamic properties with respect to proton conductivity, e.g. by means of solid-state NMR and impedance spectroscopy, which will potentially allow for a more rational design of new proton conducting membranes.

This work aims at understanding of structural motifs and proton dynamics of promising proton conducting materials, which is of crucial importance to unravel the proton conduction mechanisms of PEMs. In particular, hydrogen bonding networks, local proton mobility, and molecular packing arrangements are studied by means of advanced solid-state NMR methods. High-resolution ^1H MAS NMR spectroscopy in particular provides useful information on dynamic hydrogen-bonding in solids including exchange of protogenic groups with solvents. Hydrogen bond networks are the key interaction investigated in this work and it plays an important role in chemical and biological systems [BRUNNER 98]. In particular, in proton conduction the hydrogen bond strength and mobility of the protons within PEMs can be affected by manifold parameters.

After a brief description of the solid-state NMR techniques that are used in this thesis, an overview of fuel cells is presented in chapter 3. Subsequently, the main results of this thesis are discussed in chapter 4 and ???. In particular, chapter 4, analyzes the influence of *self-assembly* as well as the effect of *incorporated water* on both the proton conduction and mobility in rather crystalline ionomers. Notably, it was found that a high degree of local ordering is not favorable for structural diffusion in these compounds. Rather the observable bulk proton conduction is mainly based on incorporated water. In addition, chapter ??? explores the impact of the *acid-base* ratios on the proton conductivity of statistical poly (4-vinylpyridine) - poly(vinylbenzyl phosphonic acid) (PVBPA-P4VP) copolymers. Furthermore the effects of different *spacer* length in a polymer backbone on

the physical properties of the polymer are discussed. Finally, a summary of all results is provided in chapter 5.

Part I

THEORETICAL BACKGROUND

Chapter 2

Fundamentals of NMR spectroscopy

In 1945 Bloch and Purcell [BLOCH 46; PRUCELL 46] independently detected radio frequency signals generated by the nuclei of atoms. Over the last 60 years every endeavor has been made to use this effect efficiently. The technique developed continuously in hardware and software as much as in sophisticated experiments. Consequently, in modern chemistry, at universities and industry alike high resolution **nuclear magnetic resonance** (NMR) is indispensable to determine both structure and purity of molecules. In particular, liquid-state NMR provides fast and clear results in daily lab praxis. Additionally, nowadays solid-state NMR is a well established technique for probing both structure and dynamics of materials [SCHMIDT-ROHR 94, DUER 04, LAWS 02].

2.1 Theoretical background

2.1.1 ZEEMAN interaction

All NMR visible atoms may be characterized by a nuclear spin quantum number $I \geq \frac{1}{2}$. Each nucleus is related to a magnetic dipole moment μ which is proportional to the *gyromagnetic ratio* γ , the Planck's constant \hbar and the quantum number as defined in equation 2.1.

$$\mu = \gamma\hbar I \quad (2.1)$$

Under the assumption that there is no interaction, spins of one nucleus are energetically identical. Placing them into a homogeneous magnetic field leads to a splitting into $(2I + 1)$ energy levels, if $I \neq 0$. The energy of this electromagnetic interactions can be described by the SCHRÖDINGER equation (2.2).

$$\frac{d}{dt} |\psi(t)\rangle = \frac{-i}{\hbar} \hat{H} |\psi(t)\rangle \quad (2.2)$$

Additionally, the Hamiltonian can be divided into the energies of different interactions, such as the external and internal. The ZEEMAN-effect \hat{H}_Z , depending on the external magnetic field and radio frequency interaction \hat{H}_{rf} represent the external interactions. Internal are the chemical shift \hat{H}_{cs} , dipole-dipole \hat{H}_{dd} and electric quadrupole \hat{H}_q interactions and finally the J-coupling \hat{H}_J which will not be discussed further, and are described in more detail in [LEVITT 01].

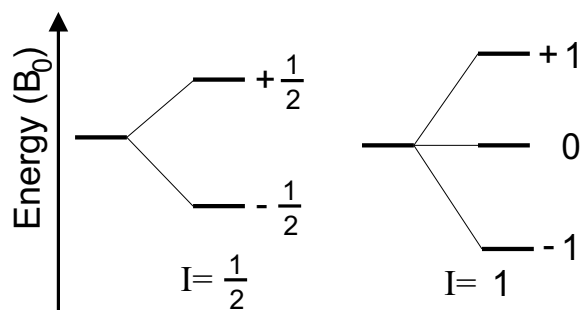


Figure 2.1: Energy level diagram illustrating the breakdown of nuclear spin degeneracy upon the application of a magnetic field.

All HAMILTONIANS represent interactions that may affect the equilibrium state of the considered spins.

$$\hat{H} = \hat{H}_{external} + \hat{H}_{internal} \quad (2.3)$$

$$= \hat{H}_Z + \hat{H}_{rf} + \hat{H}_Q + \hat{H}_{DD} + \hat{H}_{Cs} + \hat{H}_J \quad (2.4)$$

For nuclei such as ^1H , ^2H , ^{13}C , ^{15}N and ^{31}P the ZEEMAN interaction is commonly the strongest. The energy splitting between the two levels of a proton representing a $I = \frac{1}{2}$

nucleus is given by $\Delta E = \gamma \hbar B_0 = \hbar \omega_L$. Here ω_L is the LARMOR frequency and shows a wide range for protons e.g. in a 7 T magnetic field it is 300 MHz, whereas in a 19.9 T environment it reaches 850 MHz.

2.1.2 Chemical shielding (CS)

When applying a magnetic field to a sample, each nucleus experiences a different effective magnetic field due to its individual diamagnetic shielding. This leads to a variation of the ZEEMAN energy and enables an analysis of the chemical structure hence it is referred to as the chemical shielding. The external magnetic field B_0 induces an electric flux in the electron cloud surrounding the nucleus, which in turn generates an induced field $\vec{B}_{ind.}$. Thereby, the nuclear spin is exposed to an effective magnetic field B_{eff} :

$$\vec{B}_{eff} = \vec{B}_0 - \vec{B}_{ind.} = \vec{B}_0 - \bar{\sigma} \vec{B}_0 = \vec{B}_0(1 - \bar{\sigma}) \quad (2.5)$$

Quantitatively this can be measured by the LARMOR frequency for each nucleus in a molecule which is independent of motion or orientation. By definition a scale, independent of the strength of the external magnetic field B_0 is shown in equation 2.6 [HARRIS 01]. The obtained value is called the **Chemical Shift (CS)** (δ) and referenced on an internal or external standard (e.g. for ^1H tetrakis(trimethylsilyl)silane (TTSS) [MUNTEAN 88]). Therefore, the ppm-scale simplifies the comparison of spectra measured at different fields.

$$\delta[ppm] = \frac{\nu - \nu_{ref}}{\nu_{ref}} * 10^6 \quad (2.6)$$

2.1.3 Dipole-Dipole interaction

The **dipole-dipole (DD)** coupling may be either intramolecular or intermolecular. Each nuclear spin generates a magnetic field which is present between all types of spins with $I > 0$. The dipolar coupling is an anisotropic direct spin-spin interaction through space without involving the electron clouds. Each other spin in the range of the magnetic fields interacts with the perturbing spin. As this interaction is mutual, the interaction of a *homonuclear* coupling can be described as follows.

$$\hat{H}_{D,homo}^{IJ} = -\frac{\mu_0 \hbar \gamma^2}{4\pi r^3} (3\cos^2\Theta - 1)(3\hat{I}_{1Z}\hat{I}_{2Z} - \hat{I}\hat{I}) \quad (2.7)$$

The dipole-dipole interaction can be influenced by two geometrical parameters, the distance (r) between the two spins, the angle θ between the internuclear vector and the B_0 field. The *heteronuclear* spin-spin pair frequencies differ significantly, as the dipolar Hamiltonian is reduced to

$$\hat{H}_{D,hetero}^{IJ} = -\frac{\mu_0 \hbar \gamma_i \gamma_j}{4\pi r^3} (3\cos^2\Theta - 1) (\hat{I}_Z \hat{J}_Z) \quad (2.8)$$

$$\omega_D(\Theta) = \omega_0 \pm \frac{1}{2} (3\cos^2\Theta - 1) \quad (2.9)$$

In general, each isotope has a characteristic gyromagnetic ratio γ and affects the dipolar coupling as seen in equation 2.8. Investigation of the dipolar interaction is mostly used in anisotropic solids as dipolar couplings in liquids are commonly averaged due to an isotropic random motion of the molecules. These interactions, however, depend strongly on the distance thus yielding valuable information on proximities between nuclei.

2.1.4 Quadrupole interaction

When a spin is $I > \frac{1}{2}$ it additionally interacts with the local electrical field gradient present at the nucleus. Like the ZEEMAN interaction, the quadrupole coupling affects the energy levels of the nucleus. The interaction depends on the electric field gradient V at the nucleus, the nuclear spin vector \hat{I} and Q which is the nuclear quadrupole moment. With a quadrupolar frequency defined in equation 2.10 the interaction between the electric quadrupole moment of the nucleus and an electric field gradient can be described by the following Hamiltonian [MUNOWITZ 88].

$$\omega_Q = \frac{3e^2qQ}{6I(2I-1)\hbar} \quad (2.10)$$

$$\hat{H}_Q = \omega_Q \hat{I} V \hat{I} \quad (2.11)$$

In the case of deuteron ($^2\text{H}, I = 1$) the quadrupolar frequency is in the range of 2π 125 kHz and the spectra are dominated by two transitions. This remains valid for nuclei where the splitting is much lower than the LARMOR frequency, where first-order perturbation theory can be applied. In the **principal axes system** (PAS), of the quadrupole coupling tensor, the orientation of the external magnetic field B_0 is then defined by the polar angles Θ and

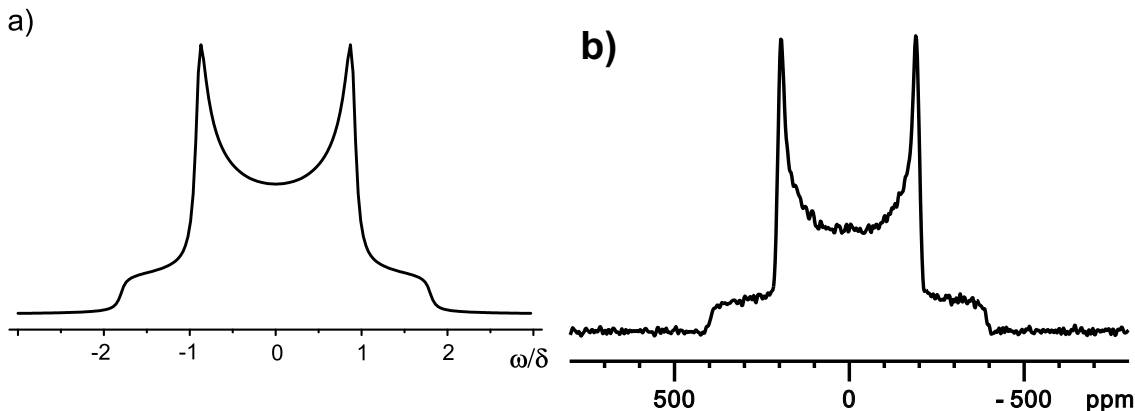


Figure 2.2: a) Theoretical ^2H NMR line shape PAKE-pattern for rigid solid with $\eta = 0$. b) PAKE-pattern of DMS. Due to the methyl rotation the spectrum shows a averaged coupling of $\omega_Q \approx 2\pi \cdot 48$ kHz.

Φ angles. The quadrupolar frequency thereby changes to expression 2.12, with $\delta = \frac{3e^2qQ}{4\hbar}$ consisting of the quadrupolar coupling constant $\frac{e^2qQ}{\hbar}$ and the ZEEMAN frequency ω_0 .

$$\omega_Q = \omega_0 \pm \delta(3\cos^2\Theta - 1 - \eta_Q \sin^2\Theta \cos 2\Phi) \quad (2.12)$$

The asymmetry parameter η is often zero for C-D bonds, meaning that the electric field gradient tensor is axially symmetric. Then the NMR frequency of the two transitions simplifies to equation 2.13.

$$\omega_Q = \omega_0 \pm \delta(3\cos^2\Theta - 1) \quad (2.13)$$

In the solid state in the absence of fast motions the orientation dependence of the quadrupolar coupling leads to the well known PAKE-pattern [PAKE 48]. Nevertheless, fast motions of small parts in the molecule such as methyl rotation can average the quadrupolar coupling, e.g. as observed for dimethylsulfoxide (DMS) shown in Figure 2.2. Notably, for the averaged quadrupolar coupling tensor $\bar{\eta} \neq 0$ may be found even though the initial tensor was axially symmetric [SPIESS 81].

2.1.5 Magic Angle Spinning (MAS)

The NMR spectra of solids typically suffer from broad signals, where line broadening effects can be divided into homogeneous and inhomogeneous, respectively [MARICQ

79]. A countless number of possible molecular orientations cause different resonance frequencies, thus leading to a signal broadening. As the line width increases that much, the possibility to resolve chemical shifts e.g. in protons is lost.

Consequently, a technique called **magic angle spinning** (MAS) was developed in 1958 independently by Andrew and Lowe [ANDREW 58, LOWE 59]. Hereby, the sample is rapidly spun around an axis tilted with respect to the static magnetic field \vec{B}_0 by an angle $\theta_M = 54.7^\circ$. The angular dependence is described by the second LEGENDRE polynomial (i.e. $\nu_r \gg \|H\|$):

$$P(\theta_M) = \frac{1}{2}(3\cos^2(\theta_M) - 1) \quad (2.14)$$

In principle, the interaction tensor can be averaged to zero, in case that the sample spinning frequency is larger than the magnitude of the underlying interaction. Notably, the second Legendre polynomial vanishes for $\theta_M = 54.7^\circ$, which is the so-called *magic angle*. Measuring the sample at the *magic angle* often does not average the interaction completely, since the interactions of interest can be in the range of a 100 kHz. In this research work, a maximum spinning frequency of ≈ 30 kHz was reached using a 2.5 mm rotor.

Other inhomogeneous effects are the **Chemical Shift Anisotropy** (CSA), first order quadrupolar couplings and dipole-dipole couplings of isolated spin pairs. As they are refocused after one rotor period one may obtain sidebands, if the signal is not recorded in a rotor synchronized fashion. This is due to the fact that the Hamiltonian only contains rotor modulated parts. If it is of interest to obtain information of anisotropic interactions, a sideband pattern can be analyzed provided that the spinning frequency is slow enough to let the interaction take effect before being refocussed. Fast MAS concentrates the signal intensity in the center band. Additionally, dipole-dipole couplings between multiple spins cause homogeneous line broadening. The magnitude depends on the natural abundance and gyromagnetic ratio, following the principle the higher the worse. Therefore, especially protons are affected. Sharp lines can be obtained by spinning faster than the interaction parameter ($\omega_R \gg \omega_D$) 2.1.3 which can be up to 30 kHz for protons in solids. Therefore, resolution in proton spectra is usually influenced by homogeneous line broadening even under fast MAS.

2.2 Basic NMR experiments

2.2.1 The single-pulse experiment (SPE)

The first and simplest experiment which was performed in NMR was the single-pulse experiment (SPE). It consisted of a single 90° pulse followed by signal acquisition [BLOCH 46].

In thermal equilibrium the ground state is higher populated obeying the BOLZMANN statistics. By applying a 90° pulse (e.g., parallel to the x -axis) the net magnetization is rotated to the y -axis. While precessing around the B_0 the magnetization induces an oscillating voltage in the detection coil. In modern NMR spectrometers the sign of the rotation phase modulation is detected by mixing of the signal with two reference signals of the same frequency but with shifted phases of 90° . This technique is typically referred to as quadrature detection. The acquired signal decaying with T_2 is called *free induction decay* (FID). Two relaxation processes should be distinguished: the longitudinal magnetization with the relaxation time constant T_1 and the transverse magnetization relaxation time constant T_2 . T_1 can be up to several seconds and even hours in solids, while the transverse relaxation is generally faster.

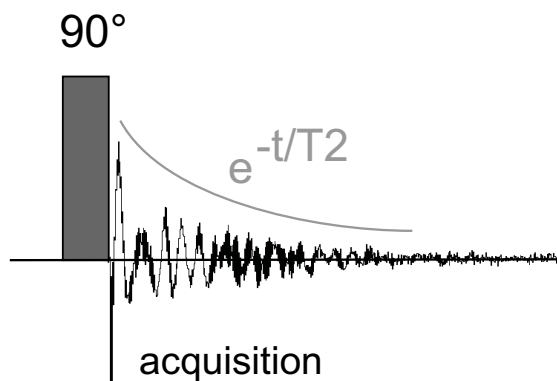


Figure 2.3: The single-pulse experiment

2.2.2 Echo experiments

As a result of the spectrometer hardware, each NMR measurement has a **dead time** (DE). This is due to the high power r.f. pulses which cause ringing of the coil and prevents acquisition during this time. However, this limitation produces severe artifacts if the FID is rather short, as often can be observed in case of strong quadrupolar or dipole-dipole couplings and chemical shift anisotropy. This problem can be overcome by the HAHN

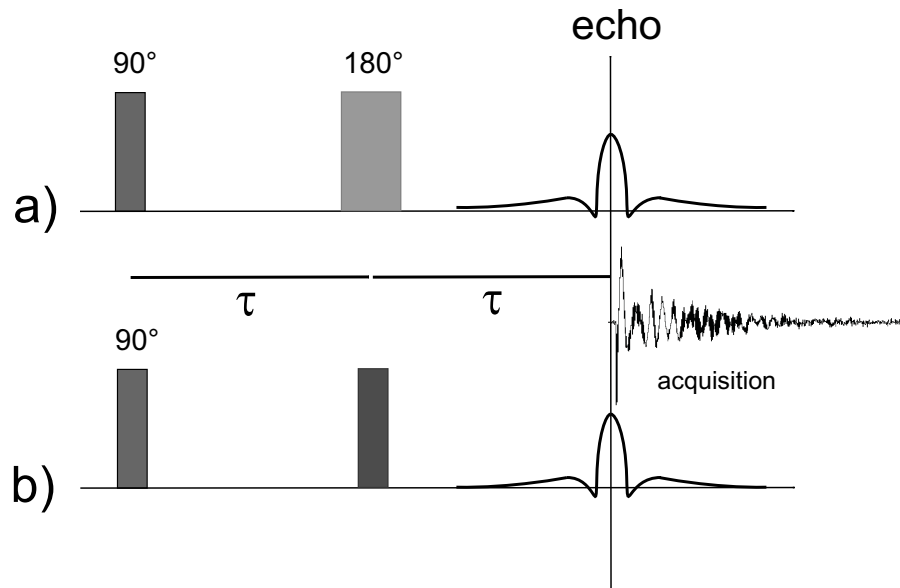


Figure 2.4: a) Hahn spin echo and the b) solid echo sequence. Acquisition starting at the signal intensity maximum.

spin echo [HAHN 50]. Here, an initial 90° pulse rotates the net spin magnetization in the $x - y$ plane where the spins evolve for a time τ . Then a 180° echo pulse is applied that refocuses the FID after time 2τ . The initial state is recovered after a time 2τ and can be measured.

Notably, the Hahn-Echo may only refocus the effects of spin interaction whose Hamiltonian is linearly dependent of the I_z operator. In other cases, the solid-echo has to be applied [SCHMIDT-ROHR 94]. It can refocus e.g. quadrupole interaction or homonuclear dipole-dipole interaction, both $\propto I_z * I_z$, by a 90° echo pulse, phase shifted by 90° from the initial pulse. In particular, in deuterium NMR, molecular reorientations during the solid echo sequence cause frequency changes and lead to characteristic line shapes. Analysis

of the geometry as well as the correlation time of the motion is supported by software like the NMR weblab [MACHO 01].

2.2.3 Cross-polarisation (CP)

Due to a low natural abundance and a low gyromagnetic ratio (γ) spectra of interesting nuclei such as ^{13}C and ^{15}N are rather difficult to obtain. In order to overcome these difficulties, the heteronuclear dipole-dipole coupling between the proton and the heteronucleus is used to enhance the signal intensity. Hereby, the spin polarization is transferred from high γ , high natural abundance nuclei protons to the nuclei of interest [PINES 73]. This experiment is also abundantly used in cases where a nucleus has a longer T_1 relax-

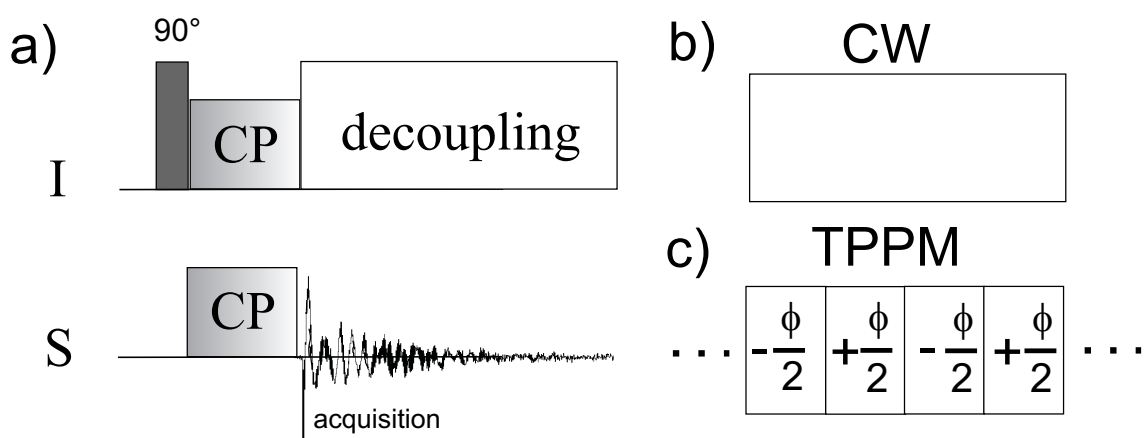


Figure 2.5: a) The cross-polarization experiment. Heteronuclear decoupling sequences.

b) For using continuous wave (CW) decoupling the RF field is switched on for the whole decoupling time.

c) TPPM is a multiple-pulse decoupling scheme.

ation times than protons. In CP experiments heteronuclear dipole-dipole couplings are reintroduced during a given contact time. This is done by irradiating r.f. pulses on both the I and S spins simultaneously. The maximum signal gain is given by the ratio between the two γ . By doing so, the intensity of a carbon signal can be theoretically enhanced by the factor of four. Experimentally, this always depends on the local environment of the S

nuclei such as a different number of coupled I . Consequently, one has to consider that a fully quantitative analysis of such CP-spectra is not always feasible.

$$\gamma_S B_{1,S} = \gamma_I B_{1,I} \quad (2.15)$$

The crucial point of the CP is to match the right r.f. values under MAS conditions on the $B_{1,S}/B_{1,I}$ -ratio. Consequently, one choose a ramp rendering it easier to fit the match [METZ 94]. Often, at $n = \pm 1$, maximum signal is observed.

$$\gamma_S B_{1,S} = \gamma_I B_{1,I} \pm n\omega_R \quad (2.16)$$

2.2.4 Heteronuclear dipole-dipole decoupling

For dilute nuclear spins S (e.g. ^{13}C with $\approx 1\%$ natural abundance) homonuclear dipole-dipole couplings do not have to be taken into account, since the probability of finding two neighbouring spins is fairly low. However, the heteronuclear dipole-dipole coupling of the S spins and high abundance nuclear spins I (usually ^1H) is of the order of tens of kHz and thus can lead to significant line broadening even under fast MAS.

Spins of different nuclear isotopes usually possess gyromagnetic ratios that are sufficiently different to separately manipulate them by r.f. pulses, based on the finite excitation bandwidth of the pulse. For this purpose, a double-resonance probehead is required, where one coil is addressed via two resonance circuits operating at the respective resonance frequencies. A continuous r.f. irradiation of field strength B_1 on the I spins leads to repeated transitions ($\uparrow \leftarrow \rightarrow \downarrow$). The flipping rate is determined by the amplitude of the r.f. irradiation and hence by the oscillation of the heteronuclear dipole-dipole interaction with period $T = 2\pi/\gamma_I B_1$. Thus, the Hamiltonian vanishes when averaged over a period T .

In doing so, the line broadening can be suppressed by a continuous high power irradiation on the I spins during acquisition of the S spin by the continuous wave (CW) decoupling. In order to achieve sufficient decoupling efficiencies rather strong r.f. fields of 50-150 kHz need to be applied. An intuitive way to understand the decoupling effect is that irradiation leads to a precession of the I spins around \vec{B}_1 and therefore, spin S cannot "see" its orientation and is not influenced, hence, the I - S coupling is averaged to zero.

By CW decoupling the dipole-dipole coupling is only removed to first order. In the last years multi-pulse decoupling schemes have been developed to achieve more efficient decoupling, especially for solids under fast MAS. In this thesis **two-pulse phase-modulated (TPPM)** decoupling was used [BENNETT 95]. It consists of a repeated sequence of two pulses with flip angles of approximately 170° and a phase difference in the order of 10° – 50° . This sequence has proven to be robust and more efficient than CW decoupling, since it also suppresses higher-order effects of couplings.

2.2.5 Variable-temperature experiments: mobility of protons

Solid state NMR is also capable to investigate motions in samples. Variable-temperature studies have been performed in the temperature range of -23 to 110°C to study the temperature dependent proton motions. If there is a mobile proton, in the *fast limit*, a change in temperature results in a continuous and significant narrowing of the line width [LEE 07]. In the same temperature range polymers typically show only a slight variation of the backbone or CH proton signal, c.f. Figure 2.6. Furthermore, a tempera-

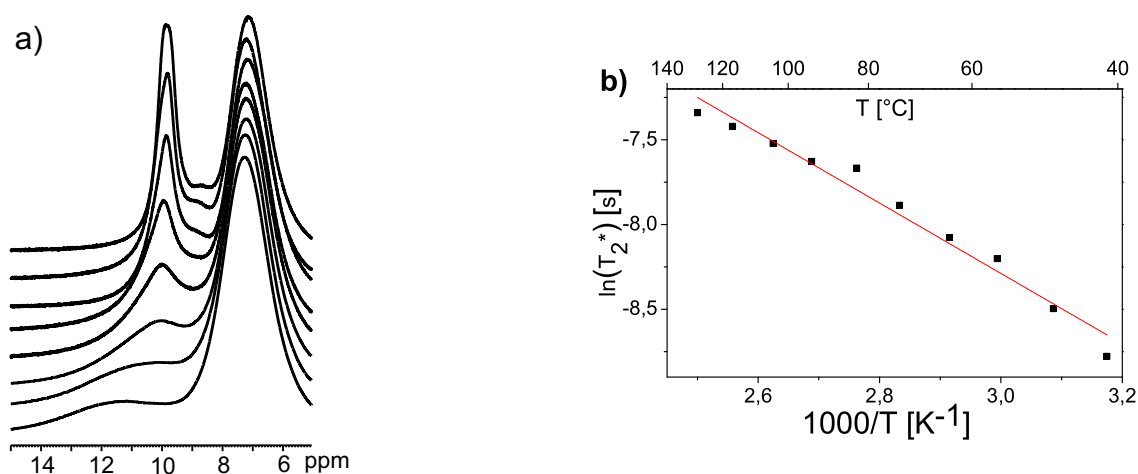


Figure 2.6: a) VT ^1H MAS NMR spectrum at 30 kHz spinning (700.1 MHz, 16.4 T) in a temperature range from the bottom starting with -30 to $+120^\circ\text{C}$ in steps of 10°C .

b) Plotting the logarithmic line width against inverse temperature to obtain the activation energy by the slope.

ture shift of the peak indicates that the motion may involve different sites. The chemical exchange process can be described with regard to the NMR time scale [SPIESS 85], where

the different ranges are characterized by the correlation time, τ_c . Slow and fast exchange limits are defined by $\tau_c > 10^{-5}$ s and $\tau_c < 10^{-7}$ s, respectively.

In the fast exchange limit a single line, at an averaged chemical shift appears. The line shape can be described by a LORENTZIAN curve with a center frequency of ω and a line width of

$$\Delta\nu = \frac{1}{T_2^*} \quad (2.17)$$

where T_2^* is the transverse relaxation time. The change in transverse relaxation time which is a synonym for the change in the line width as a function of temperature can be correlated with the exchange rate, $\Omega = \frac{1}{2\tau_c}$.

If the line width shows a linear dependence on the inverse temperature scale than the apparent activation energy (E_A) can be calculated according to the ARRHENIUS equation, c.f.2.18 & 2.19.

$$\frac{1}{\Omega} = \frac{1}{\pi T_2^*} = \frac{1}{\pi * \Delta\nu} \quad (2.18)$$

$$\Omega = \Omega_0 \exp\left(-\frac{E_A}{RT}\right) \quad (2.19)$$

2.3 Advanced experiments

2.3.1 Two dimensional spectra

Two dimensional NMR established the possibility to investigate coherences which cannot be detected directly. The general principle of a two-dimensional experiment is to introduce a second time domain t_1 prior to acquisition. A defined number of FIDs is recorded incremented by t_1 . After Fourier transformation in both dimensions, a two-dimensional NMR spectrum is obtained [ERNST 87].

Some experiments require a phase sensitive detection in the indirect (t_1) dimension. Therefore, a phase cycling scheme, incrementing the phase of all excitation pulses, has to be applied. Well-established methods are **t**ime **p**roportional **p**hase **i**ncrementation (TPPI) [MARION 83] and the States-TPPI [MARION 89]. The basic idea is to increment the phase in steps of 90° where every increment is Δt_1 or $2\Delta t_1$ respectively. In States-TPPI real and imaginary parts are recorded sequentially and the phase is only incremented every second t_1 increment.

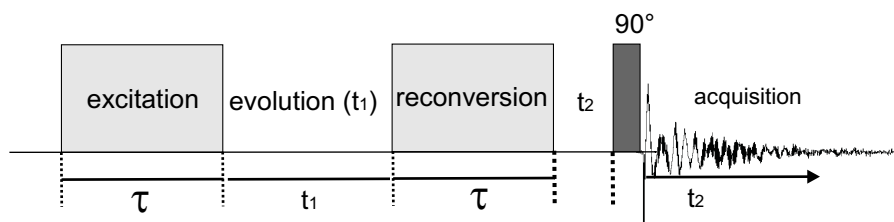


Figure 2.7: Basic structure of a multiple-quantum experiment.

2.3.2 Back-to-Back (BaBa)

In this experiment **d**ouble **q**uantum **c**oherences (DQC) are utilized to obtain valuable information. The term *coherence* describes the extent to which isolated subsystems interfere with the ensemble [MUNOWITZ 88]. In this context single and double quantum coherence will be explained. In a magnetic field \vec{B}_0 the net magnetization is aligned

along the z axis. Consequently, in the x and y plane, there is a randomly distributed magnetization which averaged to zero. Applying a RF pulse orthogonal to the z axis flips the net magnetization from the z axis to the $x - y$ plane. This transverse magnetization represents a transfer between two energy levels with a difference in quantum number of $\Delta m = \pm 1$. Therefore, this transfer is called a single quantum coherence and can be described with product operator formalism in equation 2.20. More information about the product operator formalism can be found elsewhere [KEELER 06]. The double quantum coherence cannot be explained within the classical vector model. Such a coherence couples two spins during a evolution time and forms an anti phase state. This can be further influenced by additional RF pulses e.g. to form a double quantum coherence 2.21.

$$\hat{I}_z \rightarrow \left(\frac{\pi}{2}\hat{I}_y\right) \rightarrow \hat{I}_x \quad (2.20)$$

$$2\hat{I}_{1x}\hat{I}_{2z} \rightarrow \left(\frac{\pi}{2}\hat{I}_{1x}\right)\left(\frac{\pi}{2}\hat{I}_{2x}\right) \rightarrow -2\hat{I}_{1x}\hat{I}_{2y} \quad (2.21)$$

DQC can be generated via the dipole-dipole interaction between two spins. In presence of MAS, which averages the DDC, DQC can only be generated, if the former is recoupled by appropriated pulse sequences. One of such sequences is the Back-to-Back sequence (BaBa) as illustrated in Figure 2.8 [FEIKE 96]. Excitation of DQC can be performed by applying two 90° pulses spaced by half a rotor period ($x - \frac{\tau_R}{2} - \bar{x}$). Due to the sign change of the Hamiltonian the recorded signal is shifted in the phase about 90° which modifies the sequence to $(x - \frac{\tau_R}{2} - \bar{x}y - \frac{\tau_R}{2} - \bar{y})$ when $\tau_{exc.} = 1 \tau_R$. The rotor synchronized version of the BABA experiment is frequently used for spin- $\frac{1}{2}$ nuclei. This sequence is based on homonuclear dipolar coupling and conveniently used as it is rather robust under various MAS conditions.

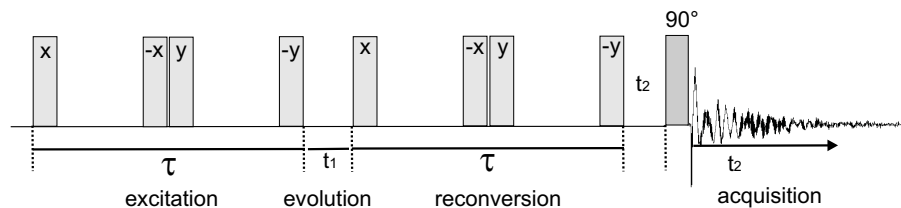


Figure 2.8: Pulse sequence of a BaBa experiment.

BaBa comprises an useful approach to distinguish mobile and immobile protons. Notably,

local mobility may reduce the effective dipolar couplings between two nuclei. Moreover, it is used for determination of ^1H - ^1H proximities and ^1H - ^1H internuclear distances [SCHNELL 01a]. Spin-spin distances in the range of several Å can be investigated depending on the excitation/reconversion times and the strength of the dipole-dipole interaction 2.22.

$$D^{(ii)} = \frac{-\mu_0 \hbar \gamma_i^2}{4\pi r_{ii}^3} \quad (2.22)$$

A schematic 2D spectrum that may be obtained with the BaBa sequence is shown in Figure 2.7. The double quantum coherence between spins of different chemical shifts are represented by the sum of the frequencies ω_A and ω_B , the "cross peaks" and can be detected at both frequencies ω_A and ω_B . The single quantum dimension reveals information if two nuclei of the same chemical shift can form a double quantum coherence. This are the "auto peaks" which are located at the diagonal of the spectrum.

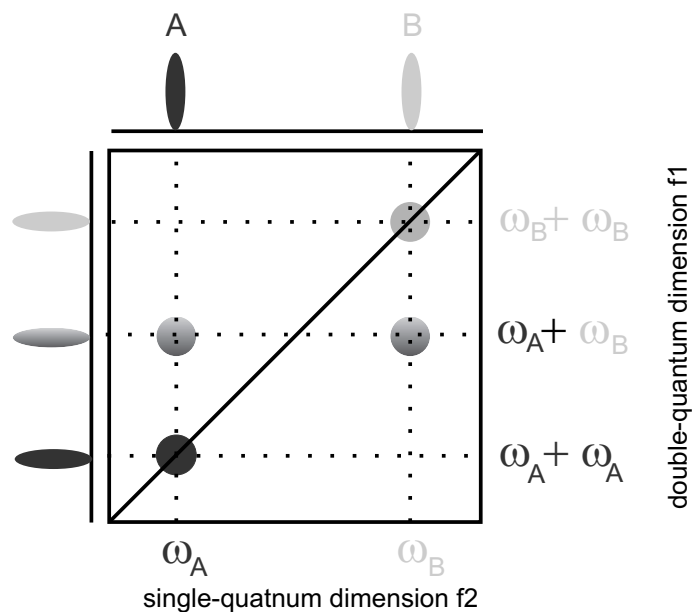


Figure 2.9: Schematic representation of a two-dimensional rotor-synchronised BABA spectrum.

2.3.3 Heteronuclear dipole-dipole recoupling

Heteronuclear dipole-dipole interactions are usually averaged by MAS to obtain a high resolution spectrum. A number of experiments which reintroduce these interactions use a building block of the **rotational- echo double- resonance** (REDOR) experiment developed by Guillion et al. [GUILLION 89]. This block is based on π pulses spaced by half a rotor period, which invert the sign of the Hamiltonian and thus recouple the heteronuclear dipole-dipole interaction. Useful sample information about both, proximities can be obtained by **recoupled polarization transfer- heteronuclear single-quantum correlation** (REPT-HSQC) and dynamics by **rotor encoded - REDOR** (REREDOR) and **recoupled polarization transfer - heteronuclear dipolar order** (REPT-HDOR). Since in this work dipolar constants were obtained using REPT-HDOR the others will not be discussed in detail [RAPP 03]. Since the 180° pulses only lead to an inversion of the sign, they can

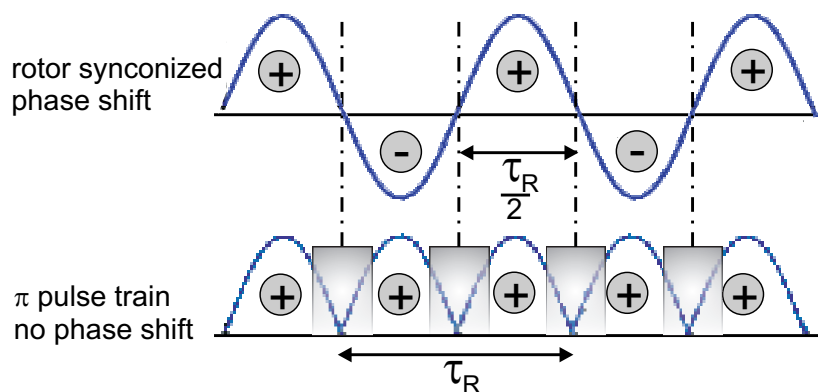


Figure 2.10: Principles of recoupling using a pulse train.

be applied on the I and S channel without changing the average Hamiltonian which also can describe the evolution over one rotor period of the recoupling π pulse train. This, however, is only the case in the absence of quadrupolar coupling. All experiments which are referred to in this work use the same REDOR scheme but differ by the nucleus from which the recoupling process is started and the detected nucleus, either conventional X or inverse ^1H -detection [SAALWÄCHTER 02].

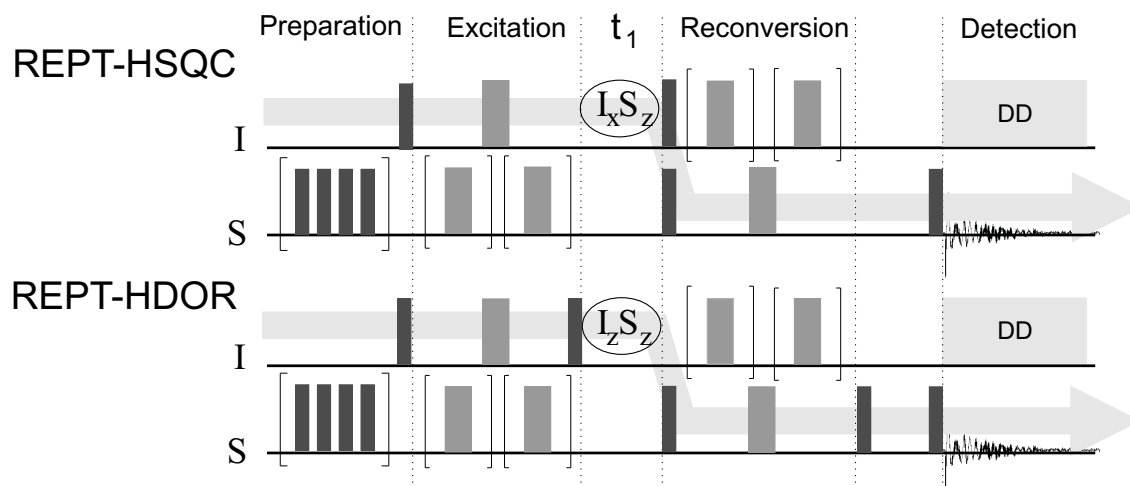


Figure 2.11: Pulse sequences for heteronuclear correlation spectra based on REDOR. The arrows indicate the possible pathways for the transverse components of the coherence states present in the indirect dimension t_1 .

REPT-HDOR

The REPT-HDOR experiment facilitates the determination of heteronuclear dipole-dipole coupling constants within reasonable measuring times in samples with ^{13}C in natural abundance. The characteristic feature of REPT-HDOR is to create a state of heteronuclear dipolar order which does not evolve during t_1 [SAALWAECHTER 01b].

This $\hat{I}_z\hat{S}_z$ state is obtained prior to t_1 by a 90° pulse on the I channel. Another 90° pulse on the S spin converts back into antiphase coherence $\hat{I}_z\hat{S}_y$ after t_1 . During reconversion this antiphase coherence evolves back into observable SQ coherence. The signal is periodic with respect to the rotor period. Since T_1 relaxation times are usually much longer than the timescale of MAS, a decay is most likely not observed.

The data processing was done as follows. After Fourier transformation (FT) along the direct (F_2) dimension, slices corresponding to the signal of interest have been extracted. The obtained sideband patterns have been evaluated with MATLAB to obtain the dipole-dipole coupling constants. A coupling of $\frac{D_{is}}{2\pi} = 22.2 \text{ kHz} \Rightarrow r \simeq 1.1 \text{ \AA}$ is characteristic for rigid aromatic CH pairs. However, REPT-HDOR is not suitable to generate spinning sideband patterns for multispin systems (e.g. CH_2 and CH_3 groups). An alternative

approach is the REREDOR experiment, which generates spinning sidebands by reversion rotor encoding. In both cases, the number and intensities of spinning sidebands can selectively be pumped by the length of the recoupling time. This depends on the product of the coupling constant multiplied with the recoupling times $D_{is} * \tau_{rcpl}$. In REREDOR the mechanism provides only odd sidebands and no center line.

REPT-HSQC

The REPT-HSQC experiment is a 2D experiment that correlates chemical shifts of two different nuclei I and S via the heteronuclear dipole-dipole couplings [SAALWAECHTER 01b]. Such spectra are especially useful to assist proton assignments in samples with poor ^1H resolution. The intensities of the peaks are determined by the number of recoupling cycles and the strength of the ^1H - ^{13}C dipole-dipole coupling.

When both dimensions are rotor synchronized, the t_1 evolution is only caused by the isotropic chemical shift of the I spins. After Fourier transformation in both dimensions a heteronuclear correlation spectrum is obtained.

Chapter 3

Fuel cells

Fuel cells are considered as environmentally-friendly alternatives to combustion engines using fossil fuels [CARETTE 01]. An electrochemical conversion has the advantage of minimized emission of green house gas CO_2 . Therefore, in our days a wide variety of principal fuel cell designs such as the polymer electrolyte membrane fuel cell (PEM), direct methanol fuel cell (DMFC), alkaline fuel cell (AFC), phosphoric acid fuel cells (PAFC) as well as the molten carbonate fuel cells (MCFC) are used. Due to their different capacities many applications, such as stationary fuel cell in power plants or portable cells integrated in automotives are feasible.

3.1 Polymer electrolyte membrane fuel cell (PEMFC)

One prominent group of fuel cells comprises **polymer-electrolyte membrane fuel cells** (PEMFC), where the PEM separates the cathode from the anode, thus preventing a short circuit. The first Fuel Cell containing a polyelectrolyte membrane was already designed by General Electric in 1959 [GUARAU 00]. Even though fuel cells containing proton conducting polyelectrolyte membranes are increasingly used in industry, the understanding of the proton transport mechanism particularly at molecular level is still fairly limited. Recently, there are three major aims of scientific research:

- molecular basis of proton transport

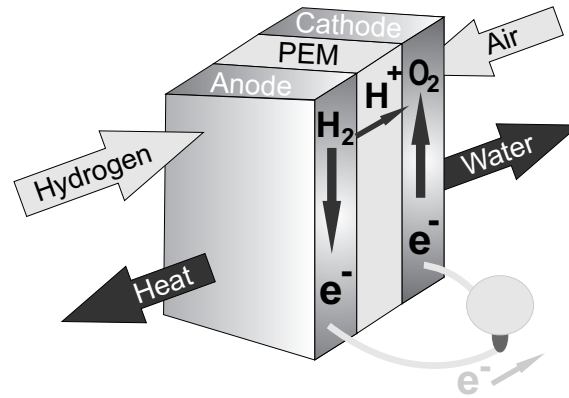
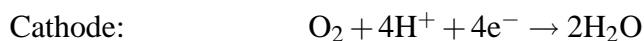
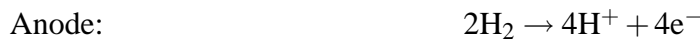


Figure 3.1: Schematic picture of a PEM fuel cell.

- diffusional motion
- reorganization of the hydrogen bond network ¹

The PEM is permeable to protons, but does not conduct electrons, while typical electrodes are based on carbon. Hydrogen enters the fuel cell at the anode and is split into protons and electrons. The H^+ permeate through the electrolyte to the cathode. The power is provided by the electrons which simultaneously to the protons flow along the external circuit. The oxygen can be supplied simply from air. At the cathode oxygen and electrons are combined with the hydrogen ions reacting to water:



PEMs which are typically used within industry scale applications consist of perfluorinated sulfones e.g. Nafion[®] provided by Du Pont since the 1970s. Further commonly used membranes are sulfonated polysulfones distributed by Dow Chemical Company and Polyimidazoles by Celanese. These PEMs are widely used due to their sufficient conductivity as well as long-term stability. However, a drawback of those membrans is

¹[KREUER 96]

	PEMFC	DMFC	AFC	PAFC	MCFC
Proton conduction	H ⁺	CH ₃ OH	OH ⁻	H ⁺ (PO ₄ ⁻³)	CO ₃ ⁻²
Operating temperature [°C]	80	120	80	150 – 200	650
Efficiency [%]	83	40	60	40	80
CO poisoning	+	-	+	-	-
Catalyst	Pt	Pt	Pt	Pt	Ni

Table 3.1: Overview of different fuel cells.

<http://www1.eere.energy.gov/hydrogenandfuelcells/fuelcells>

that they can only be operated below 80°C. This is due to catalyst poisoning with carbon monoxide and methanol crossover [KREUER 07]. Another economic limitation is that they are based on high cost materials. This major constrain explains the limited use of fuel cells in daily practice, e.g. cell-driven cars and to the large-scale commercialization.

Technical problems such as CO poisoning and methanol cross over may be prevented by operating at elevated temperature in the range of 100°C-200°C [WINTER 04]. However, this is not practicable with the currently used systems as they are based on incorporated water which transports the protons as vehicle and limits the operating temperature to 80°C [HEITNER 96].

Therefore, PEMs may work on alternative protonic solvents such as phosphoric acid (H₃PO₄) which is most commonly combined with **poly-benzimidazole (PBI)** and provides a good alternative to Nafion[®]. It shows sufficiently high conductivity as well as good thermal stability in the required temperature range of 100°C-200°C [KERRES 99]. Even though, these materials are produced on an industrial scale, leaching of phosphoric acid from H₃PO₄ swollen PBI membranes by reaction water is another troubling issue which has to be controlled [ASENSIO 05, XIAO 05].

This, however, is the motivation for scientist all over the world to work to find a suitable alternative to current design of new PEMs. Consequently, it is essential to understand the parameters which effect the proton conductivity. This is an important milestone that paves the way towards a commercial use of fuel cells.

3.1.1 Direct methanol fuel cells (DMFC)

This fuel cell is a variation of the PEM fuel cell [BOLUFER 08]. It uses methanol directly instead of producing hydrogen of it. Therefore, the reaction at the anode comprises splitting of methanol into CO₂ and hydrogen. They operate at around 120°C with efficiencies² of around 40%. The major drawbacks are the larger quantity of platinum catalyst needed leading to significantly higher costs, the reaction of methanol and the release of CO₂ which is considered as a greenhouse gas. In contrast, this argument contradicts the claim of an environmentally-friendly alternative.

3.1.2 Alkaline fuel cells (AFC)

Another modification of the PEM cell is the AFC [BROECK 93]. The design is similar to that of a PEM cell. Instead of a membrane it uses an aqueous solution or potassium hydroxide as electrolyte. Rather than H⁺, hydroxyl ions (OH⁻) are transported from the cathode to the anode. There the reaction to water and electrons occurs. Their working temperature is around 80°C which is the same range as PEMFC and therefore exhibits similar drawbacks e.g. due to CO poisoning. They are the cheapest but also biggest (size-efficiency) fuel cells limiting widespread application.

3.1.3 Phosphoric acid fuel cells (PAFC)

As the name implies PA fuel cells are working on phosphoric acid electrolytes incorporated in a silicone carbide matrix [KUMURA 04]. The working temperatures are around 150 to 200°C providing a faster reaction rate. This temperature range also increases the impurity tolerance for a longer life time. Further advantages are the simple matrix-solvent construction, stability and low electrolyte volatility. Drawbacks are requirement of a platinum catalysts on the electrodes to assure reactivity and a relatively low efficiency of only

²Efficiency is typically defined as the electrical energy, divided by the calorific value of the fuel. The calorific value (CV) is the maximum energy one could obtain from a fuel by burning it. The maximum amount of electricity that can be gained from the cell is represented by the Gibbs energy (G). In a perfect system, the efficiency of a fuel cell would decrease with increasing temperature, as the Gibbs energy decreases with higher temperatures. <http://www.worldenergy.org/>

40%.

3.1.4 Molten carbonate fuel cells (MCFC)

MCFC fuel cells work at high temperature at around 650°C which means that they are able to generate hydrogen within the fuel cell structure [BISCHOFF 06]. Furthermore, no CO poisoning is observed, while cheaper catalysts like nickel can be used. Such temperatures, however, are difficult to control in day-to-day operation which limits the applicability of those cells. Nevertheless, once heated MCFC show a high efficiency of up to 80% making them attractive for large-scale industrial processes, e.g. in combination with electricity generating turbines. High temperatures are needed to melt e.g. lithium potassium carbonates and generate carbonate ions. They are the vehicles from the cathode to the anode where they react with hydrogen to water, CO₂ and electrons.

3.2 Mechanisms of proton transport

In the recent literature, two distinct mechanisms for proton transport are widely discussed. Either structural diffusion via rapid hydrogen-bond breaking and forming or vehicular diffusion of molecules [TUCKERMAN 97, AGMON 95, MUNSON 64, KREUER 00]. Still, there is no clear tendency which mechanism describes the proton transport best. In particular, as it is rather difficult to clearly distinguish possible contributions of both mechanisms to the overall proton transport.

Vehicular and structural diffusion of water

Water is an excellent vehicle for proton transport, given its relatively high self-diffusion coefficient at room temperature of $2.25 \cdot 10^{-5} \text{ cm}^2/\text{s}$. The proton transport does not involve H^+ as such but rather hydronium ions formed due to self-dissociation of water. A comparison of cation sizes of different electrolytes water with measured ion mobility does not show a linear correlation. In addition to the vehicle properties, water shows a

Cation	Mobility [cm^2/Vs]	d[nm]
H^+	$3.62 \cdot 10^{-3}$	0.05
NH_4^+	$0.763 \cdot 10^{-3}$	0.143
K^+	$0.762 \cdot 10^{-3}$	0.138
Na^+	$0.519 \cdot 10^{-3}$	0.102

Table 3.2: Mobility of cations in aqueous solution and ion diameter.

high structural diffusion. Adding an excess proton to water facilitates complexes formed with either two or four water molecules. This are the so called EIGEN ($H_5O_2^+$) [EIGEN 64] or ZUNDEL-IONS ($H_9O_4^+$) [ZUNDEL 86]. Comparing the self-diffusion coefficient of water at room temperature of $2.25 \cdot 10^{-5} \text{ cm}^2/\text{s}$ and the proton diffusion of $9.3 \cdot 10^{-5} \text{ cm}^2/\text{s}$ [AGMON 95] it suggests that the excess proton contributes approximately 22% to the overall conductivity. In literature the movements of 1H through water moiety are described by two different ways:

- A field-induced water rotation along the lone-pair of the hydronium [BERNAL 33].

- Formation of a static cluster building out a water hydrogen network [AGMON 95].

The second model assumes that protons can hop along the moiety. This model is supported by the proton conductivity in ice which is two orders of magnitude higher than in water. Therefore, structural diffusion is claimed to be the rate limiting step in water proton conductivity. Nevertheless, this result is not undisputable as a lot of new results cannot be explained by this model. The first model on the other hand claims that the water molecules rotate either freely or through an angle (H-O-H) of 110°C [CONWAY 64]. Taking into account that each water molecule is *fixed* by four hydrogen bonds in the first hydration shell with a hydrogen bond strength of 10.9 kJ/mol [WALRAFEN 86], it seems quite unlikely, that this represents the rate-limiting step, including cleavage of a hydrogen bond. Therefore, it is considered that the second solvation shell is the place where the reorganization takes place [AGMON 95, SCHMIDT 05].

Part II

RESULTS AND DISCUSSION

Chapter 4

Phosphonic acid containing ionomers

Poly electrolyte membrane based fuel cells (PEMFC), as described in chapter 3, are currently in the focus of many research groups. In fact, hydrogen based fuel cells may one day substitute combustion engines working with fossil fuels. Recently, two major approaches which possibly facilitate high temperature operation of fuel cell membranes have been reported. One attempt is based on the addition of small proton carrier molecules to a non-conducting polymer matrix. The second way mainly uses polymers composed of hydrophobic backbones, containing hydrophilic protogenic side-chains. Hence, such a system would possibly allow higher proton mobility as a result of increasing flexibility of the protogenic groups [PADDISON 06].

This chapter discusses a concept which proposes to increase proton mobility by a self-assembled and preorganized systems suggested by Jiménez et al. [JIMENEZ 09]. Until now, the major ongoing research focuses on the addition of small molecules to a polymer matrix, as mentioned above. Systems using small molecules for proton conduction are so far fullerene and zwitterion based [HINOKUMA 01, YAMADA 05]. Therefore, it is of interest to investigate organic molecules of different geometrical shapes to reveal the effects of different organizations. The focus in this chapter is to compare the microscopic information obtained by NMR about mobility and local order with the macroscopic conductivity obtained by impedance spectroscopy.

The analyzed molecules combine a hydrophobic aromatic moiety and hydrophilic

Figure 4.1	IUPAC	Abbreviation
a	1,4-Bis(<i>p</i> -phosphonatophenyl)benzene	Line
b	1,3,5-Tris(4-phosphonatophenyl)benzene	Triangle
c	1,3,5-Tris[phenyl-2-(<i>o</i> -phosphonatophenyl)]benzene	Screw
d	Tetrakis-1,3,5,7-(4-phosphonatophenyl)adamantane	Tetrahedron
e	1,2,4,5-Tetrakis(<i>p</i> -phosphonatophenyl)benzene	Square
f	Hexakis(4-phosphonatophenyl)benzene	Hexagon

Table 4.1: Abbreviations for the different ionomer geometrical shapes.

phosphonic acid (PA) groups. This particular acidic group has been suggested to be a good protogenic group for intrinsically conducting separator materials, since its amphoteric property is in the adequate regime [SCHUSTER 05]. The different chemical structures are sketched in Figure 4.1. Indeed, the drawn structures do reflect neither the three dimensional structures nor their geometrical shape which might look quite different due to repulsion forces. The compounds were provided by L. Jiménez García [JIMÉNEZ 09] from the group of Prof. K. Müllen at the MPIP. For clarity the nomenclature of the molecules described in this work reflects the intended geometrical shape as described in Table 4.1.

In this work the results are often compared to poly(vinyl phosphonic acid) (PVPA) which is considered as a model system for proton-conducting in a phosphonic-acid-tethered polymer. In particular, the structure contains a high concentration of acid groups and adopts a highly disordered structure. In the case of PVPA, previous studies using solid-state NMR methods like ^1H double-quantum (DQ) and variable-temperature (VT) MAS NMR experiments showed that P-OH protons are rather mobile and contribute to the proton conductivity. In VT ^1H and ^{31}P MAS NMR experiments the resonance corresponding to the PA does not change the chemical shift. An activation energy of 65 kJ/mol can be calculated from impedance spectroscopy. This value by far exceeds the activation energy calculated from ^1H MAS NMR line width studies with 25 kJ/mol, reflecting proton mobility rather than proton conductivity [LEE 07a].

In general, water is incorporated in the PVPA as bulk water, indicated by sharp signals at 5 ppm in the ^1H MAS NMR spectra, which is comparable to Nafion

[SCHAUFF 07]. Clearly, the presence of water has a huge effect on the observed bulk proton conductivity of PVPA which under anhydrous conditions can reach 10^{-3} S/cm at 150°C under 1 bar relative humidity (RH). Apart from a vehicular mechanism, water can also participate in the proton transport by a GROTHUSS-type mechanism, where protons are transferred between neighboring PA sites. Based on the ^1H chemical shift an approximate ratio of water molecules to PA groups in the PVPA of $n(\text{H}_2\text{O})/n(\text{PO}_3\text{H}_2)=1$ is found [KALTBEITZEL 07]. This amount of water is sufficient to increase the bulk proton conductivity by orders of magnitude. This chapter will discuss the bulk proton conductivity of the different geometrical shapes. This implements the influence of incorporated water, crystallinity, and structural features of the samples.

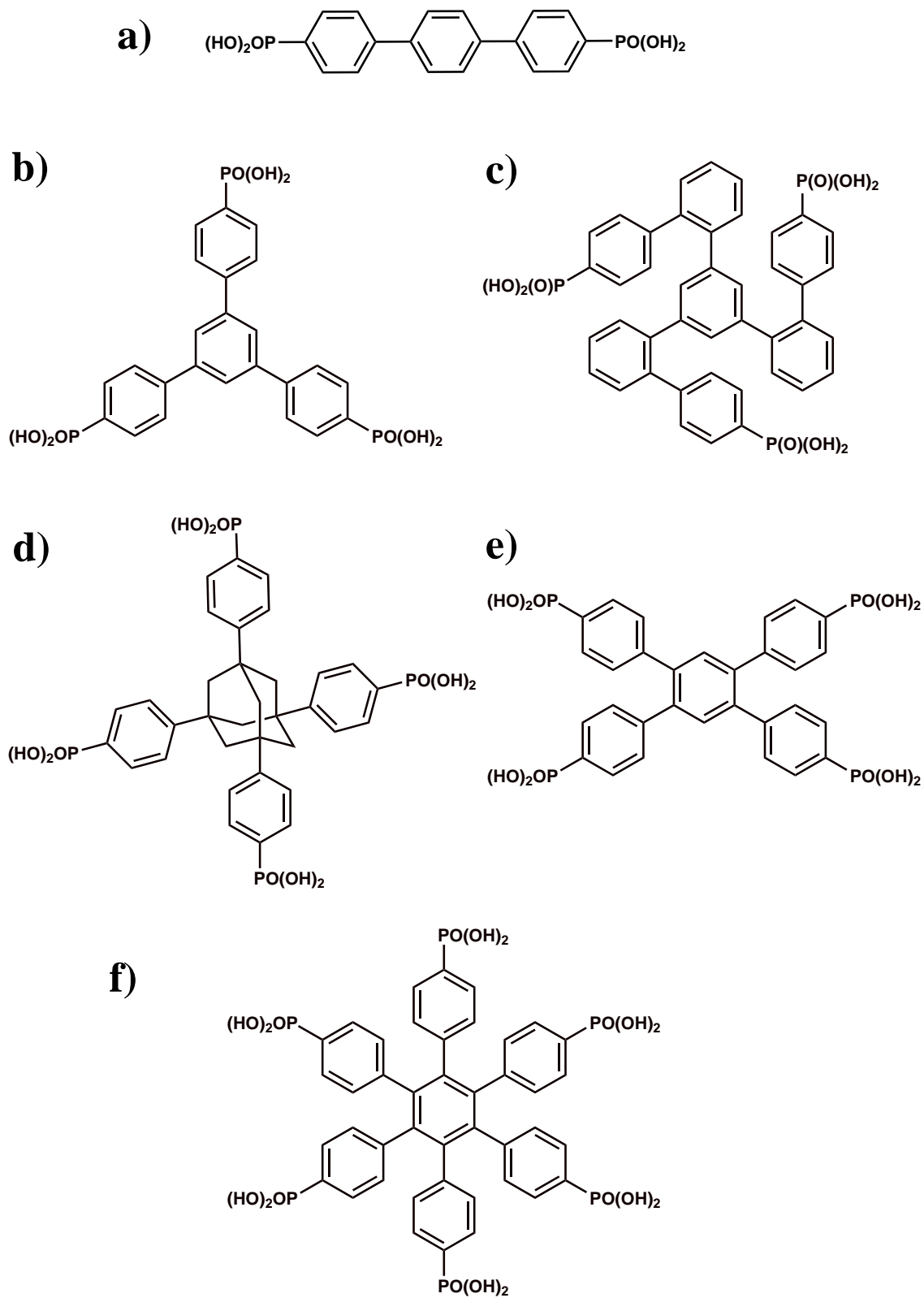


Figure 4.1: Different structures of ionomers with the geometrical shape of
a) LINE b) TRIANGLE c) SCREW d) TETRAHEDRON e) SQUARE f) HEXAGON.

4.1 Bulk proton conductivity

This study was performed to probe similar molecules based on an aromatic benzene moiety with a defined number of PA attached to the moiety. It is known that the proton conductivity to a great extent depends on the relative PA content of the single molecule [STEININGER 07]. Since the PA amount is obtained by varying the number and density of PA groups, different geometric structures were implemented. Consequently, different assemblies of the molecules and local orientation of the PA groups are expected.

Since these samples should work as proton conducting membranes, it is important to measure the bulk proton conductivity. Bulk proton conductivity data of all samples were provided by A. Kaltbeitzel using dielectric spectroscopy covering a frequency range of $10^{-1} - 10^{-6}$ Hz. Evaluation was performed using a BODE plot where proton conductivity [S/cm] is plotted against frequency (ω) [Hz]. Each measurement shows a plateau where the AC conductivity is independent of the frequency. This value is extrapolated against $\omega = 0$ which represents the DC conductivity at the respective temperature. Typically, these plots show either a positive or a negative slope due to a temperature dependent conductivity. For possible application in fuel cell membranes, bulk proton conductivities better or equal than 10^{-3} S/cm were considered reasonable.

The bulk proton conductivities of the different geometrical shapes under dry nitrogen flux are plotted in Figure 4.2. The measured temperatures range either from 20 or 50°C up to 160°C. Notably, within this temperature range all ionomers show a negative slope which indicates a higher conductivity at higher temperatures. Often, a negative dependency is observed for anhydrous proton conductors [NARAYANAN 06]. By comparing these results, the measured values of the ionomers are divided into three groups. All three reveal an insulator-like conductivity below 10^{-3} S/cm. At 160°C LINE and TETRAHEDRON show the lowest conductivity in the range of 10^{-7} S/cm and the SCREW, SQUARE, and TRIANGLE of 10^{-5} S/cm falls in the middle. The most promising sample is the HEXAGON which reaches value of nearly 10^{-4} S/cm at 160°C.

In the dry state both the amount and density of PA in the sample is expected to strongly affect the conductivity. To obtain the PA density, the ratio between the mass of

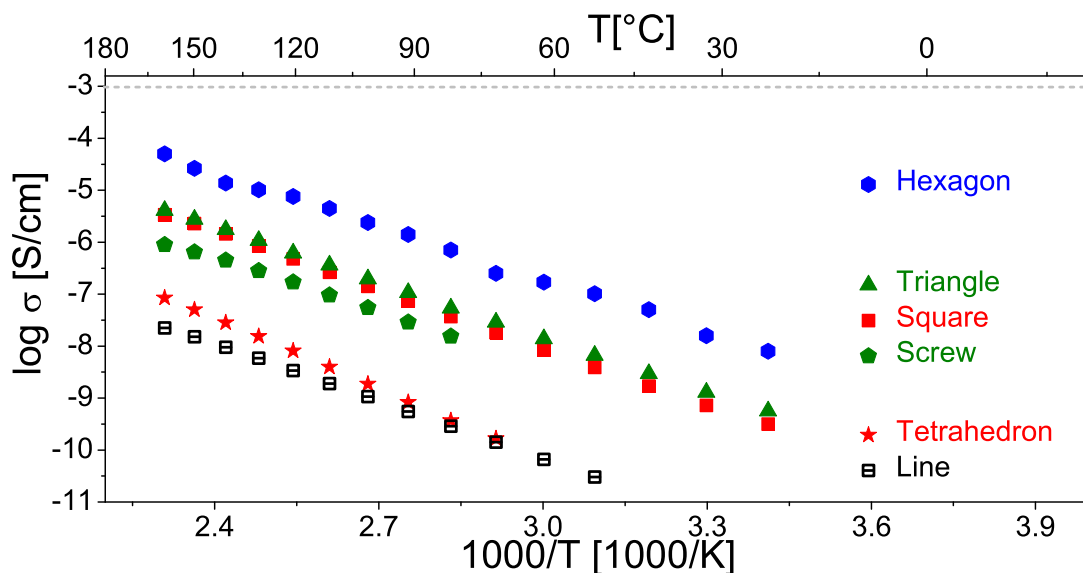


Figure 4.2: Proton conductivity obtained by impedance spectroscopy under dry nitrogen flow (second heating). The activation energies (E_A) of all geometrical shape are listed in Table 4.2.

PA and the aromatic moieties was compared. The calculation is exemplarily shown for the HEXAGON:

$$\frac{M_n(PA)}{M_n(Moiety)} = \frac{6 M_n(PA)}{M_n(6 Ph(4H) + 1 Ph(0H))} = \frac{486 \text{ g/mol}}{528 \text{ g/mol}} = 0.92 \quad (4.1)$$

The highest ratio was found for the HEXAGON. By comparing these values with the conductivity at dry conditions, it has been observed that the absolute value of the bulk conductivity decreases with a decreasing PA to moiety ratio. The only exception is the SCREW with an extremely small mass ratio of 0.46, but showing a higher conductivity than e.g., the LINE with 0.71. In contrast, the SCREW, which contains three PA groups, the same number as the TRIANGLE (mass ratio: 0.80), shows both a lower conductivity and a lower mass ratio. These results strongly suggests a dependency of proton conductivity on the combination of PA number and density in the moiety.

It is known that the proton conductivity not also depends on temperature but also on the relative humidity (RH) [SCHUSTER 05]. Especially, PA containing samples are known to suffer from condensation which can be prevented by conducting the

measurements in humid environment. Therefore, the samples were equilibrated at a defined RH and measured as described in the Appendix chapter B. At the conditions of high RH, bulk proton conductivity below 100°C was not accessible due to technical limitations. Consequently, the obtained data reflect the temperature range from 110 to 180°C.

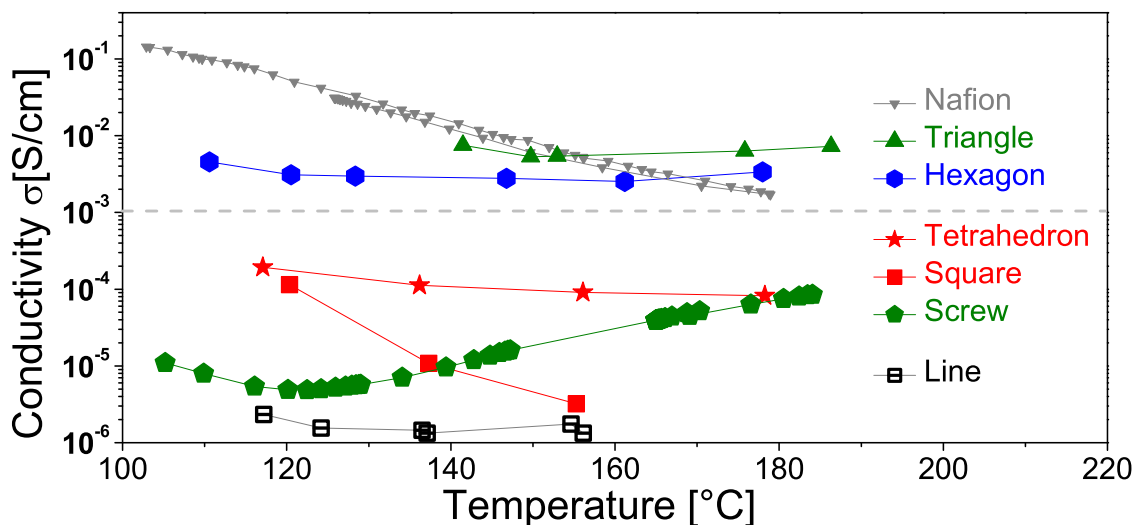


Figure 4.3: Proton conductivity obtained by impedance spectroscopy at 1 bar at different temperatures and their different relative humidities (RH). Effective bulk proton conductivities at 140° are listed in Table 4.2. HEXAGON [JIMENEZ 09]

Notably, within the chosen temperature range, the conductivity increases by one to two orders of magnitude depending on the sample. Again, the samples are divided into different groups: the LINE, TETRAHEDRON, SCREW, and the SQUARE reveal an insulator like conductivity below 10^{-3} S/cm. The second group includes the most promising samples, namely, the TRIANGLE and the HEXAGON. Their conductivity of 5.50 and $2.78 \cdot 10^{-3}$ S/cm respectively, are comparable to Nafion[®]. Thus, it can be expected that the content of water plays an important role in the proton transport mechanism. Nevertheless, all group members contain similar chemical compounds and display different conductivity behavior. The highest jump from dry to humid bulk conductivity is observed for the TRIANGLE. This suggests a high amount of water incorporated into the system and possibly also explain the difficulty to perform the impedance spectroscopy in

humid conditions due to solvating. The water uptake curve shows that, e.g., the LINE does not absorb much water, while the HEXAGON absorbs an equivalent of ≈ 3 H₂O molecules per 6 PO₃H₂ units at 100% RH.

The proton bulk conductivity at humid conditions causes differences in the slope behavior of the different geometrical shapes. The TRIANGLE shows the highest conductivity, which is slightly better than the HEXAGON followed by the TETRAHEDRON. Similarity to the dry measurements is found in the LINE showing the lowest bulk conductivity of all geometrical shapes. The most striking behavior is shown by the SCREW. In the first temperature range up to 120°C with increasing temperature the conductivity drops as commonly observed in vehicle-based proton conductors like Nafion[®] [AFFOUNE 05]. This trend is inverted at 120°C and the slope changes its sign from negative to positive. This behavior suggests a change in the proton transport properties from the vehicle to a GROTHUSS-type mechanism. Since this effect is reversible and reproducible it should be accompanied by a temperature dependent morphological change in the sample. The only sample which behaves as one would expect for a water based system is the SQUARE where the conductivity decreases with increasing temperature similar to Nafion[®]. A closer look on the ionomers proton conductivity reveals that the data for the TRIANGLE, HEXAGON, TETRAHEDRON, and LINE are apparently temperature independent, at least within the observed temperature range. This rather unexpected behavior rises once more the question what might happen on the molecular scale. In general, this behavior is not commonly observed since a thermal activation for proton conduction is expected, e.g., for an ARRHENIUS type of activation this would lead to a positive slope. In contrast, Nafion[®] has a negative temperature dependency, as plotted in Figure 4.3. This can often be observed in systems where the proton transport is based on the vehicle mechanism e.g., by utilizing free water molecules [AFFOUNE 05]. A constant behavior at changing temperature has to be due to the microscopic sample properties. Either the protogenic group has a very low activation energy, or the conductivity is based on the presence of small molecules in the sample. In both cases, a higher temperature would not necessarily lead to a higher conductivity. The protogenic group is the same in all ionomers. Since, the PA is known to show a thermal dependency the argument of the low activation energy of the protogenic group can be ruled out. On the other hand, it is known from the literature that different factors exist which may cause a temperature

independent slope behavior based on the presence of small molecules. The proton conductivity of, e.g., imidazole-based systems have been investigated with increasing immobilization, ranging from the monomer [KREUER 98] via oligomers [PERRSON 03] to fully polymeric systems [HERZ 03, RADEV 08]. All these publications include materials with negative slopes but a flattening with increasing mobility. This might also be the case for the investigated systems here, where the incorporated water molecules increase the proton mobility, e.g., in the HEXAGON. Another investigation shows that in imidazole-based oligomers doped with a high concentration of charge carriers, such as triflic acid, show a tendency to be temperature independent [SCHUSTER 01]. In oligomeric systems like octanephosphonic acid, a flattening of the proton conductivity is found as a result of exposing the sample to a humid atmosphere [SCHUSTER 05]. This tendency can additionally be followed in sulfonated poly(ether ether ketone) (S(PEEK)), which were measured as a function of water content added to the polymer [KREUER 04]. All these results support the idea that the proton transport for the investigated samples, in particular in the HEXAGON most probably depends on the incorporated, highly mobile water molecules which exchange their protons with those of PA, supporting the diffusion mechanism based on the PA. This is studied in the following chapters.

4.2 NMR characterization of the hydrogen bonds in the ionomers

For characterization of chemical compounds typically liquid-state nuclear magnetic resonance (NMR) is used. This has been done for all geometrical shapes and compared with solid-state NMR spectra. Differences between them may reveal information about the solid state arrangement [LAWS 02]. Since the chemical shifts in the solid state are not averaged isotropically they in principle contain information about the sample orientation. Thus, solid-state magic angle spinning (MAS) NMR spectra often show rather broad spectra compared to the liquid case due to the difference of orientations presents in a powder sample. On the other hand, signals which might not be present in the liquid, due to fast exchange, i.e. hydrogen bonds, can be detected and analyzed [BRUNNER 98, DENSMORE 05]. This additional information usually is not detectable in the liquid state due to the high dissolution or concurrent interaction with the solvent. The investigation of hydrogen bonds and their ability to form a network in supporting proton conduction is the aim in this study. All samples have been obtained directly from synthesis, dried under vacuum for at least two days at 50°C, except the SQUARE, which was annealed 1 hour at 110°C. Further experimental details about measurement methods are given in the Appendix chapter B.

From the ^1H MAS NMR spectra information about the hydrogen bond strength are extracted using the chemical shift (δ_{iso}) of the resonance. A correlation between the proton δ_{iso} and the strength of the hydrogen bonding was reported by Harris et al. Since the hydrogen bond strength depends on distances between oxygens participating in hydrogen bonds it will also affect the chemical shift [HARRIS 88]. For example, ^1H chemical shifts of 10-17 ppm were reported for different PA containing materials, including benzene phosphonic acid. It was claimed that the shorter the O...O distance the higher the chemical shift. By analogy, a chemical shift of 9.9 ppm for the PA signal indicates a rather moderate hydrogen bond strength [FREY 04] between PA groups of the HEXAGON and a relative large distance between them, see spectrum at the bottom in Figure 4.4. It is also probable that the PA groups of the ionomers form hydrogen bonds with residual or incorporated water contained in the system. Taking into account that

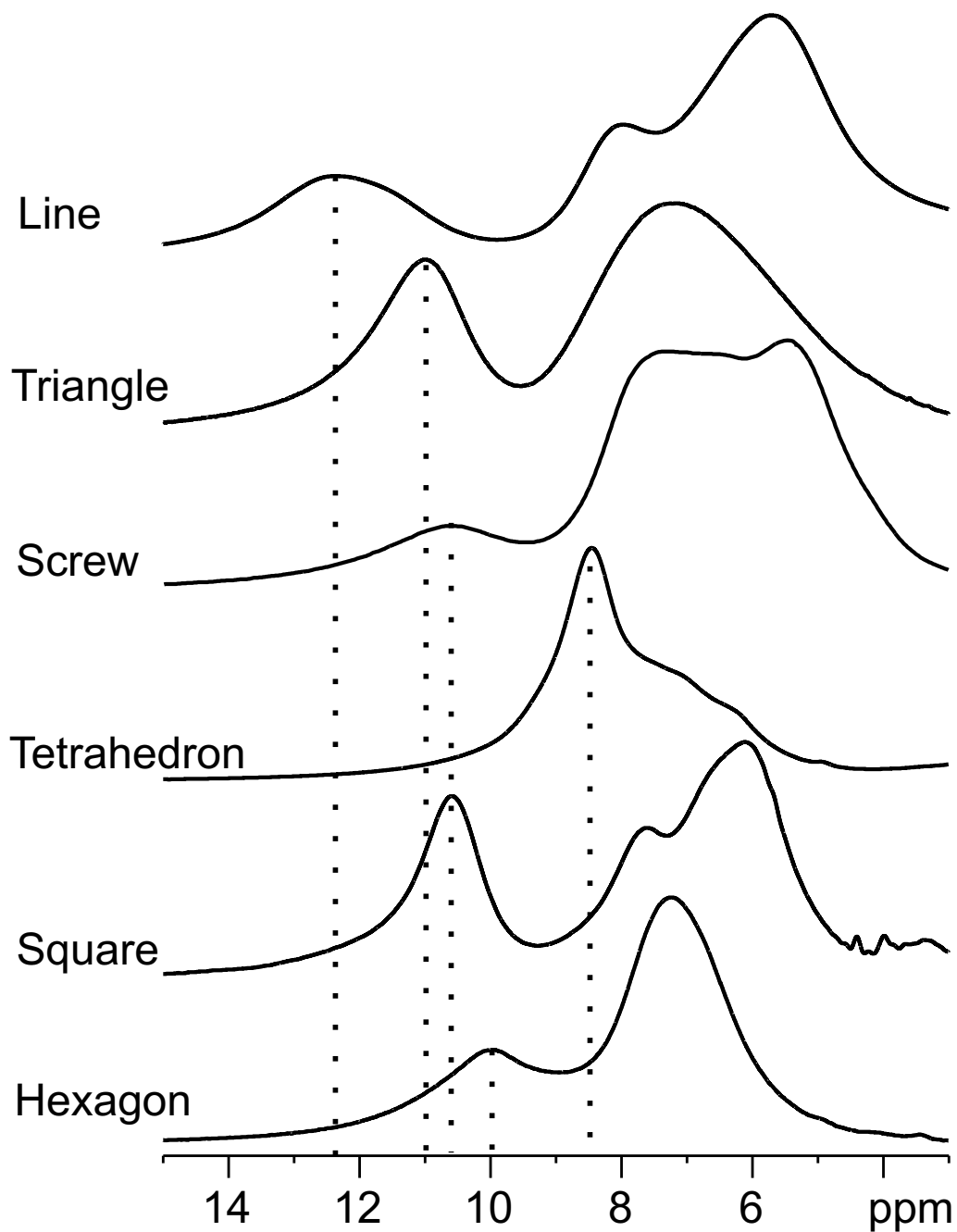


Figure 4.4: Comparison of ^1H MAS NMR spectra recorded at 30 kHz spinning (700.1 MHz, 16.4 T) for the different geometrical shapes at ambient conditions. Plotted from the top to the bottom with increasing number of PA.

liquid water itself gives rise to a resonance at 4.8 ppm, a gradual shift towards lower frequencies is predicted when the content of the water increases. This is a result of the fast proton exchange between the PA and the water which averages the δ_{iso} to an averaged value. A resonance representing a highly ordered water based hydrogen bonded network is "standard" ice where the chemical shift in the ^1H MAS NMR spectrum is approximately at 5.8 ppm [RHIM 79, PFROMMER 00].

High-resolution ^1H MAS NMR is a versatile tool to reveal information about supramolecular interactions, such as hydrogen bonding [BROWN 07]. Since the proton chemical shift value is highly sensitive to structural changes, it can display the strength of bonds and dynamics in the system. In particular, increasing hydrogen bonds strength is observed as the proton resonance frequency of the PA is shifted towards lower field [HARRIS 89, GERVAIS 04]. Tentatively, one would expect similar NMR spectra for all samples as they contain the same functional group added to the similar moiety. Therefore, it is of interest to compare the chemical shift of the corresponding PA signals for different geometrical shapes, as illustrated in Figure 4.4. The PA resonances range from 8.5 ppm to 12.3 ppm reflecting a wide spread of different hydrogen bonds strength. The PA resonances of the LINE represent the highest chemical shift. Additionally, it shows a relative broad line width of approximately 1800 Hz (4 ppm) compared to the SQUARE with 675 Hz (1.5 ppm), indicating that the PAs in the SQUARE are organized in a better ordered microstructure. In general, the chemical shift ranging from 8.5 to 12.3 ppm for the PA signal indicate rather moderate hydrogen bond strength [FREY 04] between PA groups. Especially, the small δ_{iso} values could also represent fast proton exchange between the PA and incorporated water which results in an averaged resonance between the extremities.

4.3 Probing the microscopic proton mobility in the ionomers

4.3.1 Proton mobility revealed by ^1H DQ MAS NMR

In principle, local proton mobility represents a major condition for enabling sufficient bulk proton conductivity. Insights into the proton dynamics of rather dry PEM materials were obtained from both DQ and VT ^1H MAS NMR experiments. A DQ signal is lost due to efficient averaging of ^1H dipolar couplings and can only be observed if the two involved protons are located within an appropriate distance to each other. Using the shortest recoupling time of one rotor period, distances up to 3.5 \AA can be observed [SCHNELL 01].

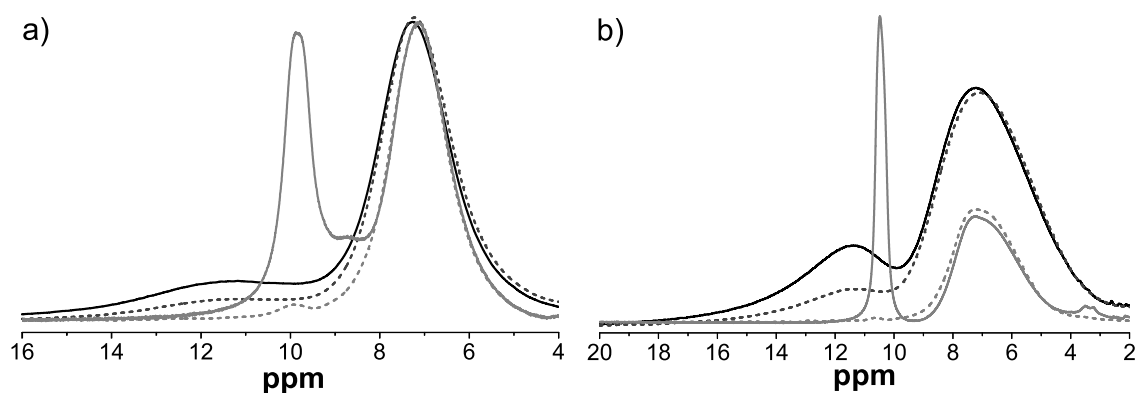


Figure 4.5: Comparison of the ^1H (solid line) and ^1H DQF (dashed line) MAS NMR spectra recorded using a spinning frequency of 29762 Hz (700.1 MHz, 16.4T).

a) HEXAGON recorded at -6°C (black) and 127°C (dark grey) and b) TRIANGLE recorded at -6°C (black) and 108°C (dark grey).

The signal intensity decreases with increasing distance. Another reason for decreasing signal intensity is higher molecular motion. Above the glass temperature (T_g) the line narrowing are attributed to a reduction of dipolar coupling due to faster motion. This leads to a complete loss of the hydrogen-bonded proton resonance and a significantly reduced intensity of the aromatic protons. The higher the mobility of a proton the less intense the signal which is detected after the DQ filter. Fortunately, all of the investigated structures show in the DSC graph the absence of a glass transition. Thus, all changes in

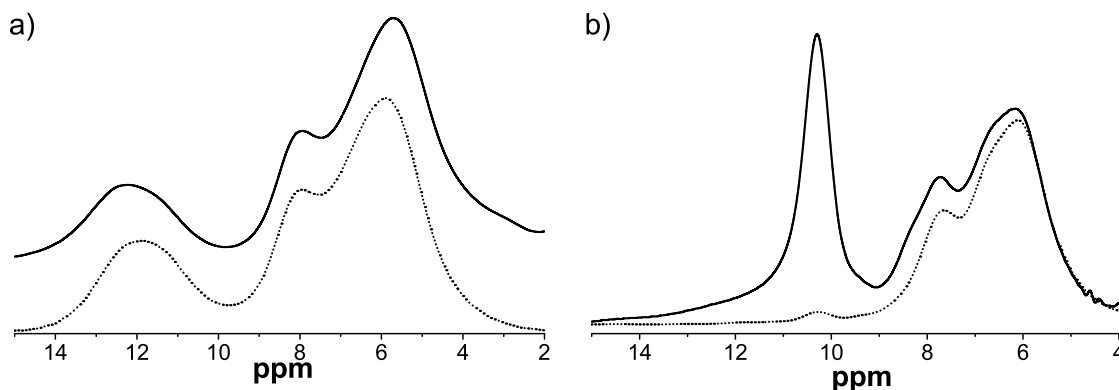


Figure 4.6: Comparison of the ^1H (solid line) and ^1H DQF (dashed line) MAS NMR spectra recorded using a spinning frequency of 29762 Hz (700.1 MHz, 16.4T).

a) LINE recorded at 51°C and b) SQUARE recorded at 108°C.

the ^1H DQF signals are related to mobility changes or relaxation. The ^1H and ^1H DQF spectra at different temperature are compared using HEXAGON and TRIANGLE as examples, see Figure 4.5.

All ionomers are in the solid state in the observed temperature range. Thus, information about the proton mobility are revealed by comparing the ^1H and ^1H DQF MAS NMR spectra at the same temperature. ^1H MAS and DQF spectra were recorded at selected temperatures between -6°C and 127°C . In the spectrum in Figure 4.5a and b one can observe that the aromatic protons signal intensity remains relatively constant, but there is a decrease in signal intensity of the PA corresponding resonance. Since the ^1H DQF spectra only includes the rigid protons present in the sample the signal loss of the PA is an indication of highly mobile PA protons. The decrease of signal intensity becomes more pronounced at higher temperatures. Thus, by increasing the temperature from -6°C to 127°C the signal loss in the HEXAGON increases from 10% to 98%, calculated by $\frac{I_{DQ}}{I_{singlepulse}} \cdot 100\%$. The TRIANGLE shows a similar behavior with 13% of PA signal left at low temperatures to nearly a 100% signal loss. In addition, the complete signal loss is reached already at a lower temperature of 108°C . The SCREW shows an increase of mobility from 7% to 95% at 127°C and the SQUARE from 12% to 97% at 90°C . The LINE, is the sample with the most immobile protons, showing a negligible loss of 1% at both RT and high temperatures, see Figure 4.6a. The signal loss of the TETRAHEDRON cannot be calculated since the overlap of the PA signal with the aromatic signal is too severe to

deconvolute the spectra reasonable.

4.3.2 Variable temperature ^1H MAS NMR experiments

^1H MAS NMR measurements performed at variable temperatures (VT) provide detailed information on local molecular mobility and dynamic processes present in the sample in question. In most cases, such local molecular dynamics lead to characteristic line broadening or narrowing, sometimes associated with a shift of the line. In particular, line narrowing at higher temperatures coincides with a change in line shape from a broad Gaussian to a narrow LORENTZIAN line [AKBEY 09]. Such changes can also be observed in the VT ^1H MAS NMR spectra of the presented geometrical shapes, as illustrated in Figures 4.7, 4.8, and 4.9. However, some of these samples show a somewhat different

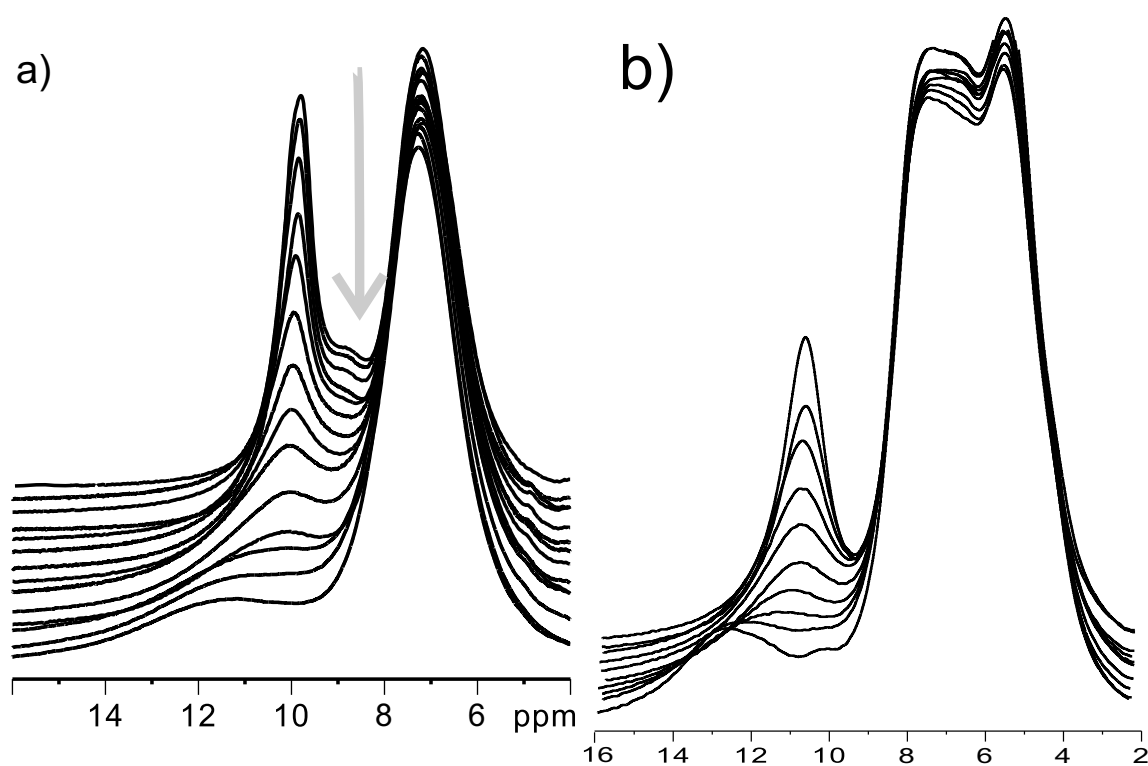


Figure 4.7: VT ^1H MAS NMR spectra at 30 kHz spinning (700.1 MHz, 16.4 T) measured at raising temperatures from bottom to top starting with -6 to 136°C in $\sim 10^\circ\text{C}$ steps.
a) HEXAGON b) SCREW

behavior. A significant continuous decrease in line width, while raising the temperature

is characteristic for proton mobility [SCHUSTER 05, YE 06]. Indeed, some of the stack VT plots show this kind of behavior. The HEXAGON, the SCREW, the TRIANGLE, and the TETRAHEDRON show a rather strong effect on the temperature, c.f. Figure 4.7 and 4.8. The HEXAGON and the SCREW show a complex temperature dependency for the ^1H signal assigned to the hydrogen bonded protons. In addition to line narrowing, a change of the chemical shift can also be observed for the VT stack for both the HEXAGON and the SCREW, c.f. Figure 4.7a and b. The ^1H MAS NMR spectrum of the HEXAGON, as seen in Figure 4.7a, shows a broad distribution of different ^1H PA sites at -6°C . Around 26°C the chemical shift of the HEXAGON shifts 2 ppm towards higher field from 12 to 10 ppm. A further increase of the temperature leads to a narrowing of the signal. At higher temperatures two signals originating from hydrogen bonds are observed with the minor one located at 8.5 ppm, as seen in Figure 4.7a (light grey arrow). This observation supports the assumption of a microstructure consisting of different sites with a minor compound of $\sim 5\%$ quantified by deconvolution. The ^1H MAS NMR spectra of the SCREW, shown in Figure 4.7b, on the other hand display two relatively broad peaks at -6°C , while there is just one hydrogen bond attributed signal at higher temperatures. This behavior is commonly known and can be explained by an averaged equilibrium of different sites [GOWARD 02]. In the VT ^1H MAS NMR stack of the SCREW a change of the chemical shift from 13 to 11 ppm is observed. Here, the modification is rather a stepwise transition in the temperature range from 26 to 46°C , see Figure 4.7b. This observation has already been reported for poly (vinyl triazole) derivatives (PVTz) [AKBEY 09]. In contrast to PVTz, the SCREW does not impose a continuous shift toward lower ppm values. In the PVTz most of those characteristics are explained by a chemical exchange processes between the $\text{NH}\cdots\text{N}$ hydrogen bonded and the non-hydrogen bonded states. Thus, in analogy the SCREW might also reflect a formation and breaking of hydrogen bonds. A further difference to the SCREW is that PVTz shows the described change of the chemical shift at the T_g .

Rather constant ^1H MAS NMR line widths suggest an absence of fast ^1H mobility on the NMR timescale. This behavior is anticipated in the case of the LINE, see stack plot in Figure 4.9a, which is based on the results obtained from ^1H DQF MAS NMR in subsection 4.3.1. Unlike in the case of the LINE, the rather constant line width observed in the SQUARE is unexpected, since the ^1H DQF MAS NMR spectra reflect a high

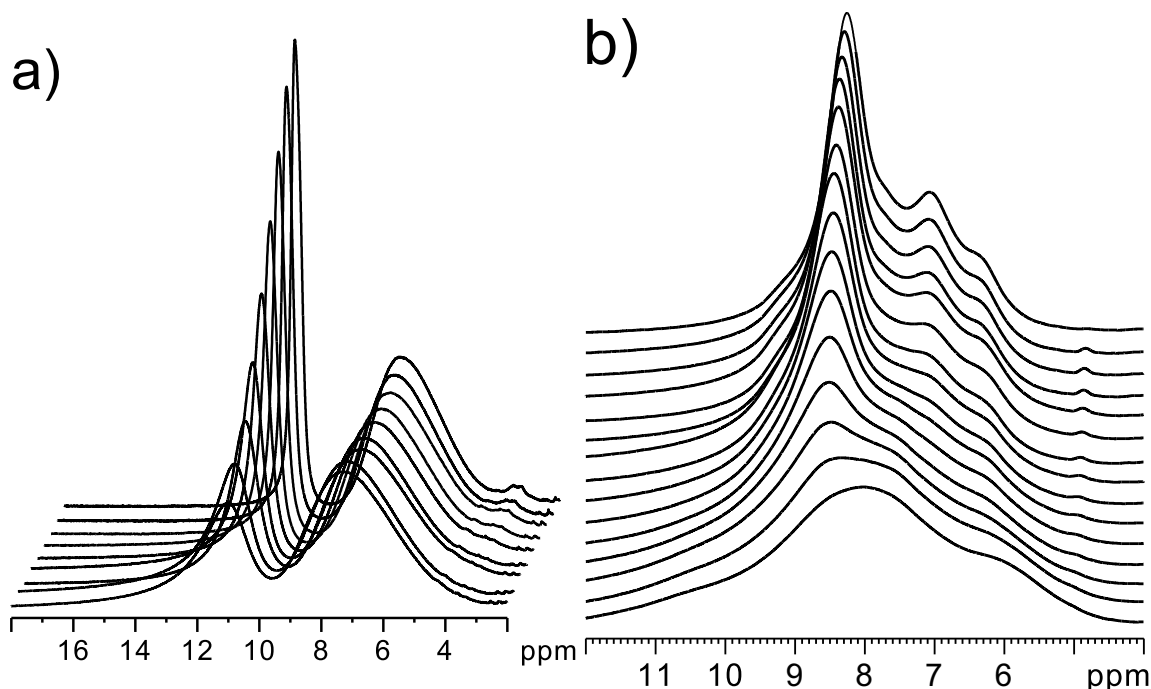


Figure 4.8: ^1H NMR spectra at 30 kHz MAS and 700.1 MHz variable temperature measurement from -6 to 136°C in $\sim 10^\circ\text{C}$ steps
 a) TRIANGLE b) TETRAHEDRON

mobility of the PAs, see Figure 4.9b.

The overall change of the PA corresponding resonance for all of the investigated ionomers can more easily be compared in the ARRHENIUS-type plot, shown in Figure 4.10. Here, the slopes of the LINE and the SQUARE superimpose, suggesting similar mobilities of the PA which contradicts the DQF results of the SQUARE in subsection 4.3.1. Thus, the signal loss in the ^1H DQF MAS NMR spectra of the SQUARE has to be related to an additional structural feature, e.g. a distance of the PA bigger than 3.5 \AA . In general, however, the low local mobility of the LINE and the SQUARE is in good agreement with the low bulk conductivity.

Intuitively one would assume that higher activation energies are found for protons among strongly hydrogen bonded positions. However, in case of PA-containing polymers, such a simple relation of hydrogen-bond strengths and local proton mobility was not observed [BRUNKLAUS 09]. A comparison of the apparent E_A derived from VT

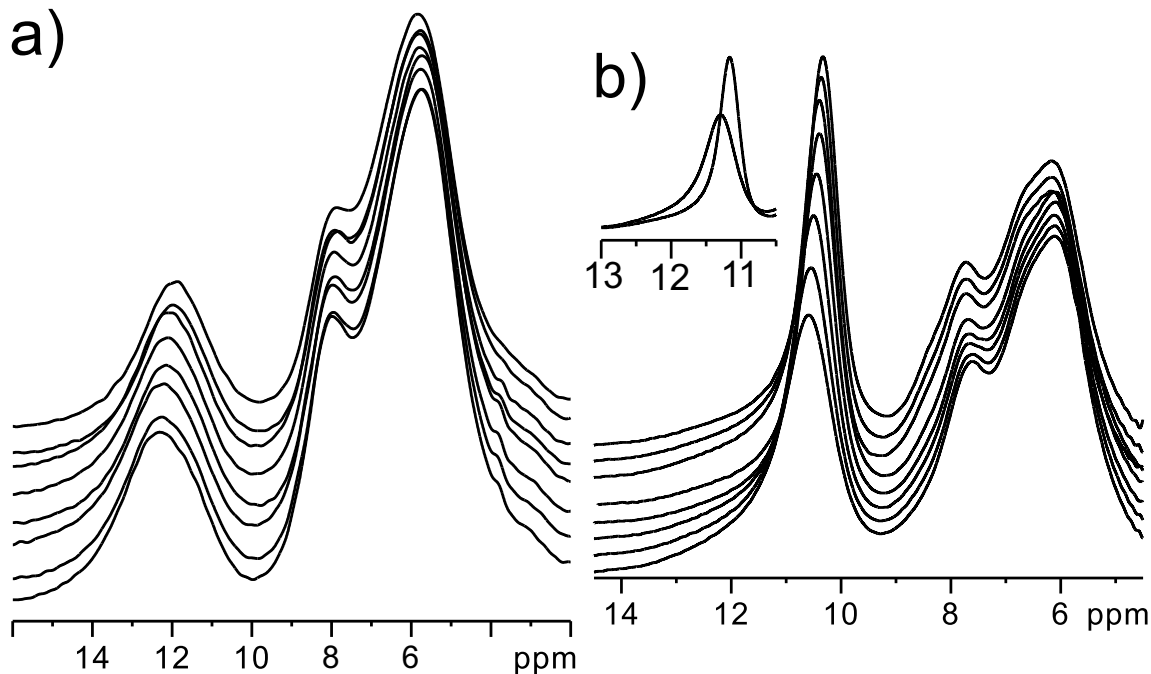


Figure 4.9: VT ^1H MAS NMR spectra at 30 kHz spinning (700.1 MHz, 16.4 T) measured at raising temperatures from bottom to top starting with 46 to 136°C in $\sim 10^\circ\text{C}$ steps.
a) LINE b) SQUARE

^1H MAS NMR of the ionomers reveals two different classes, see Table 4.2.

Geometrical shape	$\delta_{iso}(^1\text{H})_{PA}$ [ppm]	$E_A(NMR)$ [kJ/mol]	$E_A(IS)$ [kJ/mol]	$\bar{\sigma}_{DC}$ [S/cm] 140°C
Linear	12.3	2.1	30.7	$1.33 \cdot 10^{-6}$
Triangle	11.0	17.7	29.5	$5.3 \cdot 10^{-3}$
Screw	10.6	18.5	28.5	$9.62 \cdot 10^{-6}$
Tetrahedron	8.5	4.2	37.6	$1.13 \cdot 10^{-4}$
Square*	10.6	2.5	31.0	$1.08 \cdot 10^{-5}$
Hexagon	9.9	15.2	27.7	$2.78 \cdot 10^{-3}$

Table 4.2: Comparison of the chemical shift for the hydrogen bonded protons with the activation energy obtained by VT ^1H MAS NMR and impedance spectroscopy (IS), including the DC conductivity of the samples at 140°C (* - After annealing)

The first, comprising the LINE, TETRAHEDRON, and SQUARE, show E_A values lower

than 5 kJ/mol indicative of a rotational or tumbling motion. For the remaining structures TRIANGLE, SCREW, and HEXAGON, E_A values around 15-18 kJ/mol were obtained. Since activation energies of temperature-activated motional processes involving hydrogen bonds are generally in the range of 120 kJ/mol [GOWARD 02], the obtained apparent activation energies cannot be attributed to a single thermally activated process. Notably, in rather ideal cases, where the NMR data reflect the proton motions responsible for observable bulk proton conductivity, the E_A obtained from both the VT ^1H MAS NMR and IS are similar [YE 06]. In the IS measurements all geometrical shapes show an E_A of roughly 30 ± 5 kJ/mol at dry conditions except for the TETRAHEDRON with 37.6 kJ/mol. These values are rather small compared to PVPA with 58 kJ/mol [BINGOEL 06]. This deviation of the measured E_A indicates an overlap of different contributing sites

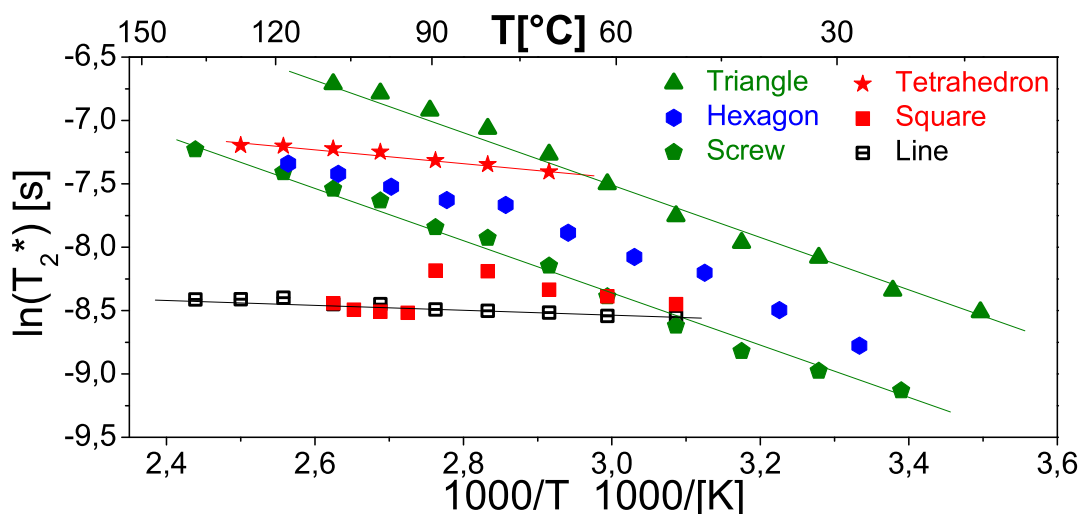


Figure 4.10: The ARRHENIUS plot shows the change in line width against the inverse temperature. From the slope the E_A is extracted shown exemplarily for the LINE, TETRAHEDRON, TRIANGLE, and SCREW. Samples with low E_A LINE, TETRAHEDRON and SQUARE. and with high E_A TRIANGLE, SCREW, and HEXAGON The obtained E_A of all geometrical shape are listed in Table 4.2.

averaging to a rather small absolute value. The "impurity" observed in the VT ^1H MAS NMR spectra of the HEXAGON, indicated by the grey arrow in Figure 4.7a, could be one site with a different dynamics affecting the overall E_A both in NMR and IS. This different resonance might be due to a PA-water interaction, also found in the case of

PVPA [KALTBEITZEL 07].

The apparent E_A of the TRIANGLE, SCREW, and HEXAGON observed in NMR are roughly 10 kJ/mol smaller compared to IS values. The discrepancy between the two measurements is attributed to the fact that the conductivity data represent charge transport on a *macroscopic* scale, while NMR detects the proton mobility on a *microscopic* scale. Local proton mobilities, however, include different types of motions which not necessarily contribute to the long-range proton transport that facilitates bulk proton conductivity.

Additionally, it has to be considered, that the conductivity scale discussed in impedance spectroscopy is based on a \log_{10} scale while the mobility in VT ^1H MAS NMR is plotted against the \ln . Therefore, comparing two samples in IS with a difference of two orders of magnitude is more pronounced than it is in the NMR plot. The ionomers show a variation of absolute values and apparent activation energies, resulting from the VT ^1H MAS NMR experiments in the range of two orders of magnitude. At the same conditions there is a difference of several orders of magnitude in IS exceeding the NMR data. Thus, the different proton conductivities obtained by IS cannot be attributed to the difference in PA mobility.

Nevertheless, the activation energies obtained from the VT ^1H MAS NMR experiments contain information about the local mobility. In Figure 4.10 the slopes of the different geometrical shapes are compared. An interesting aspect is that some of the samples show almost identical slopes for the same absolute values in line width and this even considering that the PA signal is located at different chemical shifts. In this very case it seems that there is no linear dependency between the hydrogen bond strength and the E_A results [STEININGER 07]. Hence, one has to be careful when correlating E_A values with the chemical shift of the PA.

4.3.3 Comparison of macroscopic and microscopic conductivity

The previous NMR studies discussed in this section monitor local dynamic processes of the PA groups which contribute to anhydrous proton conduction. However, *macroscopic* transport leading to high proton bulk conductivity, has additional requirements on the *microscopic* length scale. Thus, extrapolation from local processes accessible by spectroscopic NMR methods to *macroscopic* transport is not straightforward [AKBEY 09].

When analyzing the activation energies obtained from VT ^1H MAS NMR one has to keep on mind, that such values may reflect several contributing motions and it is not clear whether or not this method show the actual E_A . For proton conduction based on a single thermally activated process an E_A in a range of 20-40 kJ/mol [YE 06] is found. Furthermore, these results showed that within the working temperature range, small values most likely represent an overlap of two or more processes. This could explain the rather small E_A values for the HEXAGON and TRIANGLE, showing high bulk conductivity.

4.3.4 Water uptake behavior of the HEXAGON

It is known from the bulk conductivity data, discussed in section 4.1, that water strongly affects the conductivity of all geometrical structures. Since the HEXAGON shows a fairly high conductivity of nearly $3 \cdot 10^{-3}$ S/cm it is of particular interest to investigate this in more detail. The water uptake curve of the HEXAGON is shown in Figure 4.11. The adsorption and desorption are plotted against the relative humidity (RH). The procedure was as follows, the sample was stored two days at different RH and then weighted using a microbalance. The graph displays a hysteresis between adsorption and desorption indicating that the water release is hindered which is often observed in hydrates [BUELL 36]. To reveal the origin of this mechanism, variable temperature (VT) experiments of ^1H and ^{31}P MAS NMR experiments under different RH were studied.

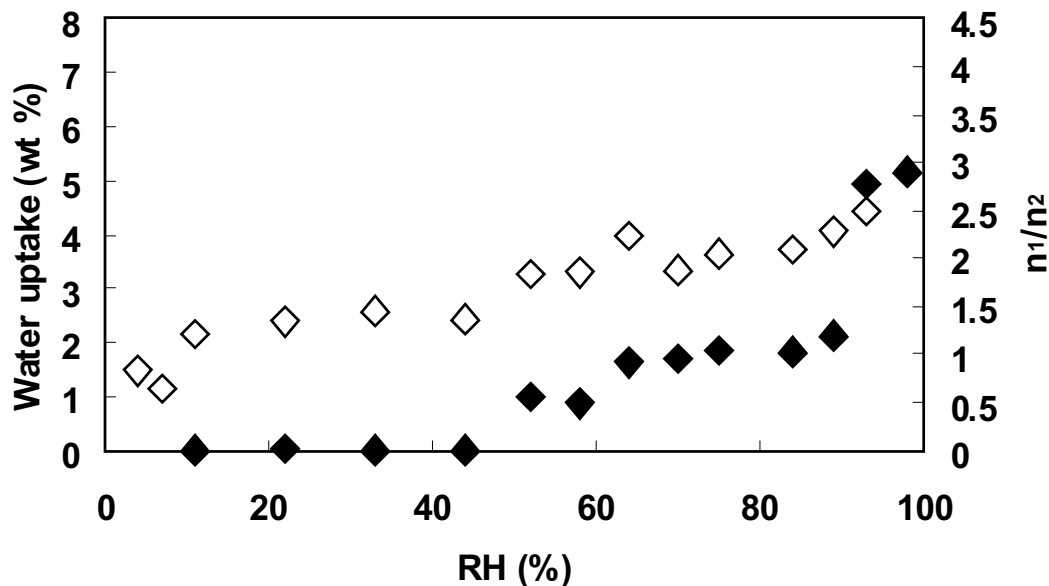


Figure 4.11: Water uptake graph of the HEXAGON: Water adsorption full diamonds and desorption open diamonds isotherms as function of RH [%] with n_1/n_2 indicating number of water molecules per HEXAGON [JIMENEZ 09]

By comparison of the different ^1H MAS NMR spectra in Figure 4.12a, one can observe

that the amount of water present in the sample, changes the chemical shift of the hydrogen bonded PA. This plot of ^1H MAS NMR spectra shows from top to bottom first a dried sample (light grey) which than has been stored under 100% RH (dark grey) and finally dried again (black). In Figure 4.12a one can see that the ^1H MAS NMR spectrum depends critically on the sample history since the release of water after exposing it at 100% RH is inhibited. This, is in agreement with the water uptake curve, shown in Figure 4.11. The freshly obtained and subsequently dried sample shows relatively broad lines, where the isotropic chemical shifts at higher temperature moves slightly towards lower frequency, as already discussed in subsection 4.3.2. After storing the sample at 100% RH it becomes waxy indicating water adsorption and possibly incorporation of water. As expected, the water has a strong influence on the both ^1H and ^{31}P MAS NMR spectra [JIANG 08]. It was observed, that the PA resonance in the ^1H MAS NMR spectrum of the dried HEXAGON is located at 10.0 ppm and upon water uptake shifts towards 8.2 ppm. Additionally, the dried sample shows two relatively broad peaks located at 6.5 and 5.4 ppm. The presence of these signals support the assumption of more possible PA-water interaction sites in the sample. Notable, for "wet" PVPA a $\delta_{iso}(^1\text{H})$ of 6.5 ppm was also observed and assigned to a PA-water interaction, while the signal at 5.4 ppm may reflect water-water interaction.

Figure 4.12b shows the ^{31}P MAS NMR spectra of the HEXAGON treated in the same manner as the ^1H MAS NMR spectra mentioned above. Here, the ^{31}P line width depends on the amount of water as a result of the higher mobility due to incorporated water molecules. In addition, the signal at 18 ppm shows a splitting when the sample has been exposed to 100% RH, supporting the presence of distinct PA sites in the bulk. Hence, if the line width also reflects the variation of different sites present in the bulk, the water also affect the PA surroundings, e.g. different hydration shells. The black ^{31}P MAS NMR spectrum of the HEXAGON shown at the bottom of Figure 4.12b displays a line width even smaller than in the "wet" state and at smaller δ_{iso} values. This observation suggests that higher chemical shifts might correspond to PA which do not interact with a water molecule. In literature, a chemical shift change due to water uptake has been reported for PVPA [KALTBEITZEL 07]. Here, calculations have been done leading to a linear relation between the observed proton chemical shift and the fraction of protons originating from water. For PVPA a shift of approximately 1 ppm, as found

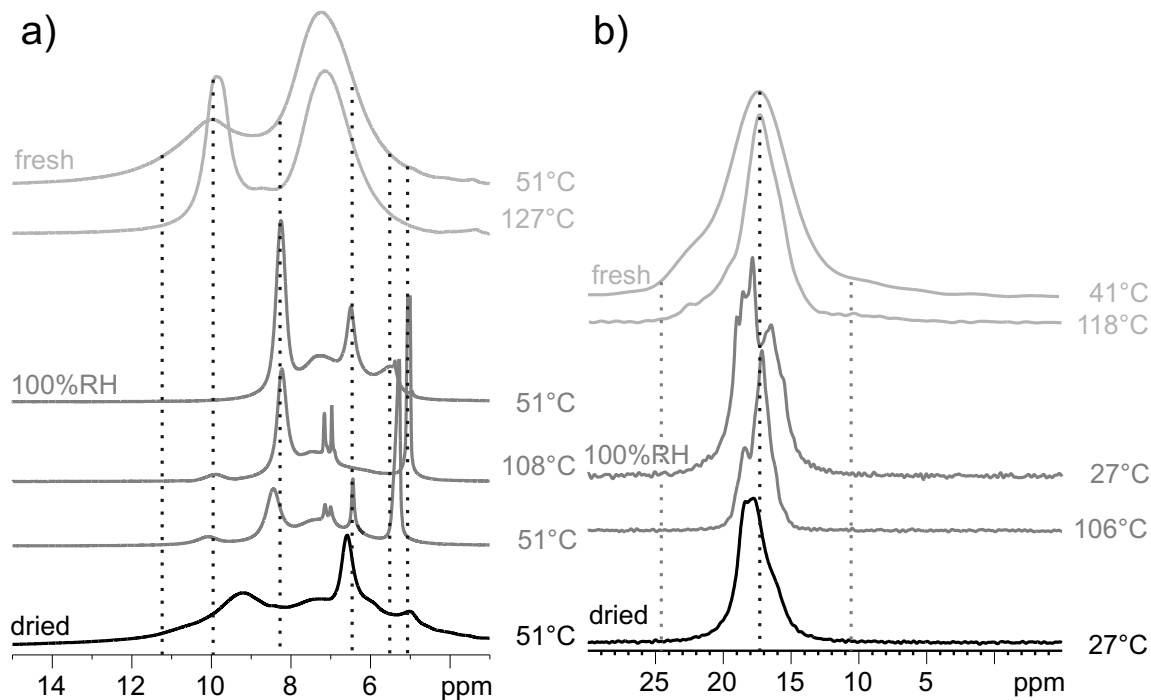


Figure 4.12: Comparison of the effect of RH on the HEXAGON. a) ^1H MAS NMR spectra recorded at 30 kHz spinning (700.2 MHz, 16.4 T) from the top: freshly obtained sample at 51 and 127°C (light grey), stored at 100% RH 51 and 108°C (dark grey), and stored at 100% RH and dried at 150°C under nitrogen flux at 51°C (black). b) ^{31}P MAS NMR spectra recorded at 15 kHz spinning (283.2 MHz, 16.7 T) from the top: freshly obtained sample at 41 and 118°C (light grey), stored at ambient conditions at 33 and 112°C (grey), stored at 100% RH 27 and 106°C (dark grey), and stored at 100% RH and dried at 2 hours 150°C under nitrogen flux at 27°C (black).

in the HEXAGON would represent the absorption of one water molecule for each PA. In agreement to the ^{31}P data the ^1H MAS NMR spectrum of the HEXAGON shows a signal as a result of sample exposure to water located at 6.5 ppm. This signal does not disappear after drying the sample at 150°C up to 1 day implementing an irreversibility of distinct incorporated water molecules.

The VT ^1H MAS NMR experiments of the HEXAGON stored at 100% RH, as shown in Figure 4.13a, again indicate a drastic influence of the incorporated water on the PA groups. By heating the sample, the change in the signals implies a fast exchange between the different sites. The resonance at 8.2 ppm first moves towards 8.4 ppm before it

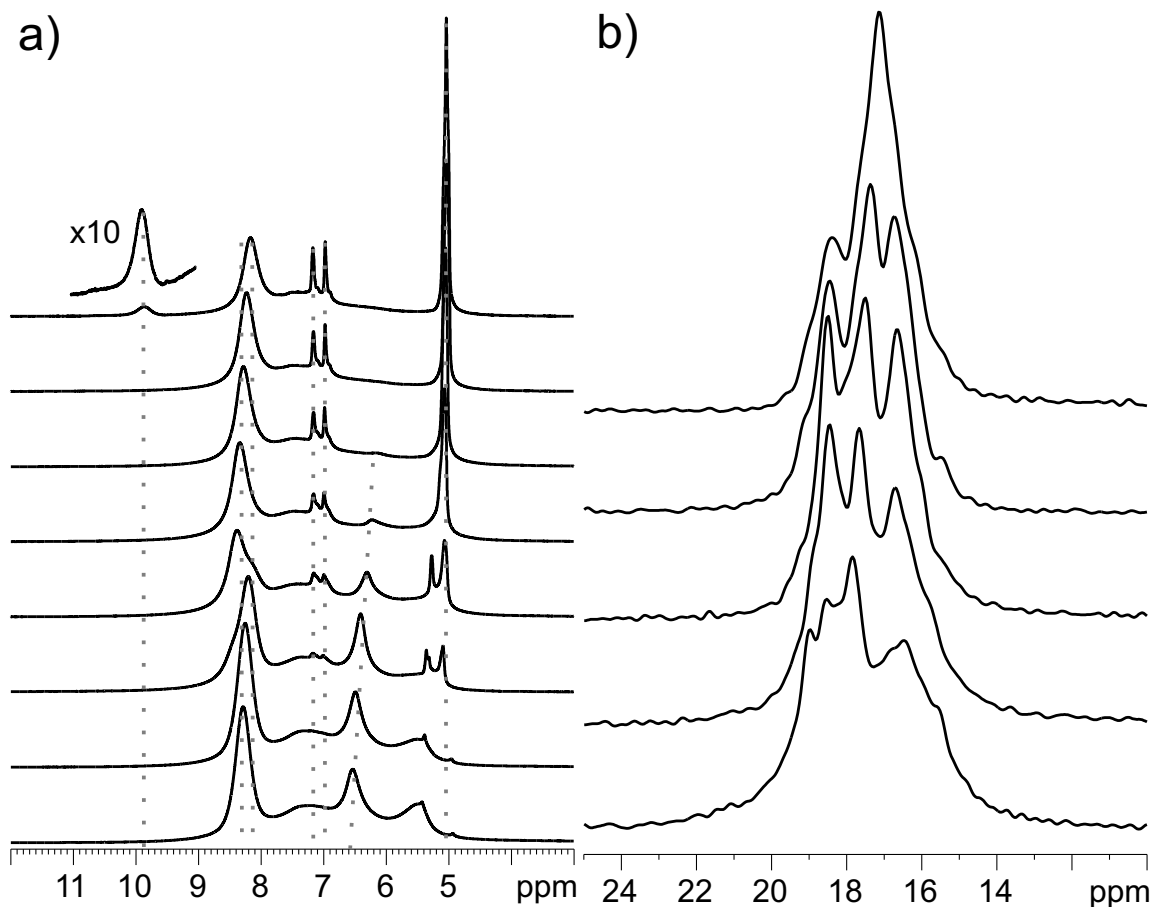


Figure 4.13: VT experiment of the HEXAGON after the sample has been stored at 100% RH a) ^1H MAS NMR spectra recorded at 30 kHz spinning (700.2 MHz, 16.4 T) in a temperature range starting from the bottom at 51 to 108°C in steps of $\sim 10^\circ\text{C}$. b) ^{31}P MAS NMR spectra recorded at 15 kHz spinning (283.2 MHz, 16.4 T) in a temperature range starting from the bottom at 28 to 107°C in steps of $\sim 10^\circ\text{C}$.

finally returns to the original ppm value at 108°C and remains unaffected by the cooling afterwards. The signal at 6.5 ppm decreases, while shifting to 6.3 ppm and vanishes at 91°C. After cooling the sample it is detected again, however, with a smaller line width than before. This value is very close to the value of 5.8 ppm for the hydrogen bonds obtained in ice [RHIM 79, PFROMMER 00], suggesting that this signal represent the incorporated water molecules located in a strong hydrogen bond network which are in a fast exchange with other water sites at higher temperatures. The intensity of the resonance at 5.5 ppm first decreases with increasing temperature before it splits into two sharp peaks located at 5.4 and 5.2 ppm. These peaks combine into one very sharp peak

at 5.1 ppm most probably corresponding to bulk water since it stays stable after cooling. Moreover, two additional sharp peaks at 7.5 and 7.2 ppm start to appear at 75 °C. At 108°C a signal at 9.9 ppm grows and remains after cooling. This resonance has the same chemical shift as the PA hydrogen bond signal in the fresh sample.

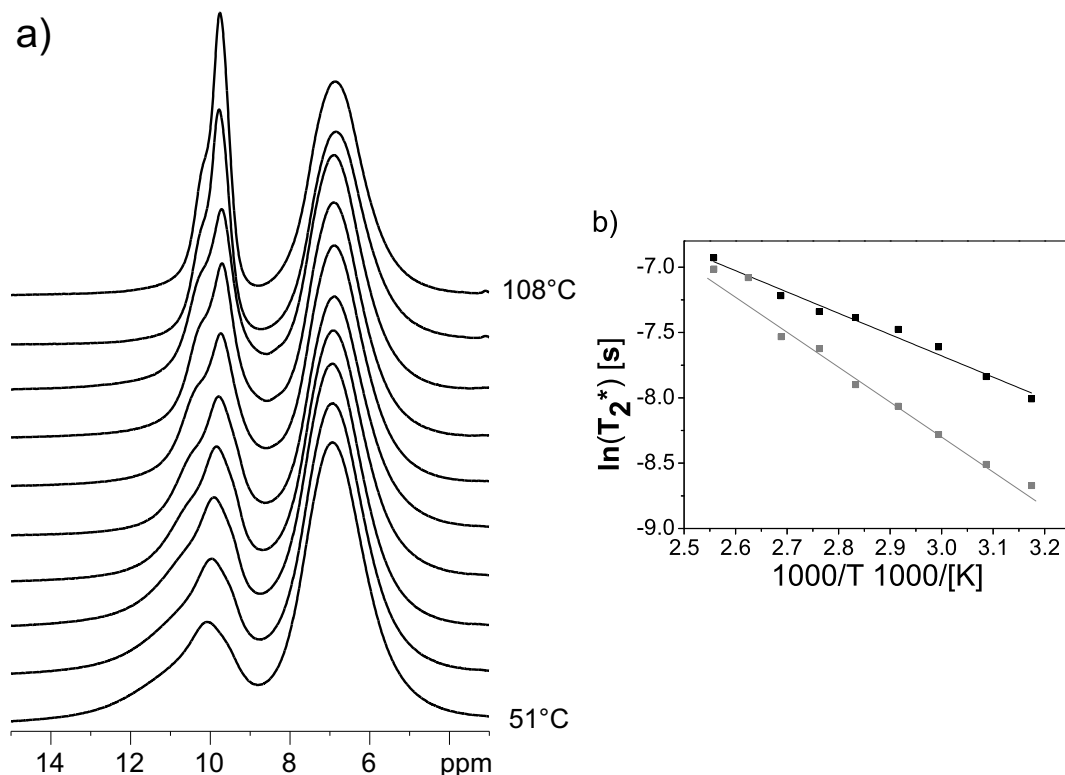


Figure 4.14: a)VT ^1H MAS NMR spectra of the HEXAGON recorded at 30 kHz spinning (700.2 MHz, 16.4 T) measurement from the bottom to the top starting at 51 - 108°C in steps of $\sim 10^\circ\text{C}$ stored at ambient conditions.

b) In the ARRHENIUS plot the line width of the two PA signals at 10.1 ppm and 11.3 ppm are plotted against the inverse temperature. The E_A values are obtained from linear plotting 13.5 kJ/mol (10.1 ppm) and 23.0 kJ/mol (11.3 ppm).

The observations in the VT ^1H MAS NMR spectra of the HEXAGON given above might correspond to a change in the structure where water exchanges its position relative to the PA. After drying the sample, see spectrum at the bottom in Figure 4.12a, water surrounded by other water molecules is released while the signal at 6.5 ppm corresponding to the incorporated water stays. In addition, the peak at 8.2 ppm broadens and shifts towards lower field indicating that the amount of water in direct contact to PA decreases.

In the VT ^{31}P MAS NMR spectra of the HEXAGON an averaging of the ^{31}P sites is observed, shown in Figure 4.12b. In the beginning several sites spread between 16 and 20 ppm are observed. When heating the sample, three major resonances emerge at 19, 18, and 17 ppm. This observation reflects an averaging of the PA in fast exchange at higher temperature.

An additional matter of interest is how the HEXAGON interact with water when it is kept at ambient conditions over a long period. Since the water uptake curve shows no adsorption up to 43% RH a drastic change as observed in Figure 4.13a is not expected. Nevertheless, water from air interacts with the substance on a long time scale as indicated by the ^1H MAS NMR experiment of the sample stored at ambient conditions over half a year (Figure 4.14a). The resonance corresponding to the PA groups indicates a slight narrowing and a better resolution of the different PA sites in the ^1H MAS NMR spectrum of the HEXAGON. This renders possible to deconvolute the different PA signals and to obtain their different E_A , see Figure 4.14b. The ARRHENIUS-type plot reveals that the two different hydrogen bonds have different E_A , supporting the assumption that the values compared in section 4.1 represent apparent E_A . In the case of the HEXAGON, the higher δ_{iso} value at 11.3 ppm has E_A of 23.0 kJ/mol, 10 kJ/mol higher than the peak at 10.1 ppm. This is consistent with the fact that higher δ_{iso} involve stronger hydrogen bonds and thus, higher the E_A are needed to break it [FREY 01, LEE 07a]. Thus, comparing the results of the HEXAGON with the findings from PVPA, the signal located at lower δ_{iso} (10.1 ppm) would represent a PA which has attached a water molecule, while the resonance at higher δ_{iso} (11.3 ppm) would be the PA hydrogen bonded protons which has no water in its surroundings. In contrast to the PVPA, the HEXAGON ^1H MAS NMR spectrum shows both species coexisting. The ratio between both resonances is constant at 1:1 over the measured temperature range consistent with 0.5 H_2O water molecules each PA.

4.3.5 Deuteron NMR of the HEXAGON

Since solid-state ^1H MAS NMR spectroscopy often does not provide well resolved peaks due to the small chemical shift distribution of the ^1H , ^2H MAS NMR spectroscopy of selectively labeled samples may be performed instead. Furthermore, provided that there are no changes in the hydrogen bond structure, ^2H and ^1H chemical shifts are comparable within ± 0.2 ppm [GOLUBEV 09]. Two types of information can be extracted from ^2H NMR measurements. Fast MAS provides spectra similar to the ^1H data and can therefore be used for a line shape analysis at different temperatures. In cases where only one type of protons such as OH is labelled selectively, no disturbing peak overlap can occur. Information about the deuteron motion was obtained from static echo spectra. The obtained line shapes reflect local reorientations of the ^2H quadrupolar tensor and thus allow for insights into the geometrical shape of underlying motions [SPIESS 85].

In principle, PA can be deuterated by dissolving or suspending the sample in D_2O for two hours and freeze drying it afterwards [SCHAUFF 07]. However, the selective deuteration of all geometrical shapes seems to be more tedious than was expected in the beginning. Similar samples such as poly(styrene phosphonic acid) were already reported to yield only poor degrees of deuteration [BRUNKLAUS 09]. Therefore, different solvent mixtures such as Methanol: D_2O and different stirring times were used to obtain a complete deuteration of the sample. Rather complete deuteration of the protogenic group could be identified by the absence of a $\text{PO}(\text{OH})_2$ signal in the residual ^1H MAS NMR spectrum (see Figure 4.15a).

Notably, the resonance emerging in the ^2H MAS NMR spectrum of the HEXAGON, shown in Figure 4.15b, does not show the expected signal at 10 ppm. The fast ^2H MAS NMR measurements reveal different sites. At -30°C and 10°C sharp signals in the range of 6-7 ppm are found. This is a shift of 3-4 ppm towards lower ppm compared to the proton signal. Since a deuteration of the aromatic core is quite unlikely this resonance has to be correlated to the PA. Also, a chemical shift change of this dimension cannot be correlated to an isotope effect [DZIEMBOWSKA 01]. This resonance between 6 and 7 ppm, however, is comparable to the ^1H peak at 6.5 ppm attributed to PA interacting with water, as discussed in subsection 4.3.4. This signal can only be observed after exposing the HEXAGON to water which is not the case for the crude sample obtained

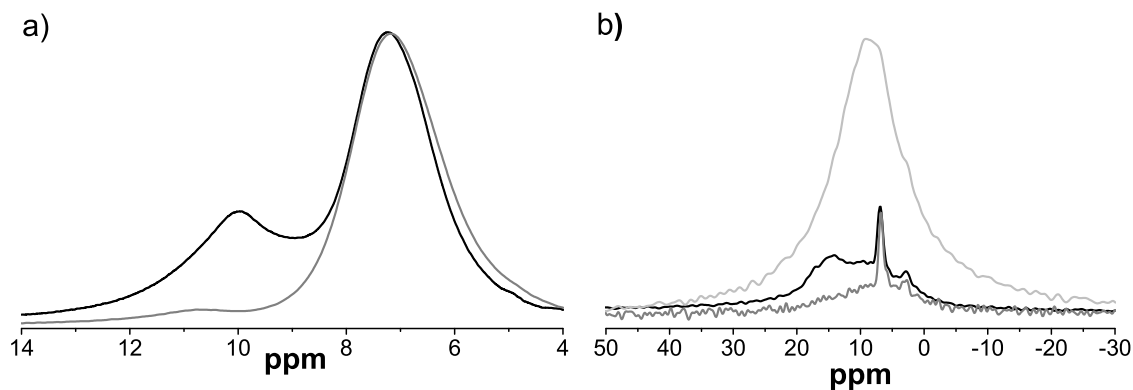


Figure 4.15: a) Comparison of the ^1H MAS NMR spectra recorded at 29762 Hz spinning (700.1 MHz, 16.4 T) at room temperature to prove the deuteration of HEXAGON (black) and HEXAGON-D (dark grey)
 b) ^2H MAS NMR spectra recorded at 29762 Hz spinning (107.5 MHz, 16.4 T) at different temperatures: -30°C (black), 10°C (dark grey) and 110°C (light grey).

from synthesis. Consequently, the history of the sample is a significant parameter. The spectrum at -30°C shows in addition to the discussed signal a broad underlying peak centered at ≈ 8 ppm. Here, the intensity for this resonance seems first to decrease with rising temperatures and increase again at an elevated temperature of 110°C where it is the only signal left is at 8 ppm with a line width of 1500 Hz, which can also be found in the ^1H MAS NMR spectrum of the wet HEXAGON, discussed in subsection 4.3.4. A similar thermal behavior was already reported for PA containing polymers [BRUNKLAUS 09]. Since only the PA was deuterated, the different signals have to origin from different PA-water interactions. In the ^1H MAS NMR spectrum the broad line would overlap completely with the aromatic resonance and hence, cannot be detected. The presence of irregularly incorporated water could explain the missing consistency of integrals obtained from ^1H spectral deconvolution. The ratio of the signal in the ^1H spectrum should be PA:aromatic 2 : 4. This, however, is not the case. At -30°C the ratio is 2 : 7 thus clearly supporting the presence of water molecules. In contrast, to the HEXAGON the LINE shows at the expected 2 : 2 : 4 ratio.

The presence of incorporated water can result in an exchange of ^1H between $\text{PO}(\text{OH})$ and H_2O . In general, the formation of a hydration shell is well known and supports this observation [DRACINSKY 09]. If this is the case in the HEXAGON the ^2H position

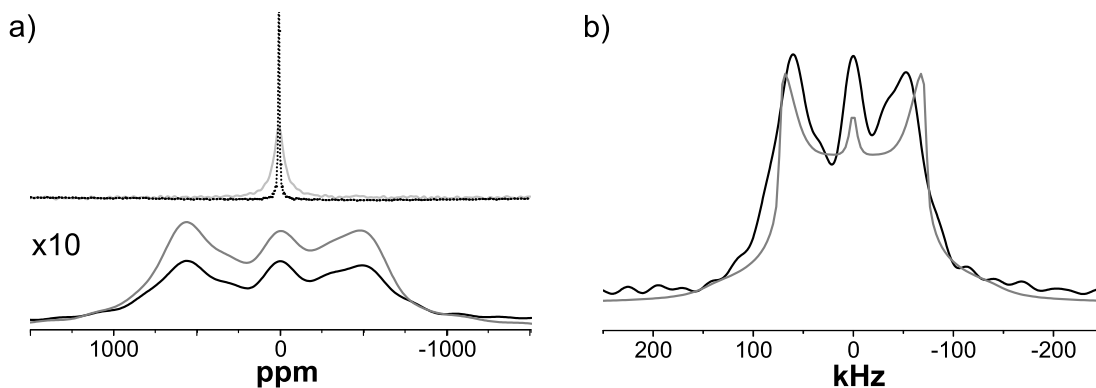


Figure 4.16: a) ^2H static NMR spectra of the HEXAGON (107.5 MHz, 16.4 T) at different temperatures: -30°C (black), 20°C (dark grey), 50°C (light grey), and 110°C (black-dotted) b) Comparing the ^2H static spectra for HEXAGON (black) at 107.5 MHz with the fit (grey) obtained from weblab with the following data: general case, two side jump, cone angle $\Theta = 54.7^\circ$, flip angle $\phi = 180^\circ$, jump rate 100 kHz.

is ill-defined. Consequently, a continuing exchange of $\text{POH} + \text{D}_2\text{O} \rightleftharpoons \text{POD} + \text{HDO}$ would affect the NMR spectra. This additionally would explain why the signal expected at 10 ppm is shifted to 7 ppm, see Figure 4.15b. This exchange between PA and water is also very fast and thermally easy to activate and could not be frozen to be measured even at the lowest temperatures. Thus, the signal at 10 ppm most likely does not appear in a single-pulse experiment due to fast exchange. Static ^2H solid-state NMR spectra might reveal further information. Depending on the temperature, the static HEXAGON spectra show two different motions, as shown in Figure 4.16a. At low temperatures there is a PAKE-line pattern underneath a narrow and isotropic peak. Since the sample is ill defined, the isotropic signal is located at the center but the PAKE-line pattern is not symmetrical distributed around it. Heating the sample, the PAKE-line pattern decreases while the isotropic signal increases which is similar to the behavior of PVPA [LEE 07b]. After one heating and cooling cycle the static measurement at the same temperature shows a higher content of the isotropic part. To ensure that this observation is not due a thermal non-equilibrium the experiment was repeated after an hour with the same result. This, however, indicates that a thermally activated exchange between the two different PA-water sites at 7 and 10 ppm occurs. Indeed, the spectral resolution of the low temperature PAKE-line pattern is not optimal due to motion. Thus, an educated guess can be given since it is known that PVPA shows a two-site jump [LEE 07b]. Due

to the fact that PVPA and the HEXAGON have both PA groups, the known parameters of PVPA were used as starting point to deconvolute the ^2H NMR spectra (WebLab [MACHO 01]). The obtained simulated spectrum shows some similarities to the measured one, c.f. Figure 4.16b, but does not fully reproduce the experimental line shape. Nevertheless, this result suggests again that more sites in the sample are interacting through a fast exchange mechanism.

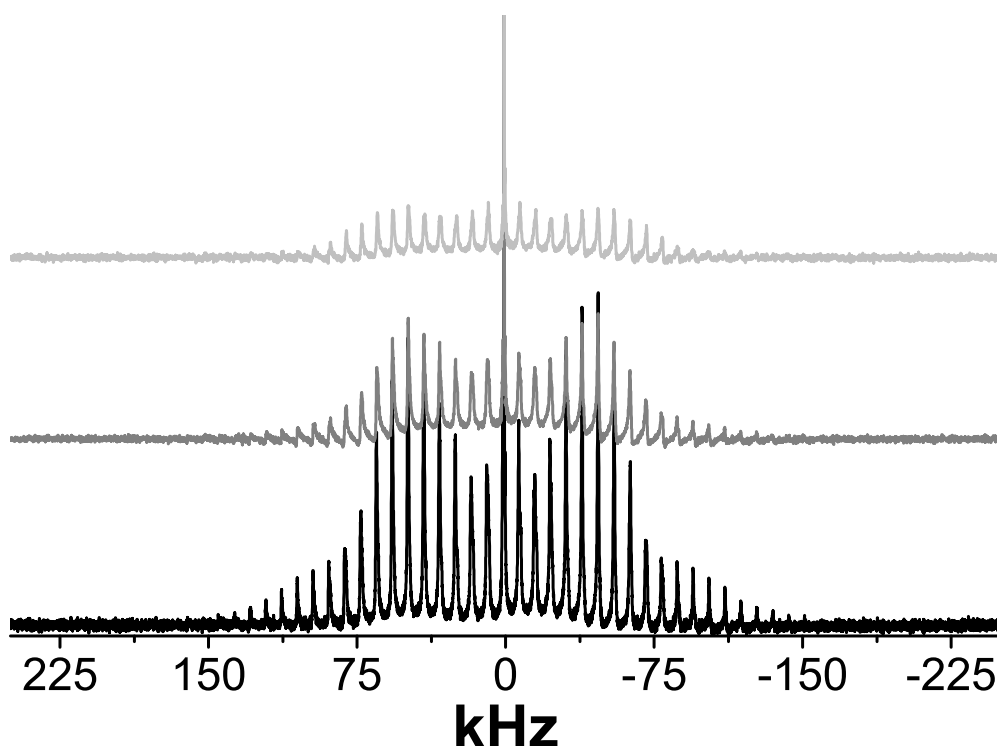


Figure 4.17: ^2H MAS NMR spectra of the HEXAGON at 7 kHz spinning (107.5 MHz, 16.4 T) at different temperature: -30°C (black), -10°C (dark grey) and 30°C (light grey).

The spinning sideband ^2H MAS NMR spectra of the HEXAGON show very persistent sideband patterns that hardly change their shape over temperature. This phenomenon is characteristic of rather rigid hydrogen bond systems. The maximum spectral extension of the spinning sidebands in the ^2H MAS NMR spectrum is observed for the rigid case at -38°C with a total width of 294 kHz, corresponding to a quadrupolar frequency of $\nu_Q = \frac{\omega_Q}{2\pi} \approx 147$ kHz. This value is roughly twice the value as reported in PVPA [SCHAUFF 07] and 1.5 times smaller compared to frozen $\nu_Q(\text{D}_2\text{O}) = 216$

kHz [LETELLIER 98]. In Figure 4.17 one can see that with increasing temperature the intensity of the signal decreases [SPIESS 81]. A similar behavior in ^2H MAS and static NMR signal has been reported for PVPA derivatives [BRUNKLAUS 09]. Intensity losses are often observed in the case when the molecular motion is in an intermediate regime, e.g., $\tau_c \sim \frac{1}{\nu_Q}$ is fulfilled. Here, τ_c denotes the correlation time and ν_Q the quadrupolar frequency defined in equation 4.2.

$$\nu_Q = \frac{\omega_Q}{2\pi} \quad (4.2)$$

4.3.6 ^{31}P NMR studies of the ionomers

^{31}P MAS NMR is an additional helpful tool to obtain structural information regarding the chemical structure and its surroundings [HARRIS 89]. In contrast to ^1H , ^{31}P is more sensitive to structure changes comprising a wider spreading of the chemical shift distributions, i.e. PA from 36 to 18 ppm [SCHAUFF 07]. In the liquid spectra the different geometrical shapes yield a spread of 2.5 ppm from the SQUARE at 11.7 ppm to the TETRAHEDRON at 14.0 ppm, c.f. Figure 4.18. Notably, the LINE and the TRIANGLE have exactly the same chemical shift. Since the solubility of the samples is rather poor one can assume that there is no packing effect in the solution. Furthermore, the poor solubility results in different effective concentrations which might also affect the chemical shift. Additionally, the central aromatic ring connecting the phenylphosphonic acids might

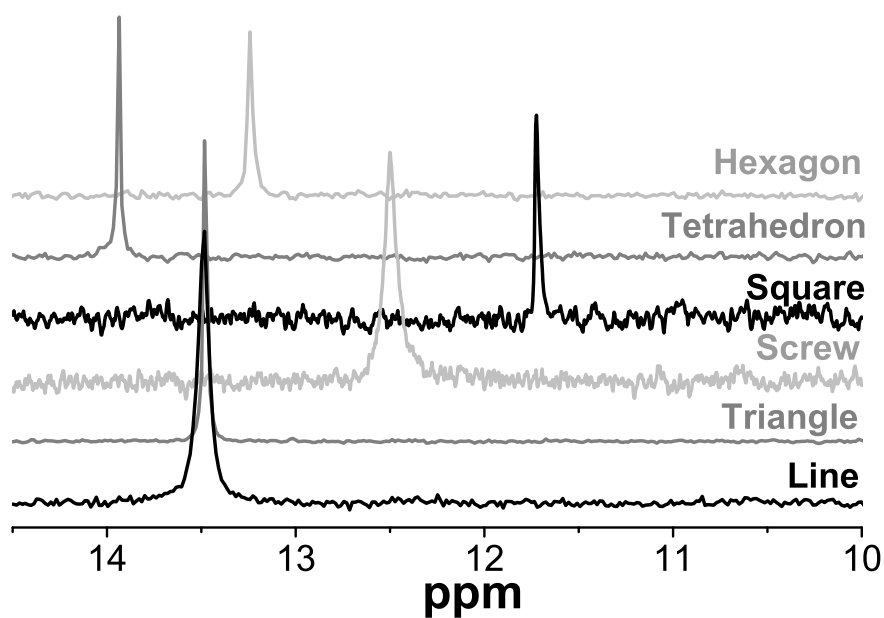


Figure 4.18: ^{31}P liquid-state NMR spectra recorded at 202.5 MHz (11.7 T) in DMSO at 100°C from bottom to top LINE, TRIANGLE, SCREW, SQUARE, TETRAHEDRON, and HEXAGON.

influence the electronic shielding of the ^{31}P nucleus since the chemical motif in all cases is $\text{Ph} - \text{PO}(\text{OH})_2$. Thus, the chemical shifts variations are possibly due to the chemical structure differences.

Comparing the liquid with the solid-state spectra one can immediately see, that in the LINE and the HEXAGON the chemical shift increases by $\simeq 10$ ppm, as illustrated in Figure 4.19a,b. The chemical shift values of the PA groups range from 21 ppm for the LINE and 18 ppm for the HEXAGON respectively. Additionally, the spectrum for the LINE shows in the solid-state, the formation of a phosphonic acid anhydride at 15 ppm 4.19a [LEE 07a]. In contrast to the spectrum of the LINE, the HEXAGON spectrum displays a peak shifted to lower field at ~ 23 ppm. Additionally, the HEXAGON shows the same amount of a different site minor compound in the ^{31}P as in the ^1H MAS NMR spectrum as discussed in subsection 4.3.2. This peak, as well as the spectra of the other geometrical shapes, will now be discussed.

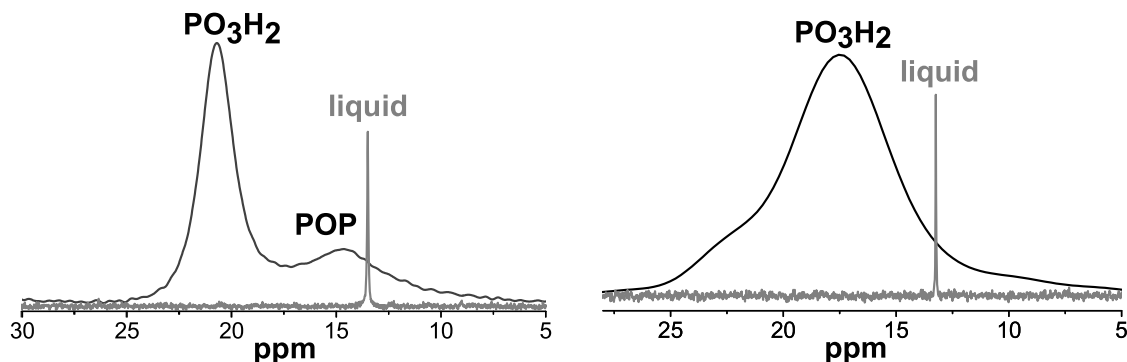


Figure 4.19: ^{31}P solid-state MAS NMR spectra at 20 kHz spinning (202.5 MHz, 11.7 T) - on the top, showing underneath liquid spectra in DMSO at 100°C (202.5 MHz, 16.4 T) of the a) LINE and the b) HEXAGON.

Similarly to the ^1H MAS NMR, the ^{31}P MAS NMR spectra show more differences than expected. All samples contain PA groups which are directly attached to phenyl rings. However, a variation of chemical shifts over 5 ppm are found. This indicates that PA of the investigated geometrical structures seem to orient in different macromolecular structures thus, located in different local fields of the aromatic systems and with the incorporated water. Therefore, a difference in the hydrogen bonds strength might be correlated with different orientations.

Comparing the spectra of the three samples in Figure 4.20, the HEXAGON, the TRIAN-

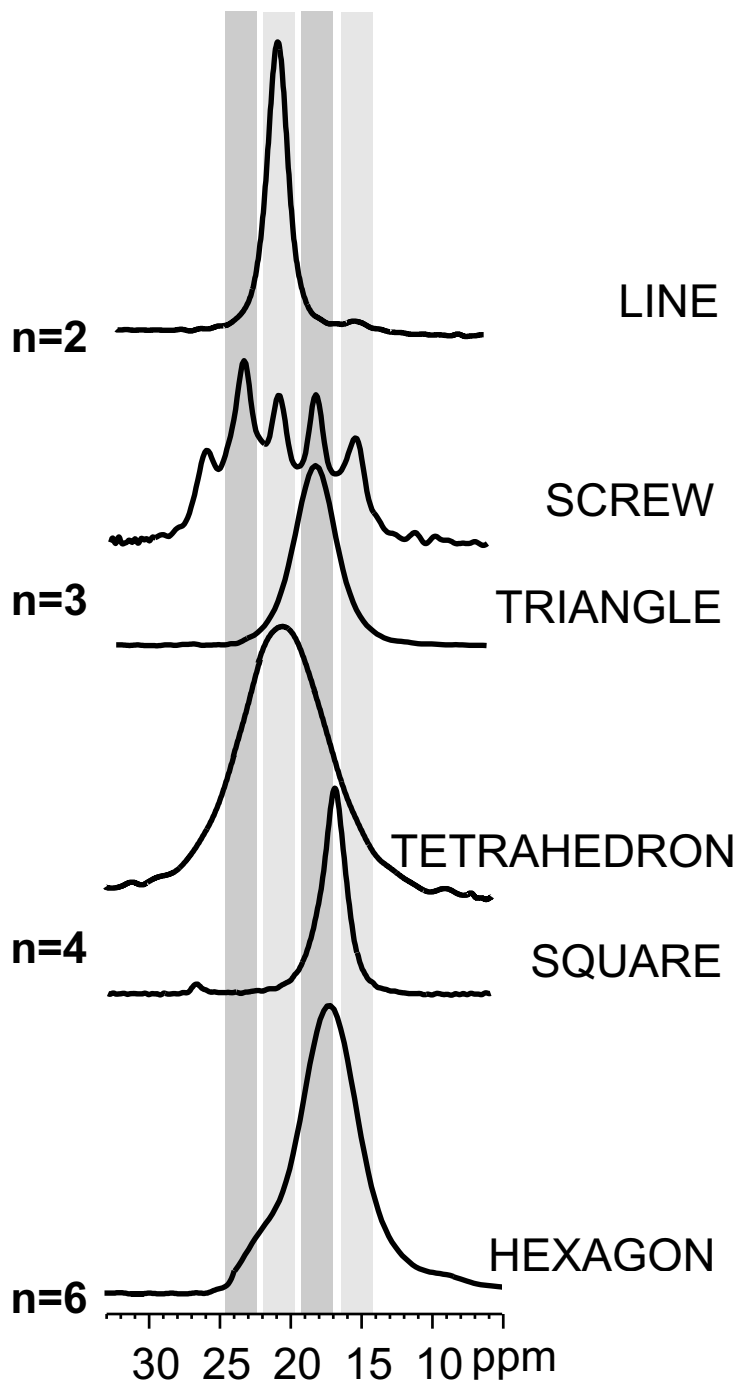


Figure 4.20: ^{31}P MAS NMR spectra of the ionomers at 20 kHz spinning (202.5 MHz, 16.4 T) at 30°C from the top with increasing number of phosphonic acids per molecule: $n=2$ LINE, $n=3$ SCREW, TRIANGLE, $n=4$ TETRAHEDRON, SQUARE $n=6$ HEXAGON.

GLE, and the SCREW, display a relative broad chemical shift distribution. Two samples, namely the LINE and the SQUARE, show quite narrow line widths of 460 Hz and 370 Hz, respectively. These line widths suggest that the samples are highly ordered such that the ^{31}P nuclei are located in a well defined environment. Notably, these geometrical shapes, the LINE and the SQUARE, both do not show significant bulk proton conductivity or a microscopic proton mobility, c.f. section 4.1 and subsection 4.3.2. Hence, this strongly suggests that a high degree of local ordering or crystallinity of the PA sites does not favor proton conduction in these systems.

The main peaks for the LINE and the SQUARE in the solid-state NMR spectra are located at 21 ppm and 17 ppm, as shown in Figure 4.20. In the case of the LINE, this observation is somehow contrary to the broad peak observed in the ^1H MAS NMR, as mentioned above. This might be explained by the larger homonuclear dipolar coupling which broadens the ^1H signal, while the higher ordered structure shows a narrow line in the hetero nuclei spectra. With respect to the results obtained in section 4.2 the PA of the LINE has a strong homonuclear dipolar coupling. In addition, both ^{31}P MAS NMR spectra of the LINE and SQUARE show some additional peaks. The small peak at 15 ppm in the LINE spectrum most probably corresponds to the anhydride (POP). This assumption is supported by various ^{31}P MAS NMR spectra of phosphonic acid and anhydride containing samples [LEE 07a, STEININGER 07]. Nevertheless, this group of chemical compounds provides a new possibility to assign this signal. The HEXAGON, as an example, shows, besides the major peak at 18 ppm a shoulder at 23 ppm which could be a structural impurity of 5%, which is the same amount found in the VT ^1H MAS NMR spectra in subsection 4.3.2. The assumption of different PA sites is supported by the ^{31}P MAS NMR spectra of the HEXAGON when stored under 100% RH. Here, the resolution increases due to higher mobility resulting in a splitting of the broad signal, see Figure 4.21. Additionally, it is observed, that the center of the phosphorous chemical shift under wet conditions is located at smaller ppm values. This, however, suggests that the phosphorous with higher chemical shift values represent the PAs which are not interacting with water.

The ionomers are small molecules and can arrange somehow in a more or less crystalline structure. If the surrounding is not completely identical for the ^{31}P nucleus it experiences

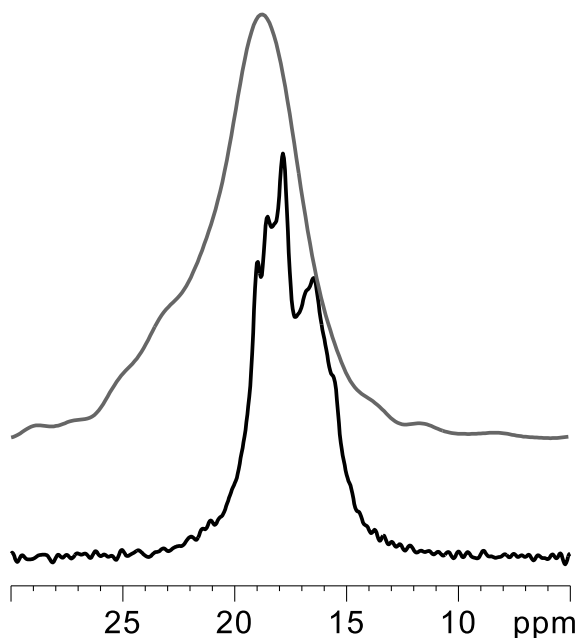


Figure 4.21: ^{31}P MAS NMR spectra recorded at 15 kHz spinning (202.5 MHz, 16.4T) of the HEXAGON as obtained from the synthesis and dried (dark grey) and after storing the sample under 100% RH (black).

different chemical shieldings, resulting in a broad NMR signal. A well-defined structure on the other hand with different sites gives rise to several narrow signals. This differentiation might explain the unusual ^{31}P MAS NMR spectrum observed for the SCREW, see Figure 4.20, where the structure appears more complicated but highly ordered. In fact, the spectrum shows a clear separation of at least six peaks instead of one broad peak which is found in the TETRAHEDRON. Furthermore, the chemical shift distribution is quite broad and ranges from 30 to 15 ppm (7500 Hz).

From the ^1H and ^2H NMR data as well as conductivity results described above it is clear that the systems can incorporate water in their structure. Therefore, it is of interest to determine the amount of water molecules and for this purpose the temperature behavior of the HEXAGON was analyzed in more detail. First step is to use thermogravimetric analysis (TGA) coupled with a mass spectrometer sensitive to the molecular mass of water (18 g/mol). The results from this measurement support once more incorporation of water in the sample, as shown in Figure 4.22a. It shows that at two temperature steps

the sample loses 4.5wt% water. To follow this by NMR, the sample was heated to 150°C and 350°C, packed into an NMR rotor inside of a glove box to avoid contact with atmospheric water. Subsequently, ^{31}P MAS NMR spectra were measured, c.f. Figure 4.22b.

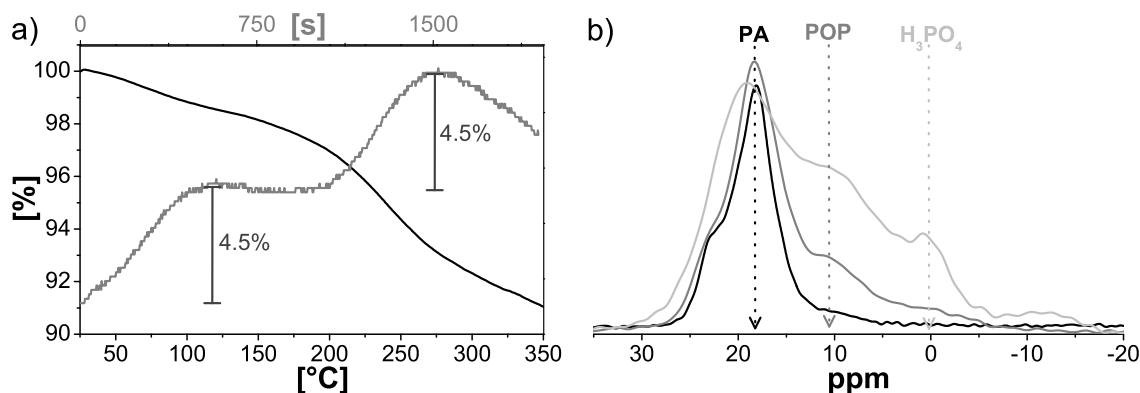


Figure 4.22: a) TGA curve 25 to 350°C at 10°C/min

b) ^{31}P MAS NMR spectra recorded at 15 kHz spinning (202.5 MHz, 16.4T) of the HEXAGON removed from TGA after heating to different temperatures: 25°C (black), 150°C (dark grey) and 350°C (light grey).

The ^{31}P MAS NMR is quantitative if a direct detection is used in the relaxation limit. Hence, peak deconvolution can yield the amount of free PA and POP present in the sample. These spectra show that due to the heating the well-known formation of anhydride (POP) is observed at 10 ppm. The samples heated to 150 and 350°C show an additional peak at 0 ppm of 4 and 9%, respectively. This resonance may be assigned either to free phosphoric acid or due to the formation of a trimer phosphonic acid [YOZA 94]. After exposure of the sample to air and humidity the ^{31}P spectrum still shows a peak at 0 ppm, however, but the signal at 10 ppm has disappeared [KALTBEITZEL 07]. This suggests that the anhydride formation is reversible and that the the signal at 0 ppm originates from free phosphoric acid, see Figure 4.22b. The shoulder at the left side of the room temperature spectrum will be discussed later in more detail. In the room temperature spectrum the amount of POP is already 6%. In the first heating step to 150°C the anhydride part increases to 24% and in the last step to 350°C the POP part increases to 44%. In both cases an POP increase of $\sim 19\%$ is detected. Both possible reactions, the anhydride formation and reaction to free phosphoric acid, are shown in Figure 4.23a and

b, respectively.

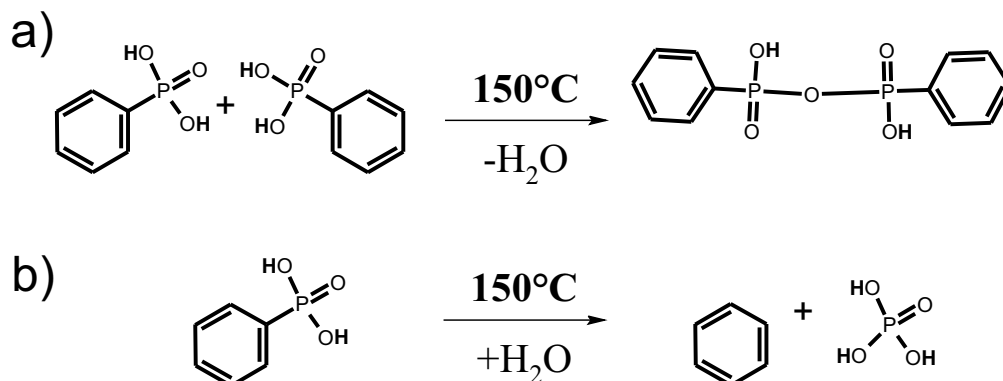


Figure 4.23: Anhydride and free phosphoric acid formation shown for PhPA.

Considering that the molar mass of the HEXAGON is 1014.03 g/mol which is equal to 100%, then 4.5% matches the loss of 2.5 water molecules per unit HEXAGON. If we would assume that all water molecules originate from the POP formation already in the first heating step, 84% of all free PA would be turned into POP. This, however, is not the case and integration of the peaks at 10 ppm shows a anhydride formation of $\sim 19\%$ for each heating step. This, however, makes it possible to calculate the amount of remaining water in the sample [MOLOGIN 02].

Calculations also predict that for membranes with a ratio $\text{H}_2\text{O} / \text{PO}_3\text{H}_2$ below 4, water is not available for proton transport as a vehicle [PEREIRA 06]. This calculation, however, is a variance after the observation that in PVPA, already one molecule of water is sufficient to increase the bulk proton conductivity by orders of magnitude [KALTBEITZEL 07]. In the case of the HEXAGON, the water amount where obtained from TGA measurements. If anhydride and phosphoric acid formation is considered, one gets 4.2 water molecules per HEXAGON which corresponds to 0.7 water molecules for each PA, which is comparable to amount of water found in PVPA. That relation would fulfill the constraint from Pereira et al. suggesting a GROTHUSS-type mechanism. On the other hand the ratio is roughly in the same range of water molecules needed for bulk proton conduction found for PVPA. In contrast to PVPA, the HEXAGON does not show conductivity behavior of bulk water in the polymer matrix. This combination of results

suggests a proton conduction in the HEXAGON based on the GROTHUSS mechanism strongly supported by the incorporated water which might also act like a vehicle on a short distance.

4.3.7 Dependency of ^{31}P CSA pattern on temperature and RH

Chemical shielding anisotropy (CSA) is an important interaction, which governs the ^{31}P NMR spectra of many phosphate materials [HARRIS 89]. Parameters related with the CSA provide details of the electronic environment and local mobility of molecules. Under slow MAS conditions, the CSA is extracted from the intensity distribution of spinning sidebands [HERZFELD 80]. Additionally, it can provide information not only on segmental orientations and reorientations [SCHMIDT-ROHR 94, HERZFELD 80] but also on the local structure [HU 01]. Furthermore, the continuing improvement of *ab-initio* chemical-shift calculations comprise a useful probe of molecular conformations [GAJDA 08]. In principle, if the spinning frequency ω_r is smaller than the chemical-shift anisotropy δ_σ , the two parameters δ_σ and η_σ are extracted from the chemical-shielding anisotropy [SCHMIDT-ROHR 94]. In some cases, correlation between the distance of two electronegative atoms aligned via a hydrogen bond and their chemical shift as well as chemical shift anisotropy were found [BERGLUNG 80].

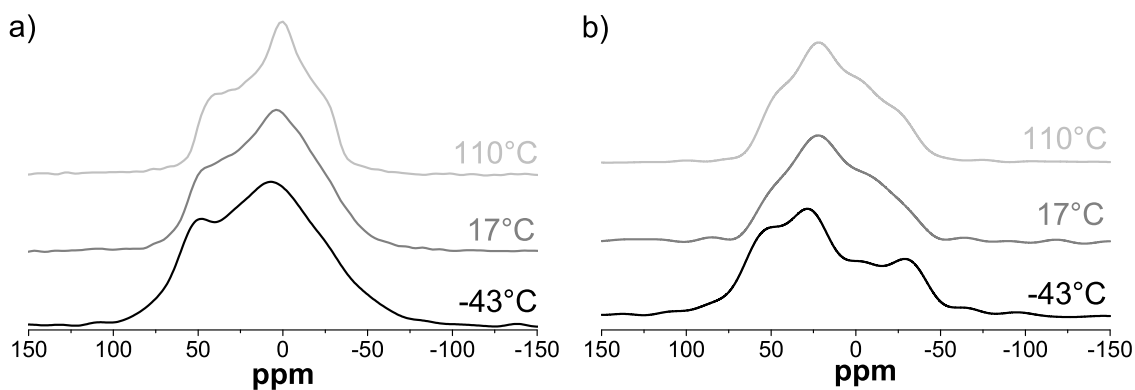


Figure 4.24: VT ^{31}P static NMR spectra (121.5 MHz, 7.0 T) recorded in dry conditions at different temperatures: -43°C (black), 17°C (dark grey), and 110°C (light grey) for a) the HEXAGON and b) the SQUARE.

Static ^{31}P MAS NMR spectra of different geometrical shapes were recorded at different

temperatures and RH, see Figure 4.24 and 4.25. The question was whether or not there is any effect on the static ^{31}P line shape of these external parameters. It is anticipated that due to higher mobility of the protons, the ^{31}P chemical anisotropy tensors may change. This in return would possibly be reflected by a different line width or a change of position for the maximum of the peak (δ_{22}) of the static ^{31}P spectrum [BERGLUNG 80]. From the HEXAGON it is known that within the given temperature range the ^1H chemical shift changes from 12 to 10 ppm, c.f. subsection 4.3.2, indicating a change in mobility of the acidic protons. However, VT ^{31}P NMR spectra of HEXAGON and SQUARE do not show any difference in the line shape or in δ_{22} . Unlike in PVPA, there is no change in tensor values at higher temperature, implicating a constant dynamics of the ^{31}P unaffected by the ^1H . Comparing the HEXAGON and the SQUARE only difference in the δ_{22} are found. Since δ_{22} depends on the asymmetry η_σ which describes the chemical surroundings this suggests that the PAs are orientated differently in the two geometrical shapes.

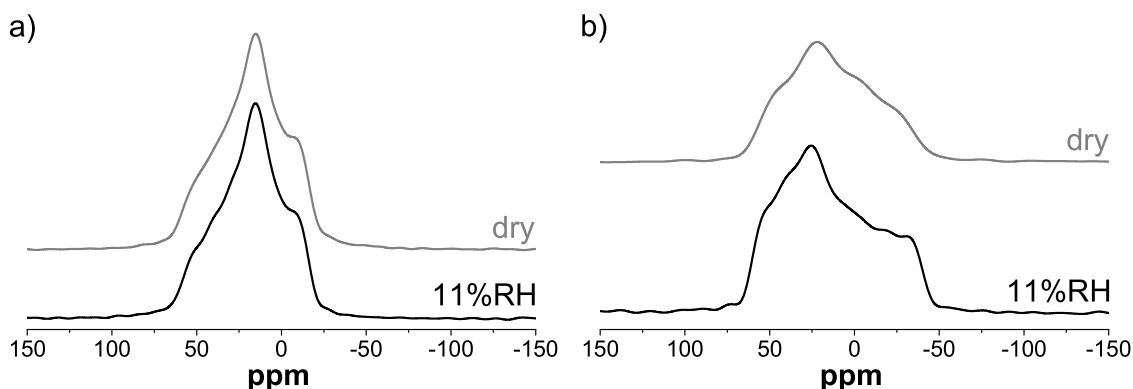


Figure 4.25: ^{31}P static NMR spectra (121.5 MHz, 7.0 T) recorded at 17°C in dry conditions (dark grey) and stored under a relative humidity of 11% (black). a) LINE b) SQUARE

From bulk proton conductivity data, in section 4.1, it is known that the values strongly depend on the relative humidity (RH). Additionally, it is expected that the water interacts with the phosphonic acid. However, in Figure 4.25, no changes of the line shape for the SQUARE or the LINE are observed, except for a slightly enhanced resolution. This means either that the ^{31}P tensors are not affected by the increase of water content and the formation of the hydrogen bond network of the surrounding or the shielding tensor is steadily changing, while the protons move towards another phosphonic group. Therefore, the spectrum could display an "averaged" shielding tensor due to the fast motion.

4.4 Structural features of the ionomers

4.4.1 Structure determination using WAXS and computations

Wide-angle X-ray scattering using 2D detection (2D-WAXS) is a versatile tool to study long-range organization of supramolecular systems [PISULA 05]. Filament extrusion WAXS introduces orientation in the sample similar to π - π packing of aromatic moieties [BROWN01]. Due to the poor solubility with decreasing PA amount per molecule, filament extrusion X-ray analysis could only be obtained from the HEXAGON.

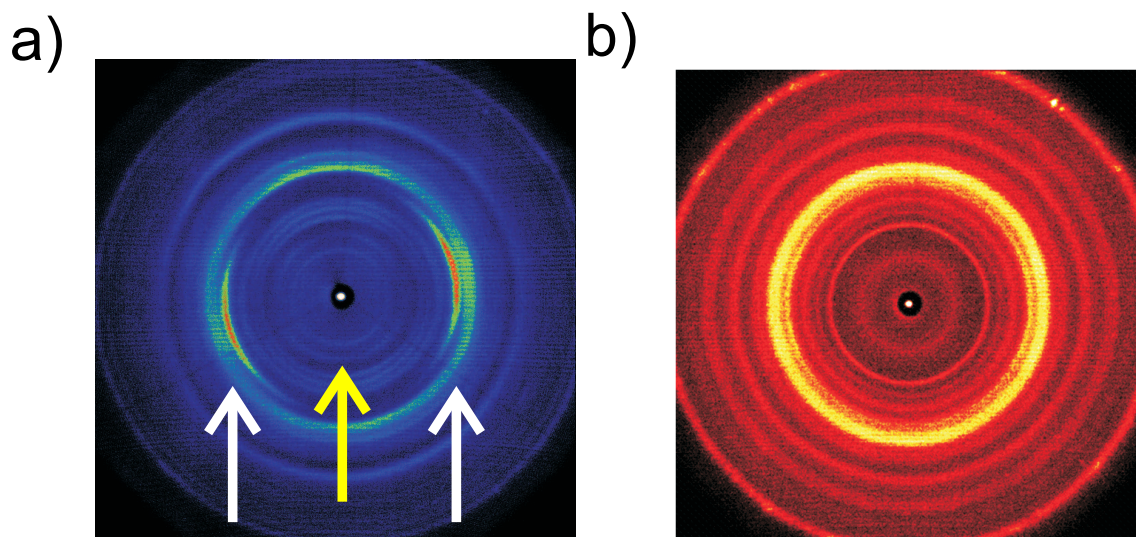


Figure 4.26: a) 2D WAXS data from filament extrusion of the HEXAGON arrows indicating the reflection 1.4 nm (yellow) and 0.6 nm (white) [JIMENEZ 09]. b) 2D WAXS powder pattern data from the HEXAGON.

The filament extrusion 2D WAXS data from the HEXAGON, shown in Figure 4.26a, indicate two different distances. Furthermore, the structure of the reflection indicated with the white arrows suggests a columnar packing. The larger 1.4 nm distance is located between the two columns and 0.6 nm represents the distance between the phosphonic acids [JIMENEZ 09]. The powder pattern of the HEXAGON is shown in Figure 4.26b and shows compared to the SCREW and SQUARE less crystalline reflections, c.f. Figure 4.27a and b. Notably, this again supports the assumption from the ^{31}P MAS NMR spectra, of the HEXAGON and the SQUARE, discussed in section 4.3.6, that crystallinity does not

favor high bulk proton conduction.

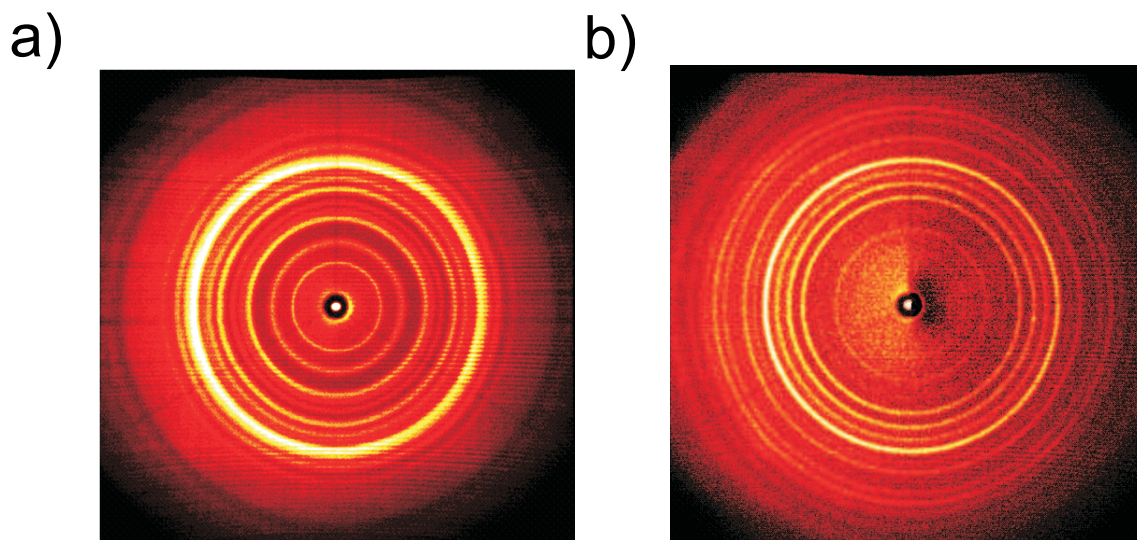


Figure 4.27: 2D WAXS powder pattern from the a) SCREW and b) SQUARE.

Furthermore, 2D WAXS diffractograms can reveal information about the crystallinity of the sample as mentioned above. Under the assumption of crystallinity a plot of the intensity against the angle dependency (2Θ) displays good resolved spectra. In the presence of amorphous or glassy parts the pattern shows underneath the sharp signals a broad peak, the so-called halo. By integration of the sharp and the broad signals the relative amount of the amorphous part in the sample can be calculated. All three X-ray data plotted here the HEXAGON, the SQUARE, and the SCREW show rather sharp reflection, as seen in Figure 4.26 and 4.27. Since the halo part is rather small the sample is considered as relative crystalline.

The results from extrusion X-ray can also be supported by data obtained from single crystal X-ray diffraction. A single crystal from a system related to HEXAGON could be grown from a sodium ethanolate-methanolate mixture, where the structure included sodium ethanolate and methanolate. The X-ray powder pattern, shown in Figure 4.28, obtained from the pure HEXAGON exhibits rather broad lines. In fact, it is difficult to imagine that the salt and the HEXAGON have similar structures. The signal at 6.5Θ corresponds to 1.4 nm the intercolumnar distances and is the only signal which is present in the bulk and the salt structure, c.f. Figure 4.28. To compare the salt structure from

X-ray with WAXS data of the same structure as measured in NMR, computations were used to construct possible models, as described in the Appendix B.

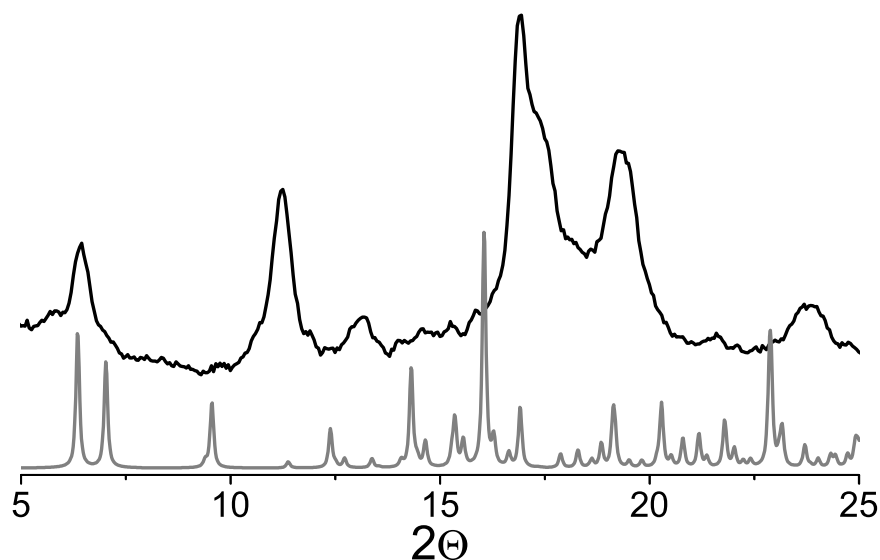


Figure 4.28: Comparison of the X-ray data for the HEXAGON obtained from single crystal grown from methanol-ethanol mixture (dark grey) with the WAXS data from the synthesized sample (black).

The assumption of incorporated water is supported by CPMD calculations where methanolates and ethanlates are replaced by water molecules. The water is always located between the PA. Even when starting the calculation with the water position between two aromatic rings it relaxes towards the PA resulting in a stable structure, where PA form with water molecules (green circles) a 2D zigzag pathway through the sample, see Figure 4.29a and b. These pathways are isolated in the different layers. By adding one water molecule per PA unit the water connects the zigzag pathways between the different layers. The amount of water was taken from the results of the combined ^{31}P MAS NMR and TGA-MS in section 4.3.6. The hexamere's principal scaffold structure, with carboxylic instead of PA, was already revealed [WATSON 01]. Consequently, it is of interest to compare these two structures to analyze the effect of the number of hydrogen bonds. The carboxylic acid derivative shows formation of almost

all hydrogen bonds in the molecular plane. In addition, some form hydrogen bonds between adjacent sheets in a way that columnar supramolecular networks are formed [MALY 07]. The crystal structure of the TETRAHEDRON is known from literature [JONES

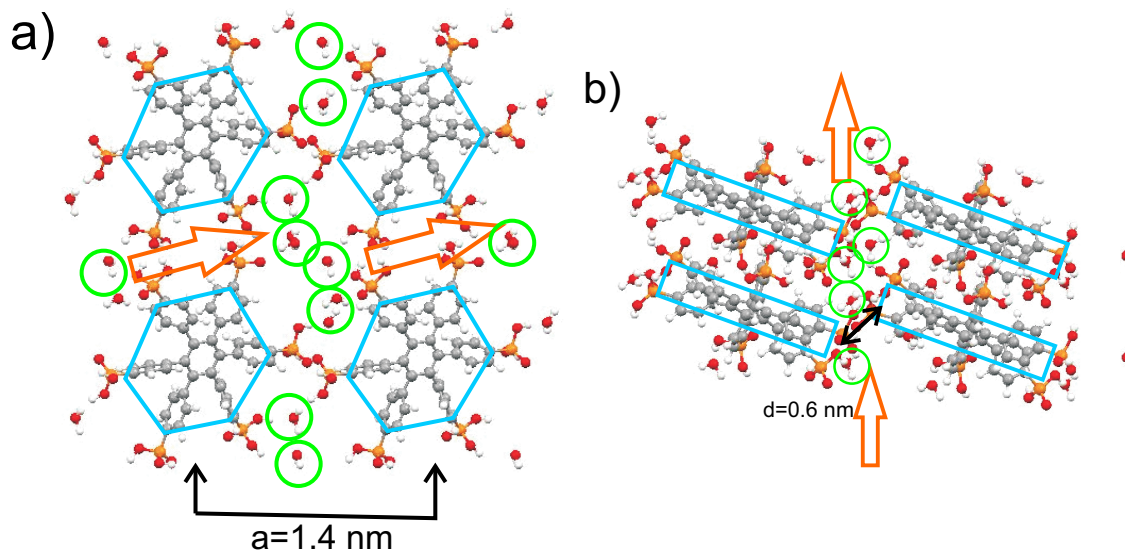


Figure 4.29: Possible crystal structure of the HEXAGON obtained from calculation from a) top view of the columns with an distance for two columnar center of $a = 1.4 \text{ nm}$ and b) side view revealing the intercolumnar phosphorous phosphorous distance of $d = 0.6 \text{ nm}$. Green circles show the water molecules attached to the structure and orange arrows indicate a possible pathway for the protons through the structure.

06]. It forms tetrameric clusters isolated from each other. Combining these results one might conclude that the formation of a PA pathway supports and the formation of isolated clusters prevents proton conduction in the crystal.

A further parameter which affects the bulk proton conduction, beside the assembly of the aromatic moiety, are the functional groups. The effect is observed, e.g. when substituting the PA in the HEXAGON by carboxylic acid groups (CA). The molecular structure of the CA-HEXAGON which is easy to crystallize is known from literature and reflects similar distances as observed in the PA-HEXAGON system [KOBAYASHI 00]. The intercolumnar distance is given by 1.34 nm and the CA groups are separated by 0.6 nm . The CA-HEXAGON possesses a center of symmetry, while the aromatic side rings are nearly orthogonal with respect to the core. The dihedral angle is not the same for all of them but changes from 91.7 to 83.5° . These structural information suggest a similar

packing of the aromatic moiety in the CA and PA-HEXAGON. Unlike the CA, the PA does not form stable and defined hydrogen bonded dimers but built a hydrogen bonded network with different PAs. Thus, the resulting mobility of the protons, delocalized over several PA, might be mainly the reason that systems containing PA as functional groups shows, in general, a higher proton conductivity than the CA substitutes, e.g. comparing PVPA with poly(acrylic acid) (PAA) [AKBEY 08]. Overall, these results strongly suggest that higher crystallinity of the functional group does not support bulk proton conductivity.

4.4.2 Temperature dependency of the SQUARE and the SCREW

Compared to the other ionomers the SQUARE shows a quite different thermal behavior. Therefore, the SQUARE, freshly obtained from synthesis, was characterized by VT ^1H , $^{13}\text{C}\{^1\text{H}\}$ CP, and ^{31}P MAS NMR. A defined temperature profile has been used to follow the molecular changes which occur during heating the sample. This has been a three steps profile and applied as followed, first increasing the temperature by 10°C steps, second waiting 15 minutes until the thermal equilibrium has been reached and finally measuring the ^1H MAS NMR. The first change in the ^1H MAS NMR spectrum, apart from line narrowing, is observed by reaching 90°C , see Figure 4.30a. At this temperature,

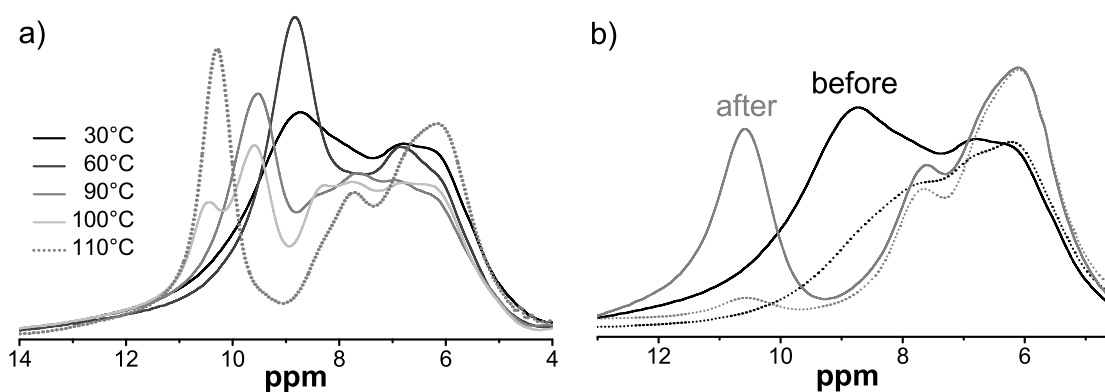


Figure 4.30: a) ^1H MAS NMR at 29762 Hz spinning (700.1MHz, 16.4T) of the SQUARE at different temperatures
 b) Comparison of ^1H and DQF MAS spectra at 29762 Hz spinning (700.1MHz, 16.4T) of the SQUARE before and after heating.

the peak corresponding to the PA hydrogen bond starts to move gradually from 8.8 to 9.5 ppm. This change is not time but temperature dependent and was followed by changing the temperature in 5°C steps. Time dependency could be disproved since a repeated experiments at constant temperature after an hour did not show any difference. However, before the change from 8.8 to 9.5 ppm is completed a second step is observed at 110°C .

Here, the value corresponding to the PA hydrogen bond shifts to even higher values at 10.5 ppm, see Figure 4.30a. Checking again the time dependency reveals that this change is continuous at constant temperature. The change needs about an hour to be completed, as shown in Figure 4.31a. Based on this observation a closer look at the unheated

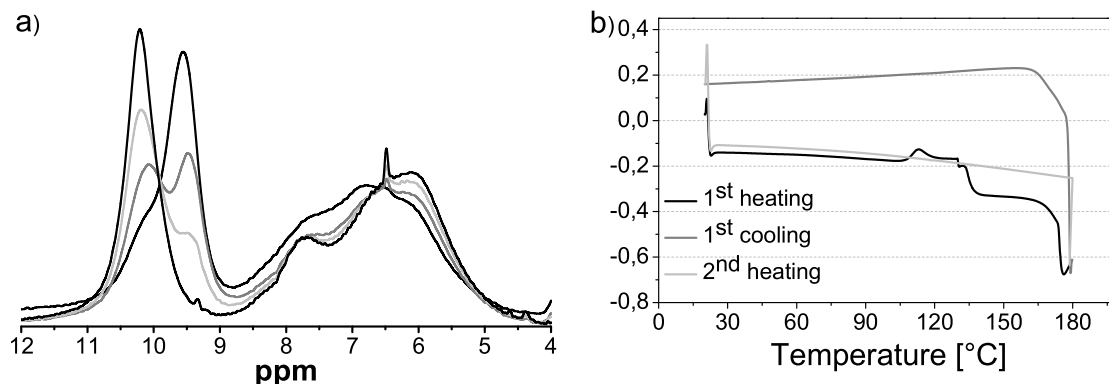


Figure 4.31: a) ^1H MAS NMR spectra of the SQUARE at 30 kHz spinning (700.1 MHz, 16.4T) at 110°C

Starting at $t=0$ minutes (black) to $t=60$ min (light grey) with 20 minutes between each measurement.

b) DSC measurement for SQUARE first heating (black), second heating (light grey).

^1H MAS NMR spectrum already shows the presence of a high temperature peak in the crude sample, in Figure 4.31b. Accordingly, the high temperature structure is already present to some extent. Due to heating a structural change from the metastable structure into a more energetically beneficial arrangement completes. Afterwards, this process is not reversible and the formed structure is stable. The DSC measurement supports this observation, since a change at 110°C in the curve only are observed during the first heating, as illustrated in Figure 4.31b. The TGA graph shows that the SQUARE loses over the observed temperature range up to 110°C 2wt%, see Appendix Figure A.3a. This is an indication, that the observed change might be due to water loss and an followed by reorientation of the structure. In addition, the peak at 10.5 ppm shows no change in line width at the different measured temperatures.

Since a certain narrowing in the line width could be observed in the first heating, this suggests that the initial structure has mobile protons and due to, e.g. strengthening of the hydrogen bonds, they disappears. This result is also supported by the dry and humid bulk conductivity data, since after the first heating the absolute conductivity value lowers by several orders of magnitude, see Appendix Figure A.4.

The described change in the WAXS data shows a loss in signals at small 2Θ val-

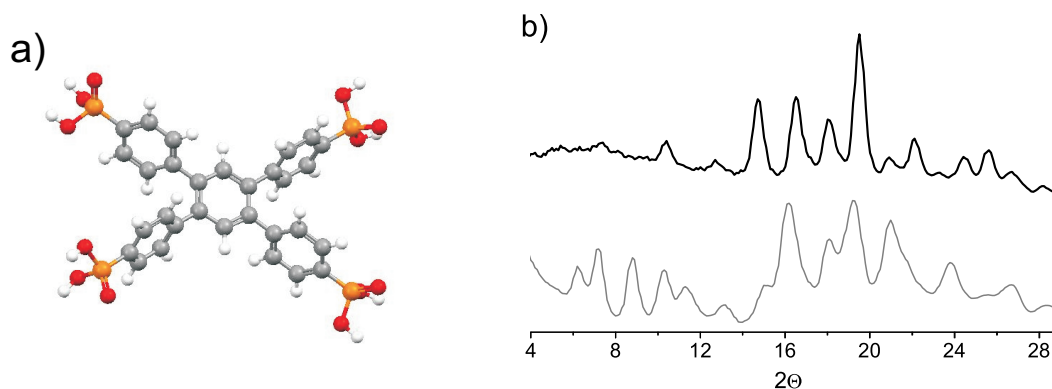


Figure 4.32: a) Structure of the SQUARE in the gas phase obtained from ChemDraw 3D molecular-mechanics force field calculations (MMFF94) [HALGREN 96] energy minimization.
 b) WAXS powder spectra plotted against 2Θ before (dark grey) and after annealing (black).

ues in the range from $4\text{-}14^\circ$ due to the heating, as shown in Figure 4.32b. This corresponds to a loss in long range order. The reflections at 2Θ ranging from 14° to 22° , represent shorter distances and do not change their position both gain in intensity and resolution. This supports the assumption of non organized long-range arrangement where a similar short-range order is present, as has been reported for the HBCs [BROWN 01]. The change in the SQUARE can also be observed in the VT $^{13}\text{C}\{^1\text{H}\}$ CP and ^{31}P MAS NMR spectra, see Figure 4.34a and b, before and after annealing. Both show a drastic change in their spectral resolution. The ^{13}C MAS NMR spectrum shows a massive narrowing of all signals from a line width of 200 to 50 Hz. The latter line width is comparable to the line width of adamantane which is a highly crystalline compound [MORKOMBE03]. Additionally, the three quaternary aromatic carbon signals are shifted by about 3 ppm, compare black and grey spectrum in Figure 4.34a. The resonance at 136 ppm (after heating) can be assigned, due to the lowest $^{13}\text{C}\{^1\text{H}\}$ CP intensity, to the quaternary carbon in the central benzene ring. This central ^{13}C and the one which is found at 137 ppm (after heating) are affected due to the new packing and shifted to lower ppm values. This could indicate that the SQUARE molecules now are stacking, implicating that both ^{13}C with a similar shift are located in similar areas of the ring current. The third quaternary ^{13}C results after the heating in a lower field at 146 ppm. Hence, the differing quaternary ^{13}C is most probably located at the outer aromatic ring

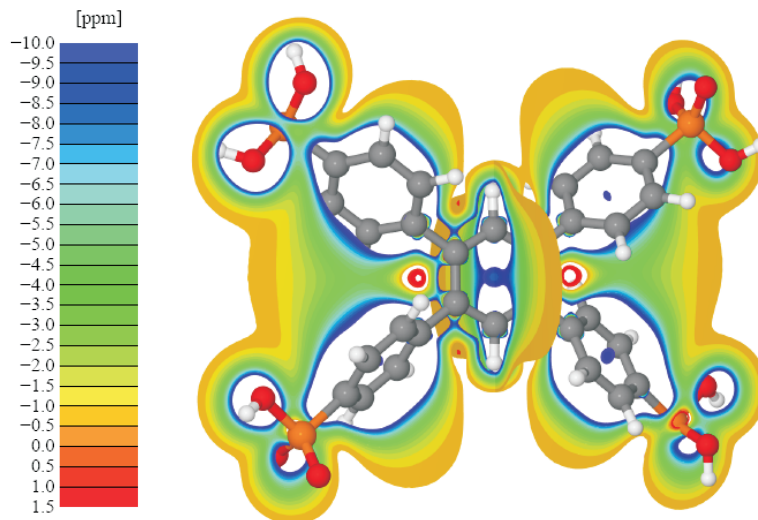


Figure 4.33: NICS map of the SQUARE computed using CPMD described in the Appendix B.

connected to the PA. Figure 4.32a shows the 3D structure of the SQUARE obtained from ChemDraw 3D molecular mechanics force field (MMFF94) energy minimization. Based on that preoptimization a nucleus independent chemical shift (NICS) map has been calculated, see Figure 4.33. Here, in the green region an atom would experience a shift of -3 ppm, while the dark orange part would shift it by +0.5 ppm. Based on these results further work may be done, to predict a possible crystal structure.

The ^{31}P MAS NMR spectrum of the SQUARE shows before annealing the existence of five different sites comparable to the ^{31}P MAS NMR spectrum of the SCREW, compare Figure 4.34b and d. After annealing the SCREW the number of sites is reduced, most likely due to higher order, to two resonances with 85 and 15% relative intensities. The phosphorous nucleus which represents the main peak is now located at a chemical shift which was not present before. This is an additional indication for an elementary structural change or/and might be attributed to the loss of water induced by annealing, as discussed in subsection 4.3.4.

Compared to the SQUARE, the SCREW has a more complex structure. The structures obtained from ChemDraw 3D MMFF94 energy minimization strongly depend on the original geometrical shape. Nevertheless, the structure that was obtained in the majority

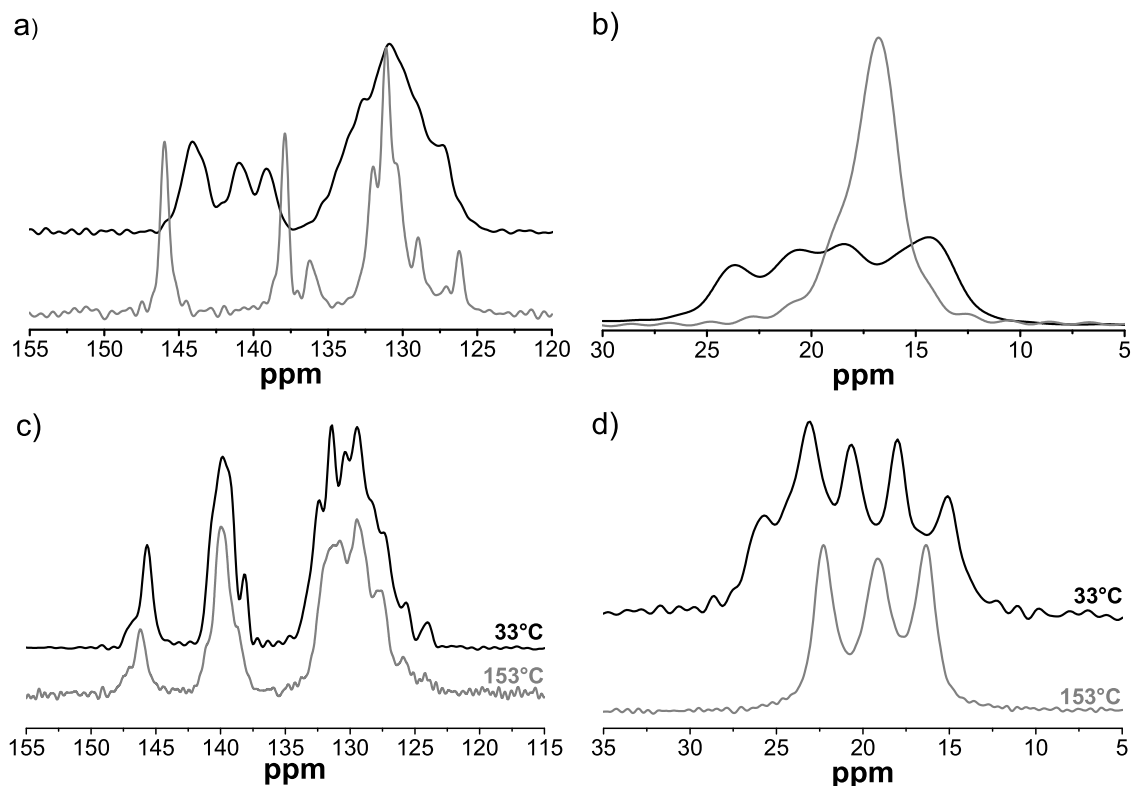


Figure 4.34: a) $^{13}\text{C}\{^1\text{H}\}$ CP MAS NMR spectra of the SQUARE at 20 kHz spinning (125.8 MHz, 11.7 T) before (black) and after (dark grey) annealing at 110°C
 b) ^{31}P MAS NMR spectra of the SQUARE at 20 kHz spinning (202.5 MHz, 11.7 T) before (black) and after (dark grey) annealing at 110°C
 c) $^{13}\text{C}\{^1\text{H}\}$ CP MAS NMR spectra of the SCREW at 10 kHz spinning and (125.8 MHz, 11.7 T) at 33°C (black) and at 153°C (dark grey)
 d) ^{31}P MAS NMR spectra of the SCREW at 10 kHz spinning (202.5 MHz, 11.7 T) at 33°C (black) and at 153°C (dark grey)

of runs is shown in Figure 4.35. Before heating, the ^{31}P MAS NMR spectrum of the SCREW shows a broad signal where at least six different sites are identified. This observation is yet not fully understood but might indicate that the asymmetric unit contains more than one or even two molecules. At higher temperature a new orientation of the PA groups occur changing the ^{31}P MAS NMR spectrum to three signals with the intensity ratio of 1:1:1. Due to the chemical structure these three peaks might be expected if there is no symmetry center in the molecule, as illustrated in Figure 4.35. On the other hand the $^{13}\text{C}\{^1\text{H}\}$ CP MAS NMR spectrum shows a less dramatic change as

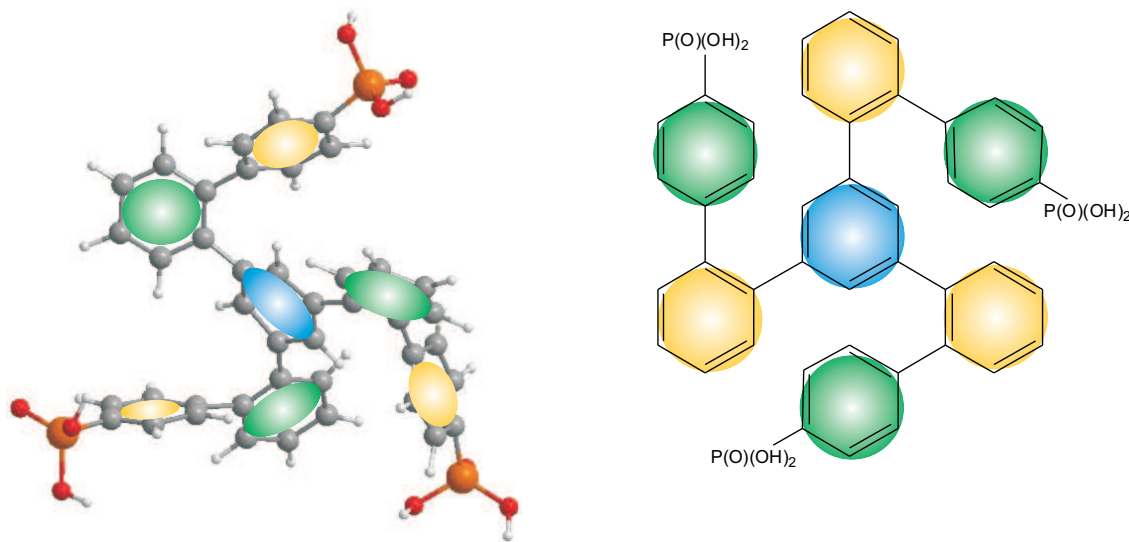


Figure 4.35: Structure of the SCREW in the gas phase obtained from ChemDraw 3D MMFF94 energy minimization

observed in the SQUARE, c.f. Figure 4.34a and c. Combining these two observations of the ^{31}P and the $^{13}\text{C}\{^1\text{H}\}$ CP MAS NMR, one might suggest, that at higher temperature the PA equalize while the aromatic packing does not change drastically.

It has been discussed in section 4.1, that the bulk proton conductivity data under humid conditions, of the SCREW, show a reversible change in the temperature dependency. For this purpose, the high temperature behavior of the SCREW was analyzed in more detail. VT $^{13}\text{C}\{^1\text{H}\}$ CP and ^{31}P MAS NMR experiments were conducted in the temperature range from 100 to 160°C. The ^{31}P MAS NMR spectra display a change from the broad overlapping line shape from different sites, reducing to the three more defined sites. On the contrary, the VT $^{13}\text{C}\{^1\text{H}\}$ CP MAS stack shows that there is no change observed within the same temperature range. These results are indicative of a structural change for PA and may be attributed to a new orientation of the PA hydrogen bond structure, while the global stacking seems not to be affected. This is supported by the TGA measurement, see Appendix Figure A.3b, where no loss of weight is observed. Accordingly, a structural change, as observed in the SQUARE is excluded. Furthermore, the change in the SQUARE is non reversible whereas the SCREW after one week at room temperature shows the same ^{31}P MAS NMR spectrum as before. This supports the assumption of a new arrangement at higher temperature induced mainly at the ^1H and

^{31}P of the PA groups.

4.4.3 ^{31}P MAS NMR spectra of the SCREW

From the one-pulse ^{31}P MAS NMR spectrum of the SCREW it is evident that six different ^{31}P PA sites are present. Thus, recording static ^{31}P spectra does not make sense since six CSA patterns would severely overlap. Consequently, another method has been applied to obtain structural information about the distinct sites. In the literature a 2D method, termed separation of undistorted powder patterns by effortless recoupling (SUPER) was used for ^{13}C CSA analysis [ORR 05]. This method developed by the group of Schmidt-Rohr, was mainly used for 4 mm rotors applying, spinning speeds, between 2.5 and 5 kHz, and based on the work from Tycko et al. [TYCKO 89]. In this work rotors with a size of 2.5 mm rotating at 6050 Hz were used. The different experimental parameters for the SUPER experiment have to be adjusted carefully, since the standard radio frequency power levels, in particular for protons, should not have a decoupling field strength $\frac{\gamma B_1}{2\pi}$ higher than 120 kHz. Two important parameters for the SUPER experiment are the CSA scaling factor which was chosen as 0.155 and the spectral width of the indirect dimension. Both directly effect the radio frequency power levels and the rotation frequency [LIU 02].

The SUPER experiment is often used to assign groups with similar chemical shifts by comparing the two parameters δ_σ and η_σ . In this work the SUPER experiment was applied to phosphorous, which is not that common [IRONSIDE 07]. Since the ^{31}P in the sample all have an identical chemical structure (PA), differences in δ_σ and η_σ are expected to originate from differences in the local structure. The spectra in Figure 4.36 do not show a clear CSA powder pattern which indicates that the PAs most likely are in the intermediate motional regime. Thus, the analysis of this data, as observed earlier in the static spectra of the HEXAGON and SCREW, is not straight forward. Without going into detail the extracted slides show a difference in line width, η and δ_{22} . Even though differences can hardly be quantified the extracted spectra show variation in the line shapes which may indicate different surroundings for the PAs.

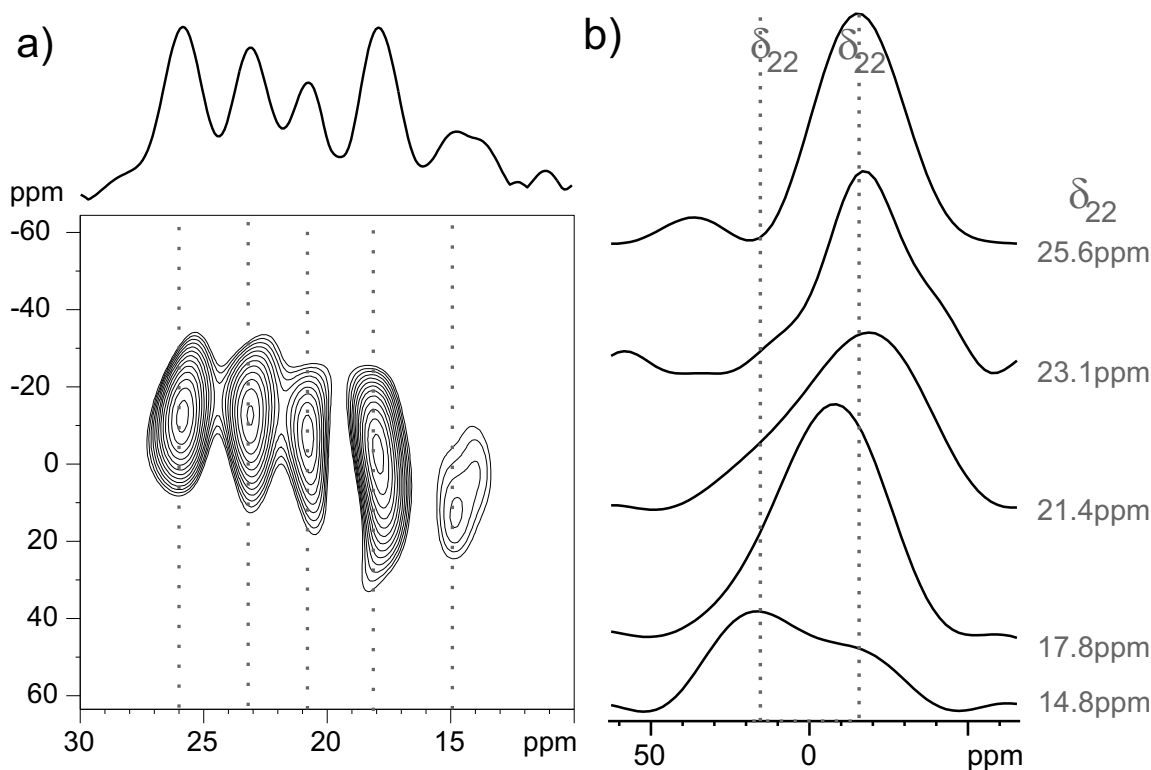


Figure 4.36: ^{31}P MAS NMR SUPER experiment recorded at 6050 Hz spinning (121.5 MHz, 7.0 T) of the SCREW a) 2D spectra with the ^{31}P MAS NMR experiment plotted on the top. Lines indicating the position where CSA sections were taken and shown in b).

To obtain more structural information about the proximity of the different sites further 2D experiments were conducted. The first approach has been to record a ^{31}P - ^{31}P SQ-DQ BaBa correlation spectrum [FEIKE 96]. Since the intensity of a DQ correlated signal is a function of the inverse internuclear distance, gyromagnetic ratio and recoupling time, it is possible to extract quantitative information about internuclear cubed distances. Similarly to ^1H NMR it was used to obtain information about the proximity of two phosphorous in the structure [LEE 07a]. Due to the gyromagnetic ratio of phosphorus $\gamma = 1.081 \cdot 10^8 \frac{\text{rad}}{\text{sT}}$, relatively low compared to the hydrogen, the dipolar coupling is weaker and measured distances are generally smaller than commonly measured in ^1H MAS NMR. The relationship between the internuclear distance is given in equation 4.3.

$$D^{(ii)} = \frac{-\mu_0 \hbar \gamma_i^2}{4\pi r_{ii}^3} \quad (4.3)$$

Compared to the gyromagnetic ratio for ^1H $\gamma = 2.675 \cdot 10^8 \frac{\text{rad}}{\text{sT}}$, it is less than one half. Therefore, to detect the similar distances $r_{31\text{P}31\text{P}}$ as in protons the recoupling has to be approximately 2.5 times longer. Recoupling times have to be chosen according to the following equation $\frac{D^{1\text{H}1\text{H}}}{D^{31\text{P}31\text{P}}} = \frac{\gamma_{1\text{H}}^2}{\gamma_{31\text{P}}^2}$. Notably, no signal from auto correlation or cross peaks could be obtained, even using a recoupling time of up to 16 times the rotor period, which was successful in PVPA [LEE 07a]. This is an indication that in the HEXAGON the distance between the ^{31}P of the PAs are bigger than 0.53 nm.

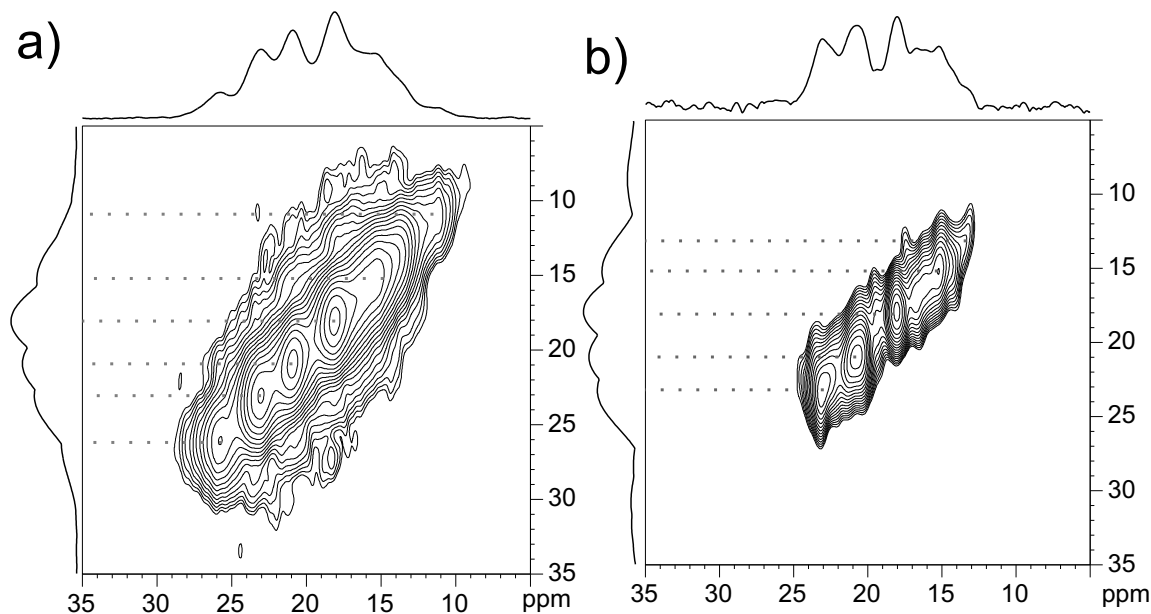


Figure 4.37: ^{31}P MAS NMR RFDR spectra recorded at 25 kHz spinning (202.5 MHz, 11.7 T) of the SCREW with ^{31}P NMR projections plotted on the top. Different mixing times of a) 3.4 ms and b) 12.8 ms have been employed.

As a second approach, a radio frequency driven dipolar recoupling RFDR spectrum was measured [BENNETT 92]. The result of this is an effective time-independent interaction that generates magnetization transfer and leads to cross peaks between coupled resonances in a 2D spectrum. The difference, compared to the BaBa experiment is that RFDR cannot distinguish direct magnetization transfer from magnetization transfer via three or more spins, the sequence detect SQ-SQ correlations [SCHMIDT-ROHR 94]. The RFDR spectra were recorded at increasing mixing times, starting with 3.2, 6.4, and 12.8 ms. Due to the absence of cross peaks one may claim that PAs of the different sites are

not in close proximity to on another.

4.4.4 Solid state effect on ^1H MAS NMR spectra

So far, the NMR study focussed on the hydrogen bonded network of PA and H_2O . In this subsequent section, structure, packing and possible dynamics of the aromatic groups of the systems are studied by ^1H and ^{13}C MAS NMR. In this subsection the ^1H MAS NMR spectrum for the LINE is discussed using additional ^1H MAS NMR spectra for further comparison. In general, information with respect to assignments are obtained by comparison of liquid-state with solid-state NMR spectra.

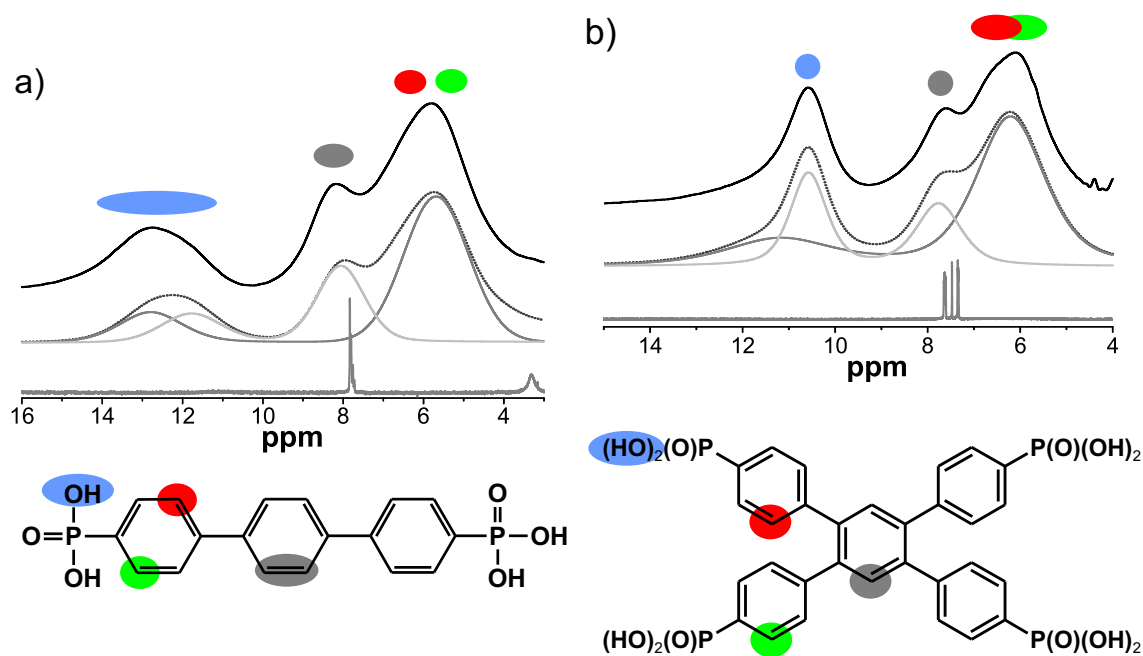


Figure 4.38: ^1H solid-state MAS NMR spectra recorded at 30 kHz spinning (700.1 MHz, 16.4 T) is shown on the top, below the deconvoluted peaks are plotted and at the bottom the liquid spectra in DMSO at 100°C (500.2 MHz, 11.7 T) is shown for a) LINE and b) SQUARE.

In addition, ^1H MAS NMR is quantitative, provided that a sufficient long relaxation delay has been chosen, which facilitates the assignment. In the spectrum for the LINE, some ^1H signals are shifted when going from liquid to solid state, see Figure 4.38a. In the liquid-state taken spectrum all ^1H are located at 7.8 ppm, while the solid-state spectrum includes three peaks. Two of these signals are found in the region between 4 and 10 ppm corresponding to the aromatic protons. Due to their broad lines and similar chemical shifts the overall spectrum suffers from a server overlap. The third peak which

corresponds to the PA proton is located at 12 ppm. A closer look on this signal indicates that the peak is not symmetric. Deconvolution of the ^1H MAS NMR spectrum reveals two peaks with the proton ratio of 2 : 2. They represent hydrogen bonds incorporated in different structural positions and with different strengths. By iterative fitting, the aromatic signals are deconvoluted and analyzed quantitatively, as shown below the ^1H MAS NMR spectrum in Figure 4.38a. The integrals of the different peaks reveal the ratio 4 : 8 of the aromatic CH protons, indicating that the chemical shift of one kind of protons stays unaffected by the packing, while the other type of protons shows a shift of the chemical shift towards higher field.

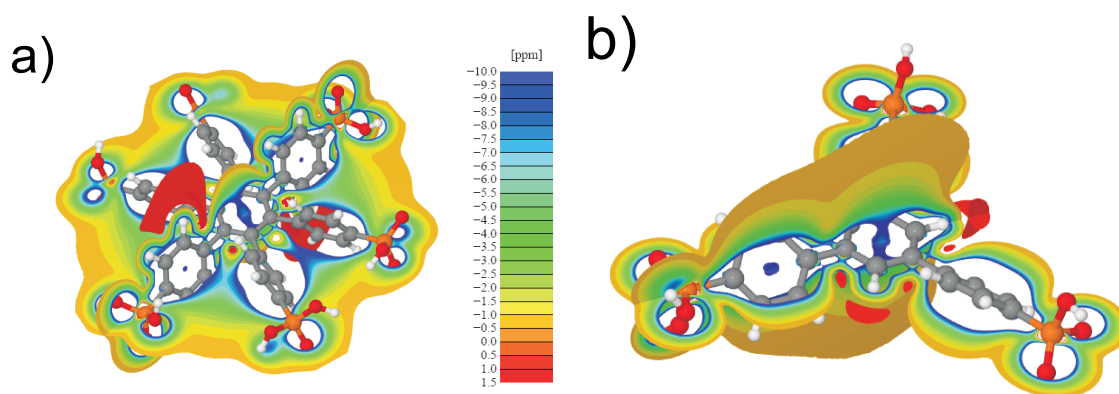


Figure 4.39: NICS maps of a) the HEXAGON and b) the TRIANGLE have been computed as mentioned in the Appendix section B.

Often deconvolution of broad signals cannot provide clear results, which is also illustrated here in the ^1H MAS NMR spectra of the LINE and the SQUARE shown in Figure 4.38a and b, respectively. In this case the peak at 6 ppm results from two different aromatic sites, where the overlap is too strong so one should take care considering deconvolution. In the solid state, the protons are exposed to the ring currents due to other nearby through-space intra- or intermolecular aromatic moieties [WAUGH 56]. Depending on the packing and the geometrical structure the ^1H are influenced differently. For example in the case of the HEXAGON due to the high density of aromatic rings within one plane the next molecule would have to be placed on top of another in a distance defined by repulsion. The minimum distance is limited by the repulsion of the twisted rings. By avoiding the direct contact the whole molecule is either rotated by or slit to one axis. Other molecules, such as the TRIANGLE, can approach one another much closer,

since after rotation there is no hindrance for the tilted aromatic rings and additionally there is an energetic gain resulting from the π - π interaction between the central rings. Nucleus independent chemical shift (NICS) have been calculated by D. Dudenko for the HEXAGON and the TRIANGLE, illustrated in Figure 4.39a and b [SEBASTIANI 05]. These maps reflect the areas where the influence of the aromatic rings can shift in the solid state, e.g. the chemical shift of the ^1H . Thus, a closer distance between two molecules, e.g. in the TRIANGLE, would allow the protons to enter in other aromatic ring current regions, which might be an explanation for the observed shift in the solid-state NMR spectrum (top spectrum in Figure 4.38a and b) compared to the solution-state spectrum (spectrum below in Figure 4.38a and b).

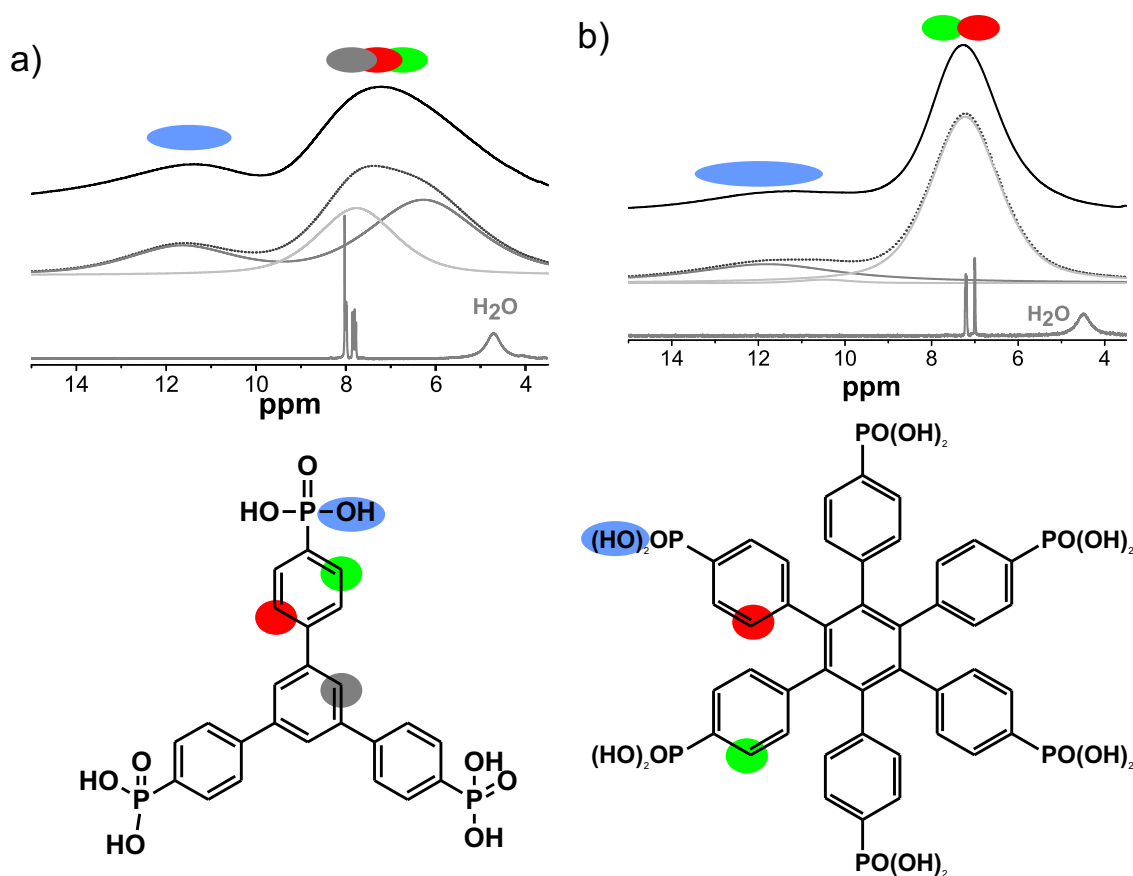


Figure 4.40: ^1H solid-state MAS NMR spectra recorded at 30 kHz spinning (700.1 MHz, 16.4 T) is shown on the top, below the deconvoluted peaks are plotted and at the bottom the liquid spectra recorded in DMSO at 100°C (500.2 MHz, 11.7 T) is shown for a) the TRIANGLE and b) the HEXAGON.

A comparison of an ^1H MAS NMR spectra for the investigated geometrical shapes shows, that the δ_{iso} of some aromatic protons are shifted towards higher field except in the HEXAGON, see Figure 4.40b. The liquid-state ^1H NMR signals of the TRIANGLE are located around 8 ppm and the corresponding signals for HEXAGON at 7 ppm. Changing to the solid state, the TRIANGLE shows a partial shift of these signals towards 6 ppm, while the HEXAGON stays constant at 7 ppm c.f. Figures 4.40a and b. In contrast, to the SQUARE discussed above, a deconvolution results in two different displacements ranging from 1 to 2 ppm. This might be an indication that the shifted proton resonance corresponds to different arrangements of the aromatic rings. The ^1H MAS NMR and liquid NMR spectra of the SCREW and TETRAHEDRON also show high-field shifts but have not provided any new information and can therefore be found in the Appendix A.

DQ NMR is used to reveal information about the dynamic of protons as mentioned in subsection 4.3.1. In addition, 2D ^1H - ^1H DQ measurements can reveal information about intermolecular distance between e.g. the PA groups, as presented in part I subsection 2.3.2. Here, this method is used to probe and determine PA proton proximities. Figures 4.41, 4.42, and 4.43 show the 2D BaBa spectra of the LINE, SQUARE, SCREW, and TRIANGLE at different temperatures. As mentioned in subsection 2.3.2, mobile protons may also decrease the signal intensity observed in a ^1H - ^1H DQ spectrum. Hence, comparing the spectra at 51°C and at low temperature -15°C it can be revealed if the proton mobility affects the spectra. In particular, if the protons exchange is too fast, no autocorrelation peak of the PA protons is observed. This is often the case at ambient temperature, however, the motion can in some cases be slowed down, resulting in an autocorrelation peak observed only at low temperature [LEE 07b]. The LINE shows already at room temperature an autocorrelation peak for the hydrogen bond signal indicating no observable mobility in the NMR, as illustrated in Figure 4.41. Thus, as conducted before, the PA protons of the LINE are quite immobile and thereby does not represent a good conductor.

In Figure 4.42a,b, the 2D DQF spectra of the SQUARE at ambient and low temperature are shown. The PA proton of the SQUARE seems to be more mobile than the LINE since there is no autocorrelation signal at room temperature, but at low temperatures. The explanation might be that due to higher motion at RT the auto signal cannot be detected. Apparently, as a result of freezing the motion at low temperatures, the signal

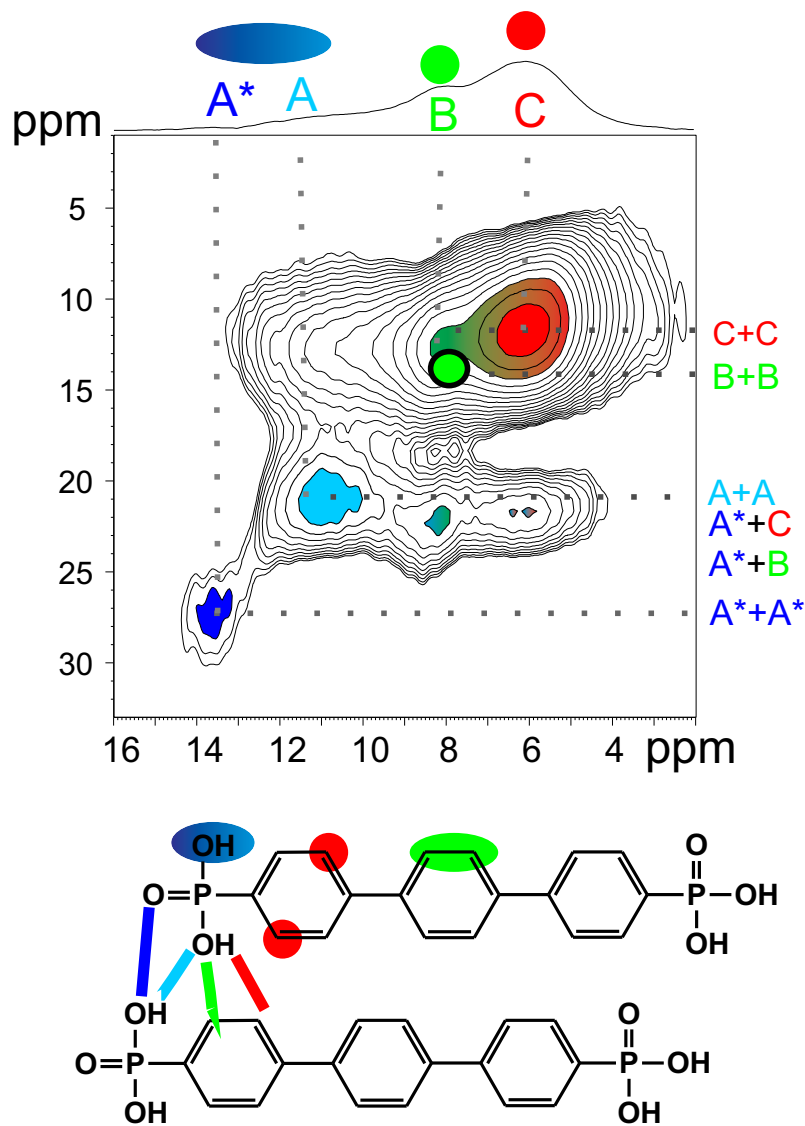


Figure 4.41: 2D $^1\text{H}-^1\text{H}$ MAS NMR DQ-SQ correlation spectrum of the LINE using a spinning frequency of 29762 Hz (700.1 MHz, 16.4 T) recorded at 51°C and acquired under the following experimental conditions: $\tau_{(\text{exc.})} = 33.6\mu\text{s}$, 516 t1 increments in the indirect dimension for a time step of 16.8 μs , a relaxation delay of 20 s, and 68 transients per increment. Sixteen positive contour levels are shown between 16% and 99% of the maximum peak intensity are plotted. The projection of the direct dimension is shown on the top. The assignment is indicated is shown below.

appears. In contrast, the TRIANGLE and the SCREW show an autocorrelation peak neither at room temperature shown in Figure 4.43b and d, nor at low temperature,

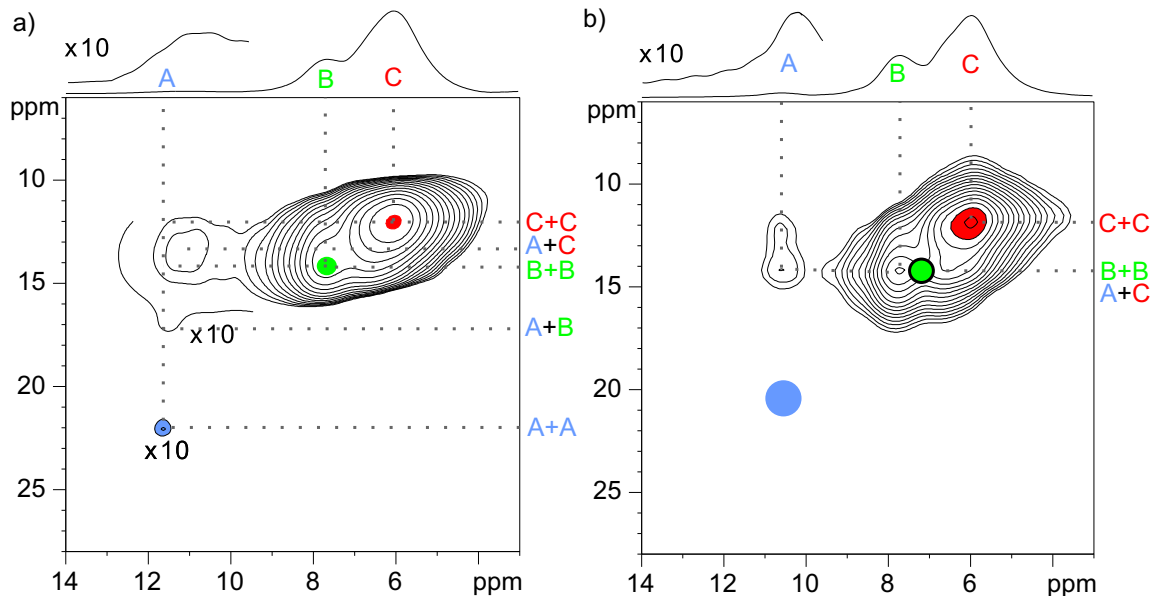


Figure 4.42: 2D $^1\text{H}-^1\text{H}$ MAS NMR DQ-SQ correlation spectra of the SQUARE using a spinning frequency of 29762 Hz (700.1 MHz, 16.4 T) recorded at a) -15°C and b) 51°C and acquired under the following experimental conditions: $\tau_{(\text{exc.})} = 33.6\mu\text{s}$, 2048 t1 increments in the indirect dimension for a time step of $16.8\mu\text{s}$, a relaxation delay of 2 s, and 104 transients per increment. Sixteen positive contour levels are shown between 2% (4%) and 96% (96%) of the maximum peak intensity are plotted. The projection of the direct dimension is shown on the top.

compare with Figure 4.43a and c. Unlike the TRIANGLE, in the spectrum of the SCREW appears a new peak at low temperature which is correlated to a weaker PA at 11.5 ppm 4.43c. This peak at 11.5 ppm might correspond to a PA site with a smaller $\text{O}\cdots\text{O}$ distance.

In general, an autocorrelation peak for a PA group can also originate from the two OH groups which are connected at the same phosphorous in a tetrahedral like angle. Consequently, the two protons would be close enough to another to result in an autocorrelation signal. The absence of an autocorrelation peaks both in the TRIANGLE and the SCREW may exclude this assumption. Hence, the presence of an autocorrelation peak might suggest a higher proximity of the hydrogen bonds. Thus, the results from the 2D DQF spectra are in good agreement with the chemical shift $\text{O}\cdots\text{O}$ distance mentioned above. This observations yield the result that the distance in the PA groups, e.g., for the TRIANGLE is better for the proton conduction, where in the LINE the PA are relative close

and thus forming too strong hydrogen bonds. The behavior of the HEXAGON (Figure shown in the Appendix A) is rather analogous to the TRIANGLE which agrees with earlier observations of the bulk proton conductivity in section 4.1.

4.4.5 Structural features from $^{13}\text{C}\{^1\text{H}\}$ MAS NMR

Insight in the solid-state organization of the samples are also provided by $^{13}\text{C}\{^1\text{H}\}$ cross polarization (CP) MAS NMR. Upon comparison of the liquid and the solid-state NMR spectra one can clearly observe that the peaks not only will be broader but also are shifted. Some to higher and some to lower ppm values. This can be due to different effects:

- packing
- limited mobility
- $\pi - \pi$ stacking

In general, all three effects have an influence on the chemical shift. However, since the molecules studied here all include aromatic systems the effect of $\pi - \pi$ stacking is most probable present [LAZZERETTI 00]. Furthermore, it is a typical packing effect which rises from the ring-current in aromatic moieties and is of great use in molecular structure determination [BROWN 01]. Considering a benzene ring there are two different regions, the first is located above and below the molecular plane and the second orthogonal. These regions will be different in the geometrical structures due to the turning of the aromatic rings and the it strongly depends on the location of each ^{13}C next to another ring whether it is shifted to higher or lower chemical shift values [GOMES 01].

Above the plane an atom will experience a deshielding due the induced magnetic field, leading to a difference in the chemical shift values. In contrast, if the atom is located at the side of the aromatic ring the values become smaller. Additionally, one has to recall that the structures drawn in Figure 4.1 are just a 2-dimensional view. This is not their real orientation neither in the liquid nor in the solid phase. The aromatic rings are twisted to

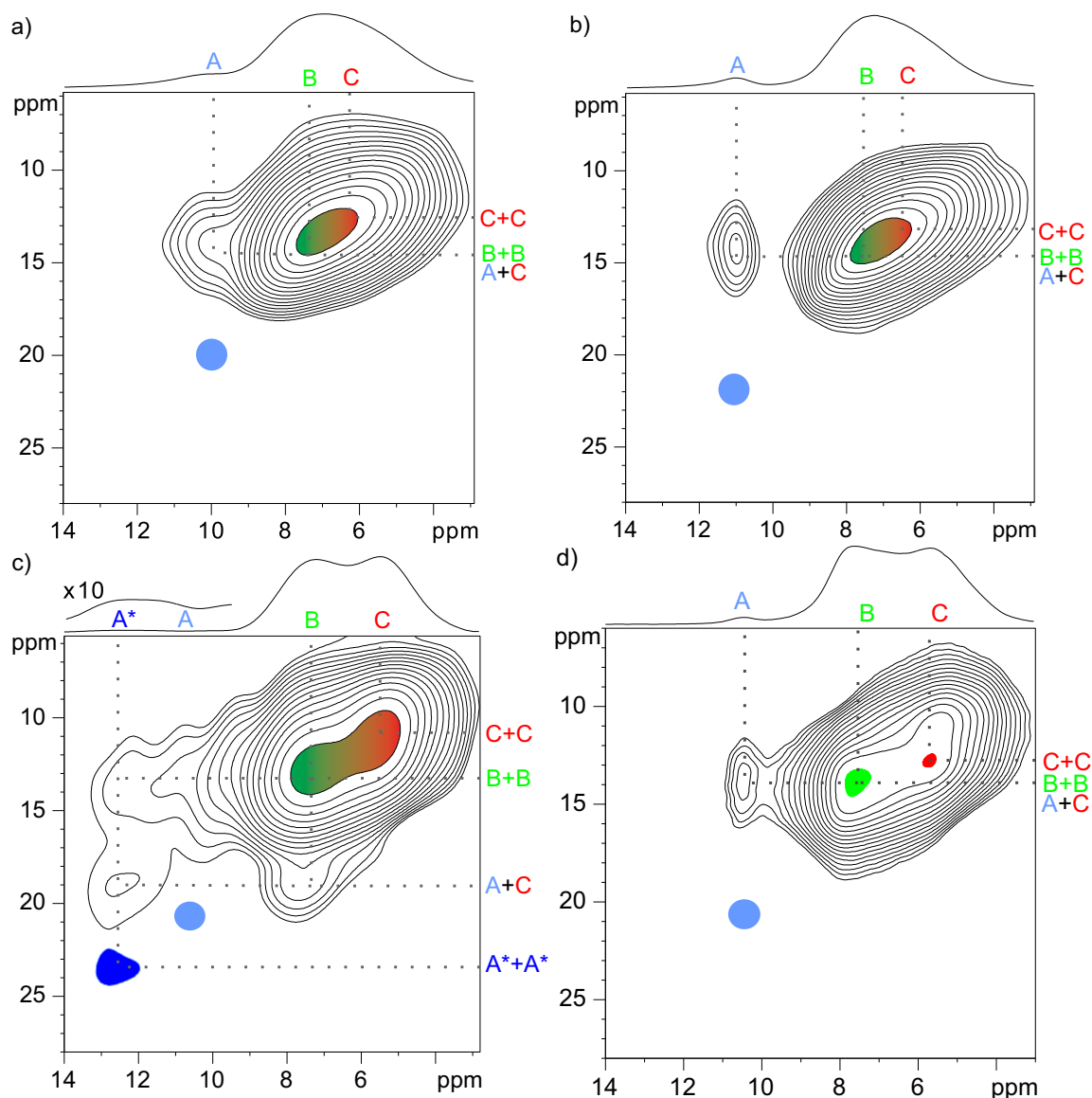


Figure 4.43: 2D $^1\text{H}-^1\text{H}$ MAS NMR DQ-SQ correlation spectra using spinning frequency of 29762 Hz (700.1 MHz, 16.4 T).

The TRIANGLE recorded at a) -15°C and b) 51°C and acquired under the following experimental conditions: $\tau_{(\text{exc.})} = 33.6\mu\text{s}$, 2048 t_1 increments in the indirect dimension for a time step of $16.8\mu\text{s}$, a relaxation delay of 20 s, and 96 transients per increment. Sixteen positive contour levels are shown between 11% (7%) and 90% (86%) of the maximum peak intensity are plotted. The projection of the direct dimension is shown on the top.

The SCREW recorded at c) -15°C and d) 51°C and acquired under the following experimental conditions: $\tau_{(\text{exc.})} = 33.6\mu\text{s}$, 2048 t_1 increments in the indirect dimension for a time step of $16.8\mu\text{s}$, a relaxation delay of 10 s, and 96 transients per increment. Sixteen positive contour levels are shown between 2% (4%) and 96% (98%) of the maximum peak intensity are plotted. The projection of the direct dimension is shown on the top.

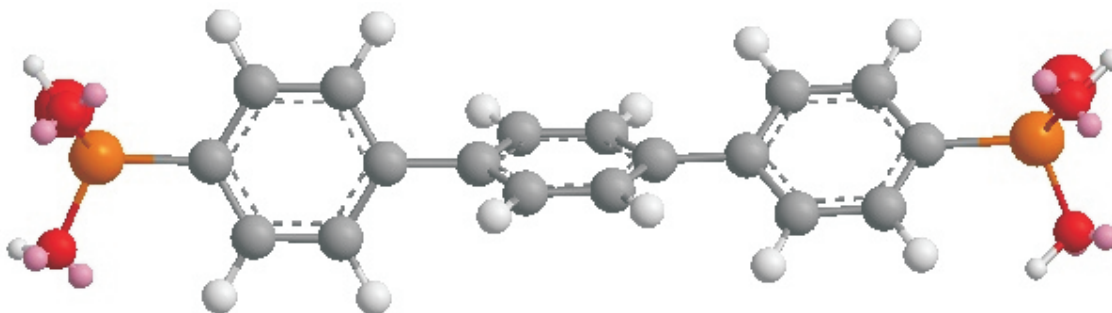


Figure 4.44: 3D structure obtained from ChemDraw 3D MMFF94 calculation of the LINE.

some extent to reach an optimal energy between the energetic gain from the π system and loss due to the repulsion of the ortho CH groups [JOHANSSON 08]. The geometrical shape of the LINE in the gas phase has been calculated with ChemDraw 3D MMFF94 and is shown in Figure 4.44.

With the above monitored effects in mind, the $^{13}\text{C} \{^1\text{H}\}$ CP MAS NMR spectrum of the LINE, shown in Figure 4.45a, is analyzed in more detail. This spectrum displays resonances in the aromatic region from 120 to 145 ppm. Between 135 and 145 ppm the quaternary carbons are located, while the CH are found around 120 to 133 ppm. Indeed, signal splitting is observed in liquid-state NMR spectra originating from a $J_{^{13}\text{C}^{31}\text{P}}^2$ coupling (11 Hz) which falls in the expected range [HESSE 95]. In the solid state this coupling cannot be observed since the broad lines overlap. In contrast to the liquid spectrum of the LINE the solid state spectrum includes more signals than expected, possibly explained by breaking the molecular symmetry due to packing. In the liquid the LINE has a C2 symmetry axis since there is for each symmetric carbon just one corresponding peak. In the solid-state $^{13}\text{C} \{^1\text{H}\}$ CP MAS NMR spectrum one can observe a splitting of the CH signals. This effect is well resolved for the CH group at 123 and 124 ppm, marked in grey in Figure 4.45b.

As a result of packing, also the aromatic ring current can affect the chemical shifts of nuclei which are located within their vicinity. This can be in fact quite long-ranged, with an aromatic ring still exerting an influence at a distance of 0.7 nm [LAZZERETTI 00]. Also, the ring current effect is not restricted affecting protons only but can obviously

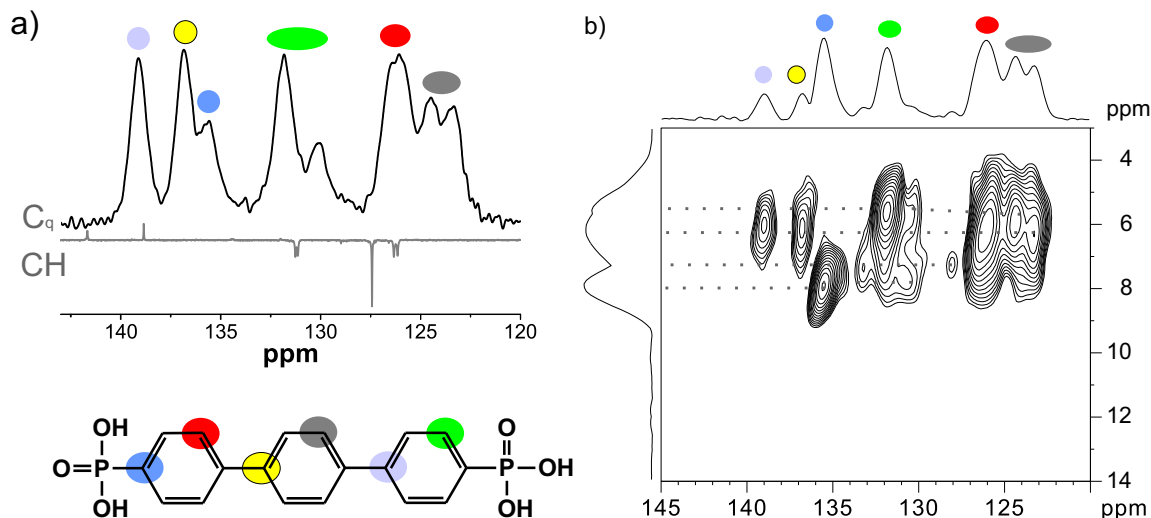


Figure 4.45: a) Solid-state $^{13}\text{C} \{^1\text{H}\}$ CP MAS NMR spectrum at 20 kHz spinning (125.8 MHz, 7.0 T) on the top, showing underneath the liquid DEPT-135 spectrum in DMSO at 100°C, with a coupling constant of $J_{^{13}\text{C}^{31}\text{P}}^2 = 11$ Hz.

b) 2D $^{13}\text{C} \{^1\text{H}\}$ MAS REPT-HSQC spectrum of the LINE at 29762 Hz spinning (213.8 MHz, 19.9 T) plotting projections along the ^{13}C and ^1H NMR axis respectively on the top and on the left, respectively.

also influence other nuclei such as carbon [BROWN 01]. However, the effects are much more pronounced for ^1H NMR due to the small chemical shift range and the usual exposed position of the protons in the molecule. Since single crystals X-ray diffraction data from the LINE could not be obtained, a $^{13}\text{C} \{^1\text{H}\}$ MAS REPT-HSQC spectrum has been recorded, shown in Figure 4.45b, to reveal further information about the structural packing of the LINE. In this spectrum a correlation between ^{13}C and ^1H is observed. Notably, the ^1H chemical shift is unaffected by changing from the liquid to the solid state, compare subsection 4.4.4. In addition, this unaffected ^1H corresponds to a ^{13}C in the quaternary region. In general, if a proton shows a change of an absolute chemical shift, the corresponding carbon spectrum should show approximately the same. Hence, the $^{13}\text{C} \{^1\text{H}\}$ CP MAS and REPT-HSQC NMR spectrum makes it possible to get some information about the structure.

^{13}C chemical shifts of the phosphonic acid containing rings are shifted to higher field. Thus, considering possible π shifts, they have to be located close to the side of another aromatic ring. On the other hand, no ^{13}C chemical shift changes are observed

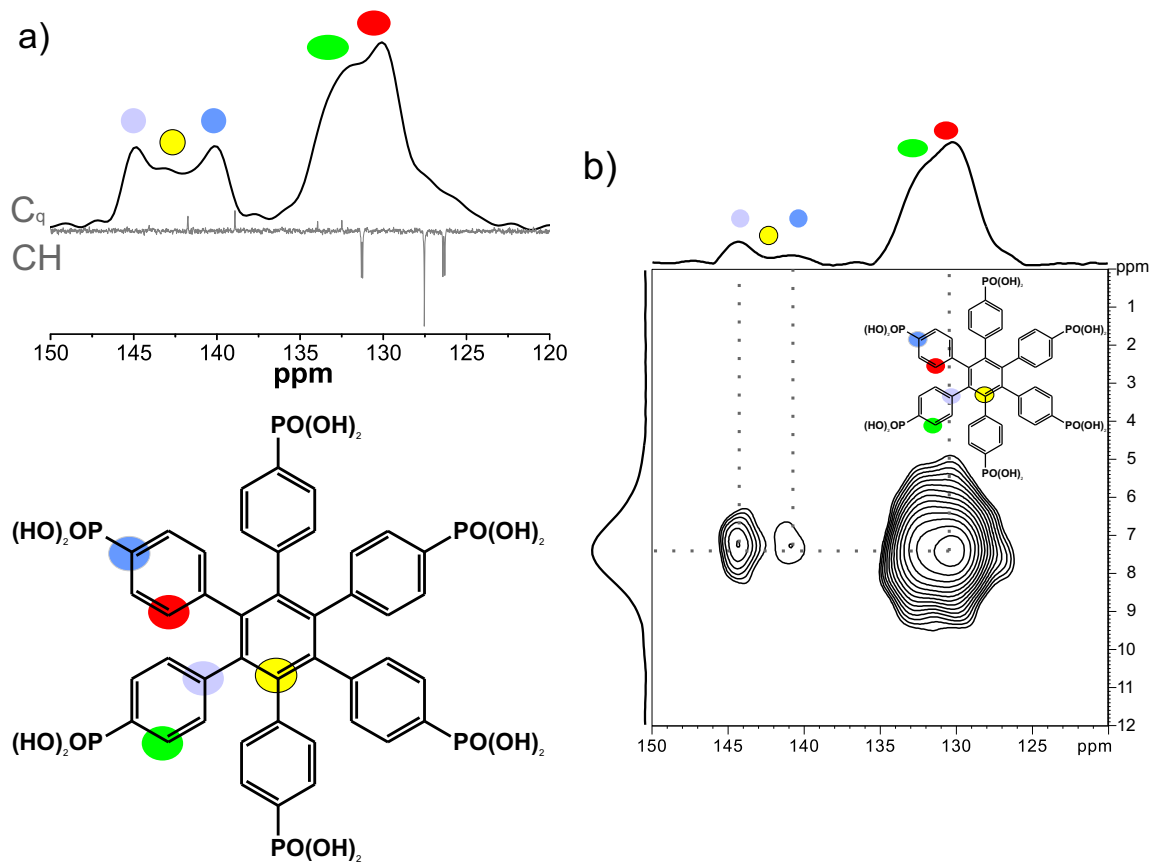


Figure 4.46: a) $^{13}\text{C} \{^1\text{H}\}$ CP MAS NMR spectrum of the HEXAGON at 20 kHz spinning (125.8 MHz, 7.0 T) on the top, showing underneath the liquid DEPT-135 spectra in DMSO at 100°C.

b) $^{13}\text{C} \{^1\text{H}\}$ MAS REPT-HSQC of the HEXAGON at 29762 Hz spinning (213.8 MHz, 19.9 T) plotting projections along the ^{13}C and ^1H NMR axis respectively on the top and on the left.

for the central aromatic CH. This suggests that a possible location in a region unaffected by the ring current.

By comparing the obtained ^{13}C signal from the $^{13}\text{C} \{^1\text{H}\}$ CP MAS spectrum with the 2D $^{13}\text{C} \{^1\text{H}\}$ REPT-HSQC spectrum of the HEXAGON, a signal loss of the quaternary carbons is observed (c.f. Figure 4.46a and b). In Figure 4.46a, the quaternary carbon marked yellow shows the lowest intensity representing the carbon of the central aromatic ring. This is supported by the fact that this signal has no corresponding intensity in the $^{13}\text{C} \{^1\text{H}\}$ REPT-HSQC spectrum. There are no protons near by which may be able to

transfer any polarization to quaternary ^{13}C marked yellow in Figure 4.46a and b. This observation of complete signal reduction of a quaternary ^{13}C cannot be observed for the other geometrical structures. In contrast the HEXAGON all the remaining ionomers do have at least two additional CH groups in the central ring which supports the signal assignment.

In addition, Figure 4.46b shows a not so dramatic but detectable and differential signal reduction of the other two quaternary carbons. This observation might arise from the location of the aromatic rings in the HEXAGON structure among one another. Hence, the difference in reduction, comparing the blue and the purple marked quaternary carbon, might result from a more or less strong polarization transfer, originating from the protons located at the neighboring ring. Accordingly the assignment is as followed, the blue marked quaternary carbon represents the PA connection and the purple marked carbon the aromatic conjunction between the two aromatic rings, as shown in Figure 4.46.

For a closer look on the ^{13}C results the ^{13}C CP MAS NMR spectra of the LINE, SQUARE, TRIANGLE, and HEXAGON are compared, c.f. Figures 4.45, 4.47 and 4.46. The chemical shifts of the LINE were analyzed already above. Comparing the ^{13}C line width of the different geometrical shapes it results that a broad range can be found. The LINE and the SQUARE show a quite good resolution with a line width of 120 Hz for the LINE and 50 Hz for the SQUARE, c.f. Figure 4.45a and 4.47b. Additionally, most of the signals are clearly resolved. In contrast to those observations, the TRIANGLE and HEXAGON show rather broad signals, one for both the quaternary and for the CH ^{13}C signals. This is an indication of a higher ordered system in the case of the LINE and the SQUARE, while the TRIANGLE and HEXAGON are rather disordered. Beside the assigned peaks in the ^{13}C $\{^1\text{H}\}$ REPT-HSQC spectrum of the LINE minor additional signals are found, e.g. in Figure 4.47b at 132 ppm. Liquid NMR of the LINE was repeated after solid-state NMR experiment to prove the stability of the sample. Since the spectra did not reveal any difference one can claim that this sites are correlated to different packing positions of the carbon.

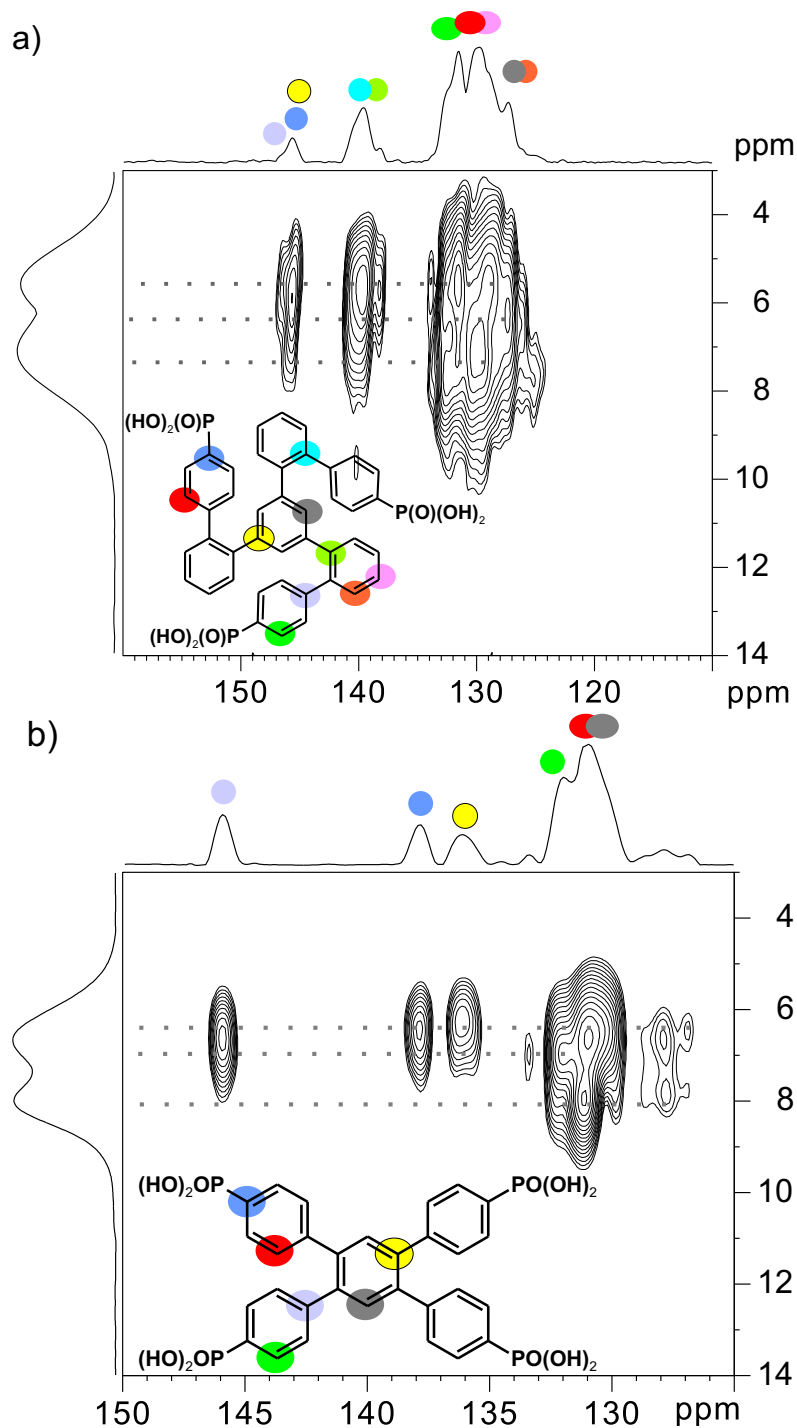


Figure 4.47: a) $^{13}\text{C} \{^1\text{H}\}$ MAS REPT-HSQC of the SCREW at 29762 Hz spinning (213.8 MHz, 19.9 T) plotting projections along the ^{13}C and ^1H NMR axis respectively on the top and on the left.

b) $^{13}\text{C} \{^1\text{H}\}$ MAS REPT-HSQC of the SQUARE at 29762 Hz spinning (213.8 MHz, 19.9T) plotting projections along the ^{13}C and ^1H NMR axis respectively on the top and on the left.

4.4.6 Mobility of the aromatic moiety using REPT-HDOR experiments

In order to determine the influence of possible ring flips on the dynamics hydrogen-bonding network, ^1H - ^{13}C dipolar couplings of the aromatic rings were determined via $^{13}\text{C}\{^1\text{H}\}$ recoupled polarization transfer - heteronuclear dipolar order (REPT-HDOR) (c.f. chapter 2.3.3). The basic idea is that through the information about rotational motion of the aromatic rings one may conclude indirectly about the fixation or motion of the PA. It may be possible, that due to the motion of the aromatic moiety, the motion of the proton might be perturbed or supported. Hereby, one can assume that if there is a fast motion of the aromatic ring the attached PA may not form a stable hydrogen bonds cluster. Otherwise, the P-C bond can rotate freely and might not be effected by the motion of the aromatic moiety at all. Due to recoupling of the heteronuclear dipolar-dipolar interaction, the mobility of the aromatic CH protons can be determined. By using a program, developed in the Spiess group, the resulting side band patterns can be determined and the dipolar coupling constant (D) extracted. A complete immobile ^{13}C - ^1H spin pair is characterized by a coupling of $D_{\text{CH}} = 21$ kHz [FISCHER 04]. Molecular motion can reduce by this coupling provided that the motion is larger than > 100 kHz. For easier comparison it is common to use a so-called order parameter S instead of the D. This parameter is defined by equation 4.4. In the complete immobile case it is equal to 1.

$$S = \frac{\text{dipolar coupling}}{\text{dipolar coupling rigid sample}} \quad (4.4)$$

Several similar structures have already been analyzed using $^{13}\text{C}\{^1\text{H}\}$ REPT-HDOR. Polyphenylene dendrimers are a comparable example for the HEXAGON system and show a dipolar coupling constant for the CH groups of 20.5 kHz [WIND 01]. A more mobile compound is the benzyloxy benzyl methacrylate which is also represented by the D value of the aromatic CH with 16.1 kHz. It is claimed that even in this system a value of 16.1 kHz indicates that the phenyl ring flip is inhibited. Such a flip would be associated with a reduction of the coupling to 12.8 kHz [RAPP 03]. Since the dendritic system is more strongly hindered in rotation than the benzyloxy benzyl methacrylate, the ionomers in this work would be expected to have a dipolar constant in between. The best sample to

compare with is poly(*p*-phenylenes) with short ethylene oxide side chains [MIERZWA 02]. It has aromatic-aromatic bonds and hindered the rotation, yielding a value of $D_{CH} = 18.8$ kHz. Values close to this can also be found in several geometrical shapes as listed in Table 4.3, except for the TRIANGLE and the TETRAHEDRON, which allow rotation in the structure thereby yielding values for the order parameter comparable to a phenyl ring flip [SPIESS 83, GRAF 07]. Especially the TRIANGLE with 0.64 is very close to the order parameter for a 180° flip of 0.62. A more general determination of the dipolar coupling constant was provided by Hentschel et al. using ^2H NMR spectroscopy [HENTSCHEL 81]. They determined corresponding rotation angles and order parameters, resulting in a $S \sim 0.8$ for an angular motion of $\pm 15^\circ$ and $S \sim 0.7$ of $\pm 20^\circ$ respectively. These values will in the following be used to define the range of motion and are not considered as the absolute value.

Sample	Dipolar coupling [kHz]	Order parameter S	angle motion [°]
Line	17.9	0.85	$\pm 10^\circ$
Triangle	13.4	0.64	$\pm 180^\circ$ phenyl flip *
Screw	17.0	0.81	$\pm 15^\circ$
Tetrahedron	14.7	0.70	$\pm 180^\circ$ phenyl flip *
Square	16.6	0.80	$\pm 15^\circ$
Hexagon	16.9	0.80	$\pm 15^\circ$

Table 4.3: $^{13}\text{C}\{^1\text{H}\}$ REPT-HDOR results for the CH protons next to the phosphonic acid. The error deviation is estimated to be for $S \pm 0.5$. The angular motion corresponding to the values obtained from literature ⁺[MIERZWA02]*[GRAF07].

Comparing the order parameter listed in table 4.3 one can see, that the ring mobilities are in the expected range for aromatic moieties. Moreover, one can divide the geometrical shapes in three different groups: rigid, intermediate, and mobile. Of course, this classification is just valid for comparing these geometrical shapes where CH order parameters are determined, as the order parameter of a CH_3 group were in the range of $S \sim 0.3$ [GARROW 98]. In the case of unsubstituted biphenyl, the equilibrium torsional angle is 44.4° and the torsional barriers are 6.0 kJ/mol at 0°C and 6.5 kJ/mol at 90°C [JOHANSSON 08]. Therefore, basically all geometrical shapes, except the

TETRAHEDRON, should reveal similar C-H mobilities. Certainly, one has to consider the substitutional effects of the further aromatic rings in the system.

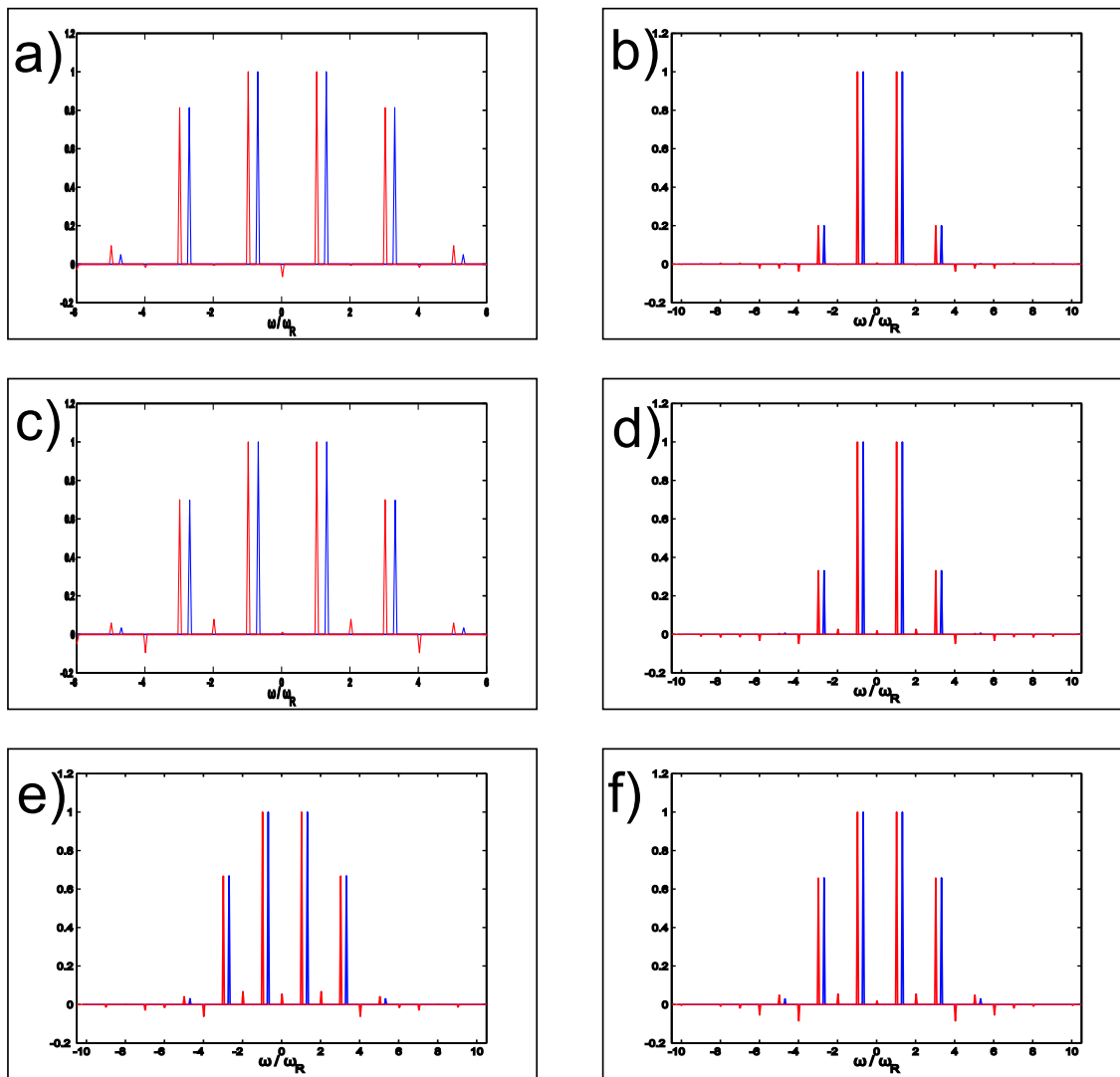


Figure 4.48: $^{13}\text{C}\{^1\text{H}\}$ REPT-HDOR MAS NMR recorded at 25 kHz spinning (213.8 MHz, 20.0 T) with a t_1 increment of 20 μs , recoupling time $2\tau_r$ and 1k scans for a) LINE b) TRIANGLE c) SCREW d) TETRAHEDRON e) SQUARE f) HEXAGON.

Starting from this expectation the relative mobile ionomers should be the LINE, the TETRAHEDRON and the TRIANGLE, since their geometrical shape has no substitution in the ortho position which implements a high degree of freedom. Consequently, the

order parameter of the TETRAHEDRON and the TRIANGLE suggest higher motion even a phenyl flip of 180° is highly probable. Whereas, the LINE unexpectedly shows the highest dipolar coupling constant of $S \sim 0.85$ which represents a motion of $\pm 10^\circ$. This means it shifts from being expected to be the most mobile sample to the most rigid. Thus, the relative high order parameter in LINE has to be explained by the micro structural order of the sample in the solid.

For steric reasons, it is expected that the substitution of two ortho hydrogens by larger atoms or groups should lead to an increase of the torsion angle [GREIN 02]. The mediate samples including the SCREW, SQUARE and HEXAGON have an order parameter in the range of $S \sim 0.80$ possibly reflecting an angular motion of $\pm 15^\circ$. This suggest that in the microcrystalline structure there is less space for rotational motion. A comparison of the order parameter with the activation energy does not reveal a useful correlation. These results might possibly indicate that larger motion may support ^1H motion that contribute to bulk conductivity. However, it seems that angular motion has no negative influence on the hydrogen bond network.

4.5 Conclusion

In this chapter the concept of using low molecular weight compounds as proton conductors was investigated. The study has been carried out on ionomers based on aromatic moieties and phosphonic acid (PA) groups combined to form different geometrical shapes: LINE, TRIANGLE, SCREW, SQUARE, TETRAHEDRON, and HEXAGON. In the temperature range from 110°C to 120°C the HEXAGON and the TRIANGLE show a bulk proton conductivity above 10^{-3} S/cm at different relative humidities for the respective temperatures. The presented impedance spectroscopy, ^1H , and ^2H MAS NMR data suggest that proton conductivity is most likely explained by incorporated water. Moreover, the ^{31}P MAS NMR data combined with TGA-MS support this assumption. This result is in contrast to the observation of the state-of-the-art, proton conducting polymers like Nafion[®] and PVPA [LEE 07a]. It seems that this water dependency for the HEXAGON provides a high and fairly constant proton conductivity especially in the high temperature regime. This rather uncommon behavior of a constant proton conductivity reflects the presence of various hydrogen bond strengths as a result of PA water interactions in the bulk. Different PA water sites are also suggested by the data obtained by ^1H and ^{31}P MAS NMR measurements at varied relative humidity.

In general, the amphoteric character of the PA groups and the incorporated water support the proton conductivity. Therefore, the question rouse why some geometrical shapes show relatively high and others insulator like bulk proton conductivity. From single crystal X-ray diffraction the formation of a columnar structure in the HEXAGON formed by the hydrophobic aromatic core can be proposed. By using computations based on WAXS data possible structures containing additional water were obtained. Thus, it is most probable that the PA groups in the HEXAGON form a zigzag pathway through the sample. The TETRAHEDRON on the other hand forms isolated tetrameric clusters restricting the mobility of the PA protons. Hence, the bulk proton conductivity most likely depends on how the PA are connected, suggesting that some geometrical shapes conduct while others show an insulator bulk proton conductivity.

The current study provides a detailed understanding of the ionomer approach. Similar systems with different configurations have been investigated, which will help to elucidate

the conductivity phenomenon. The rational design of proton conductors requires insights into the structure on molecular level. A combination of advanced solid-state NMR, X-ray, and thermogravimetric methods can provide detailed information on structure and dynamics of such systems. Therefore, low molecular weight organic crystals with incorporated water are therefore promising materials to be used as PEM, e.g. for automotive applications.

4.6 Spacer concept

This approach aims at increasing the distance between the backbone of the polymer and the functional group which is referred to *spacer-length*, as shown in Figure 4.49b. The spacer concept has been successfully applied to enhance proton conductivity of heterocycle based systems [PADDISON 06]. In case of imidazole, the heterocycle were attached to polymer backbones via flexible spacers such as ethylenoxide or alkane segments, as seen in Figure 4.49a. Notably, the proton mobility increased with increasing spacer length. This increase even overcompensated the dilution effect with respect to the change in spacer length [PADDISON 06]. It is anticipated that, flexibility of long spacers facilitates an aggregation of terminating protogenic groups, corresponding to the formation of hydrogen bonded structures and networks. The results from Steininger et al. clearly indicate that the *spacer concept* fails in the case of PA functionalized polymers [STEININGER 07]. Here, proton conductivity significantly decreases with longer alkane segments.

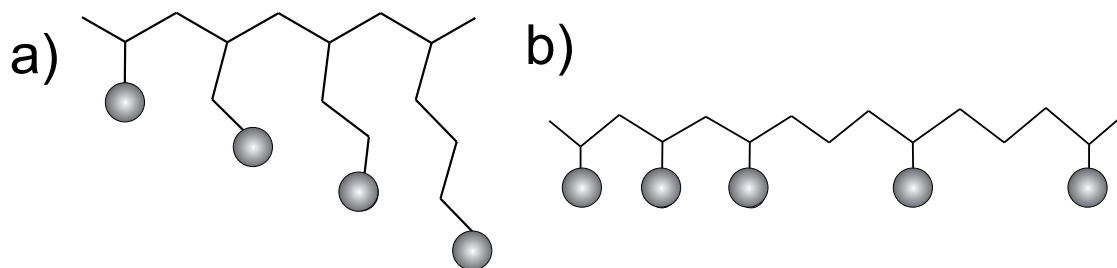
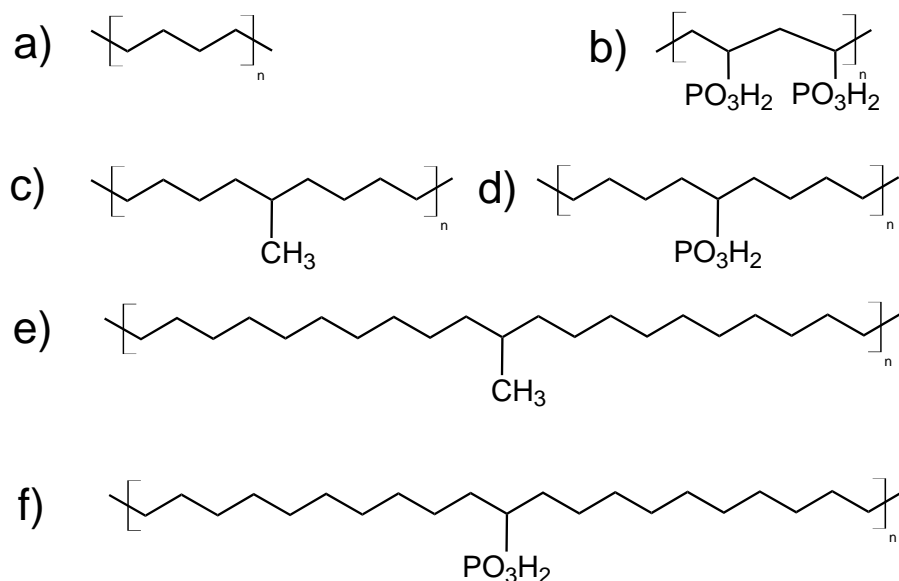


Figure 4.49: Sketch of the intended spacer concept with a) increasing spacer length between backbone and functional group and b) increasing spacer length between the functional groups.

PA functionalized homo- and copolymers have gained increasing interest due to their promising properties which include chemical separation, ion exchange, and ion conductive membranes. The PA in general is known to be a good protogenic group which can be easily introduced to the backbone of polymers, e.g. as shown in the case of poly(vinylphosphonic acid) (PVPA) [BINGOEL 06].

In this work the same basic idea of an increasing spacer is used. Unlike the way of en-



	IUPAC	Abbreviation	Literature
a	Poly(ethylene)	PE	[WEI 09]
b	Poly(vinylphosphonic acid)	PVPA	[LEE 07a]
c	Poly[ethyl(9-methyl)]	PE9-Me	[WEI 09]
e	Poly[ethyl(21-methyl)]	PE21-Me	[WEI 09]
d	Poly[ethyl(9-phosphonic acid)]	PE9-PA	
f	Poly[ethyl(21-phosphonic acid)]	PE21-PA	

Table 4.4: List of the investigated polymers including their abbreviation due to the spacer extended poly(vinylphosphonic acid).

larging the distance between the backbone and the functional group a *spacer* between the PA was introduced in the polymer chain. The focus of interest was how this spacer insertion will affect the conduction properties. The question is whether the polymer forms a channel or cluster system with the hydrophilic groups. This cluster is intended to conduct only protons and not water as it is the case in NAFION[®].

Therefore, regularly spaced acid groups were inserted in a polyethylene backbone. This was achieved by using the **acyclic diene metathesis** (ADMET) polymerization. The phosphonic acid groups could be precisely placed on every 9th and 21th carbon molecule, as shown by K. Opper [OPPER 09] from the University of Florida (USA) . The abbrevia-

tions used for the different polymers are listed in table 4.4. Due to the stepwise dilution of the PA groups, it is expected to reveal a decrease of PA-PA interactions. Furthermore, it should be possible to observe a transition from the PVPA to polyethylene (PE) behavior. PE is already known to give a variety of microstructures and morphologies [YAO 07]. It is known from literature that specific properties for particular applications can be target by incorporating polar functionalities into PE [BOFFA 00]. Consequently, different functionalized PE polymers were compared, as represented in Figure 4.6.

The systems were analyzed using ^1H , ^{13}C and, ^{31}P MAS solid-state NMR. Methods such as single pulse ^1H MAS, ^1H DQF, and two dimensional ^1H - ^1H DQ spectroscopy were performed. ^{31}P MAS NMR provides additional aspects of structural features since this nuclei is very sensitivity to its surroundings via changes in the chemical shift.

4.6.1 Crystallinity of the polymers followed by ^{13}C MAS NMR and DSC

The $^{13}\text{C}\{^1\text{H}\}$ CP MAS NMR spectra from PE to PVPA shows a transition from crystalline to amorphous polymers, see Figure 4.50a. Thus, the PE-dominated polymers show, besides a glass transition an additional melting point (T_m). The line width of 53 Hz is comparable to the standard adamantane [MORKOMBE03]. On the contrary, PVPA shows a broad line width with a poor resolution. Notably, the corresponding $^{13}\text{C}\{^1\text{H}\}$ CP MAS NMR spectrum of PE21-PA obtained above T_g reveals three resonances at 33.2, 31.7, and 28.8 ppm. These signals can all be assigned to the polymer backbone, depending on the distance to the PA branching. The signal at 37 ppm corresponds to the CH branching group and consequently is more intense in PE9-PA than PE21-PA. Below T_g , however, the CH_2 groups show a poor resolution in both PE9-PA and PE21-PA. Yao et al. have assigned the crystalline part of PE signal to ~ 33 ppm and the amorphous to ~ 31 ppm [YAO 07]. Therefore, the thermal behavior in PE21-PA may be explained by the melting of the crystalline part. Two additional new signals are observed in PE9-Me and PE21-Me and these are assigned to the methyl group at 19 ppm and the branching CH group at 40 ppm.

Figure 4.50b shows three single-pulse $^{13}\text{C}\{^1\text{H}\}$ CP MAS NMR spectra, of PE21-PA,

recorded at different temperatures. A single-pulse experiment with proton decoupling was chosen to analyze the spectra quantitatively. At 0°C both the peaks at 33.3 ppm and ~ 31 ppm are present. Deconvolution shows an amount of 18% crystallized phase. This amount decreases with increasing temperature until no signal is left when the temperature exceeds the glass transition (25°C). After the first heating and cooling the percentage rises to 33% at room temperature. This indicates that the crystalline part is higher when the sample is cooled down from melt than by precipitation from solution, similarly to the reported results of PE [YAO 07]. Consequently, as expected, the morphology of PE21-PA is mainly affected by the PE part and not by the PA inserts. In contrast, PE9-PA shows a broad amorphous peak below its T_g and does not exhibit a sharp peak at ~ 33 ppm, see Figure 4.50a. By increasing the temperature above the T_g a better resolution is obtained. Thus, the crystalline part is difficult to determine which is a contrary to PE9-Me [WEI 09]. This might also be due to the limited resolution as a result of the broad peaks.

With the above results, one can see that the kind and the number of "defects" in PE with PA can affect the morphology of the polymer significantly. In literature there are more PE polymers with specifically introduced side group. The effects of their different properties on the morphology are obtained by comparing their thermal behavior. A good indicator is the presence or absence of a melting point. Table 4.5 shows the data of the polymers already discussed above, including some examples from literature.

The polar character of the introduced imperfections might have a strong impact on the morphology. Therefore, polymers containing different kinds of groups, such as unpolar methylene or polar chloride, have been compared with PE-PA. Particularly, the effect of an increased number of possible hydrogen bonds have been studied. Theoretically two hydrogen bonds are formed by carboxylic (PE-CA) and three by phosphonic acid compounds. It is also highly likely that hydrogen bonds can form among the chains which also is supported by NMR results. This would prevent the PE crystallization. Consequently, one can observe a transition in the PE-CA as well as in the PE-PA polymer from the amorphous PE9-CA/PA to the semi-crystalline PE21-CA/PA polymer. All polymers containing chloride (PE-Cl) show a T_M which decreases with increasing amount of Cl. They are also characterized by being semi-crystalline as the PE-Me polymers.

Therefore, one can conclude that not only the polarity of the attached groups but also the ability to form hydrogen bonds affects the morphology of the polymer. Fur-

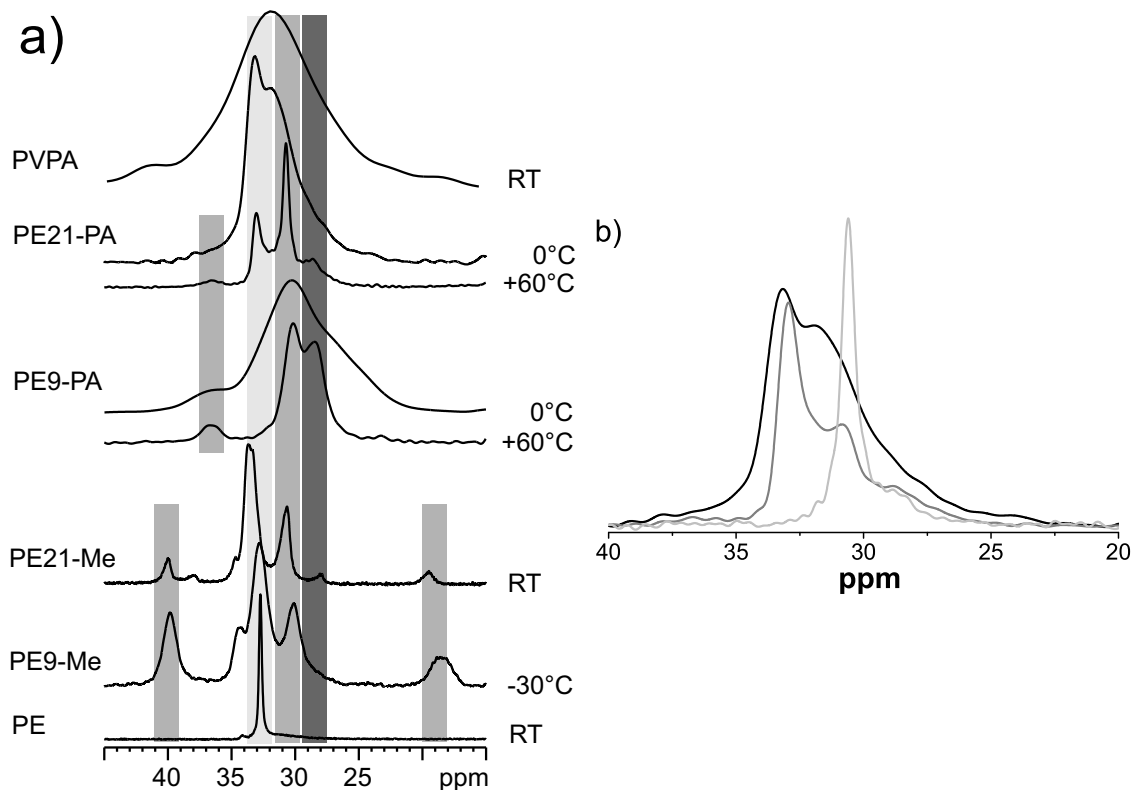


Figure 4.50: $^{13}\text{C}\{^1\text{H}\}$ CP MAS NMR spectra at 20 kHz spinning (125.8 MHz, 11.4 T and 213.8 MHz, 19.9 T) from top to bottom of a) PVPA (RT), PE21-PA (0 and 60°C) PE9-PA (-30 and 60°C), PE21-Me (RT)*, PE9-Me (-30°C)*, PE (RT)*; *[WEI 09]
 b) PE21-PA: 0°C (black), 30°C (dark grey) and 80°C (light grey)

thermore, it seems that the spacer can be used to change the thermal and morphological behavior in a stepwise manner. The higher flexibility, however, does not enhance the proton conductivity significantly even with locally higher ordered structures comparable to PVPA.

4.6.2 Local structure from ^1H and ^{31}P MAS NMR

Assuming that the proton transport depends on the local structure the first step in the analysis is to reveal it. Although, the resolution of the ^1H solid-state NMR is rather poor in this particular case, it provides fast preliminary information. In Figure 4.51, the ^1H and ^{31}P MAS NMR spectra of all three PVPA containing samples are compared. The ^1H MAS NMR spectra show two peaks located at 9.8 ppm and 1.4 ppm taking PE21-PA

Polymer	T _g [°C] ^[a]	T _m [°C]	EN ^[f]
PVPA ^[b]	−23	−	2.65
PE9-PA	25	−	2.65
PE21-PA	25	71	2.65
PE21-Me ^[c]	−44	62	2.40
PE9-Me ^[c]	−43	−9	2.40
PE ^[c]	−	133	−
PE9-CA ^[d]	22	−	2.85
PE21-CA ^[d]	−	45	2.85
PE9-Cl ^[e]	−	41	3.00
PE21-Cl ^[e]	−	81	3.00

Table 4.5: Glass transition T_g, melting point T_m and electronegativity EN of the different polymers: [a] from DSC; [b] [SEVIL 04];

[c] [WEI 09]; [d] [BAUGHMAN 07]; [e] [ALAMO 08]; [f] The different electronegativities were calculated for all groups using

<http://pages.unibas.ch/mdpi/ecsoc/e0002/calelecg.htm>

as an example, as shown in Figure 4.51a. The resonance at 1.4 ppm is assigned to the polymer backbone and the peak at 9.8 ppm to the hydrogen-bonded protons of the PA unit. Integration of both signals corresponds to the expected quantitative ratios in all three samples. This ensures that further measurements reflect the acid groups in its protonated form.

In both the ¹H and ³¹P NMR spectra a line narrowing from PVPA (black) to PE9-PA (dark grey), and PE21-PA (light grey) can be observed. This seems to be due to the dilution and equalization of the chemical surroundings for each PA group. The decrease of intensity from PE9-PA to PE21-PA of the PA corresponding peak at 9.8 ppm is quantitatively correlated to the number of PA per repetition unit.

Since a matter of interest is the proton conductivity it seems reasonable to compare the activation energy obtained from VT ¹H MAS NMR spectra. The question is whether the separated phosphonic acids show similar activation behavior as PVPA. This

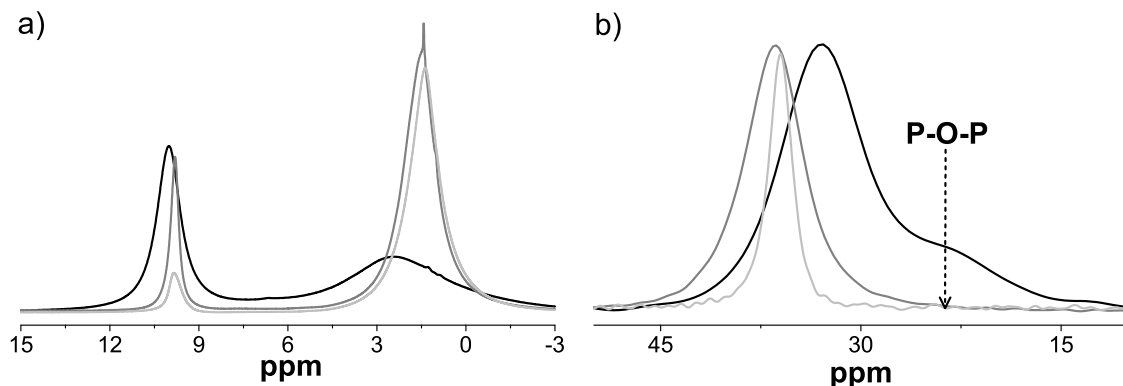


Figure 4.51: Comparing PVPA (black) with PE9-PA (dark grey) and PE21-PA (light grey)
 a) ^1H MAS NMR at 30 kHz spinning (700.1 MHz, 16.4 T) and $T = 20^\circ\text{C}$.
 b) ^{31}P MAS NMR spectra at 20 kHz spinning (202.5 MHz, 11.7 T) of PVPA at 30°C , PE9-PA and PE21-PA at 20°C .

would indicate that either the acidic groups form clusters or the activation energy would not describe the actual transport of protons.

The activation energy of the local motion is obtained by performing VT ^1H MAS NMR experiments. The chosen temperature range must be below T_g which is around 25°C for both PE9-PA and PE21-PA. The glass transition points have been determined using DSC measurements [OPPER 09].

Figure 4.53 shows the VT ^1H and ^{31}P MAS NMR spectra of PE9-PA and PE21-PA. In the temperature range below T_g , the phosphonic acid signal at 9.8 ppm displays a significant line narrowing. This means that the motion reaches the fast limit and thereby fulfills the assumptions of the ARRHENIUS equation as explained in chapter 2.2.5. Above T_g the signal intensity decreases due to the faster motion and leads to a signal loss in solid-state NMR, i.e. in the intermediate regime of motion. PE9-PA and PE21-PA show activation energies (E_A) of 20 and 30 kJ/mol, see Figure 4.52 which is in the range of PVPA 25 kJ/mol [LEE 07]. Activation energies obtained from impedance spectroscopy (IS) reveal slightly higher values of 46 and 48 kJ/mol. These values are roughly the same for PE9-PA, PE21-PA and PVPA (45 kJ/mol). On the other hand, the conductivity of the PE9-PA and PE21-PA at 160°C shows an insulator like values of $9 \cdot 10^{-6}$ S/cm and $1 \cdot 10^{-7}$ S/cm respectively, two orders of magnitude smaller than the obtained value from PVPA $2 \cdot 10^{-5}$ S/cm [BINGOEL 07]. Combining these results suggest that the bulk proton

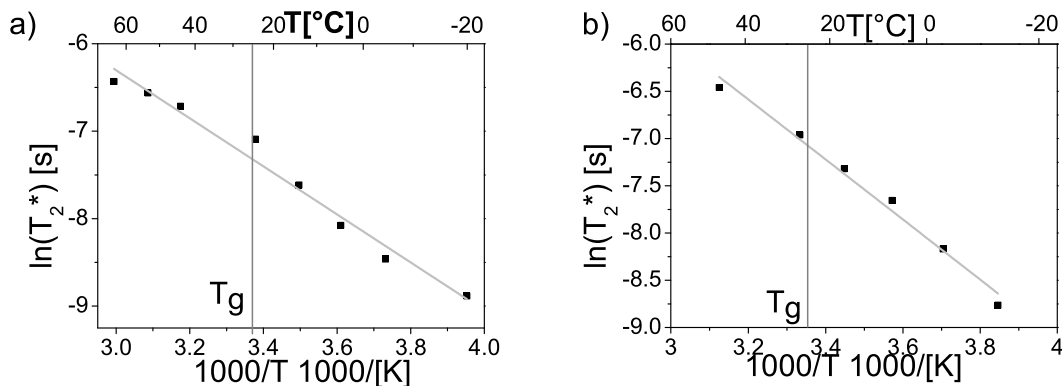


Figure 4.52: The ARRHENIUS plot shows the change in line width against the inverse temperature. From the slope the E_A is extracted shown for a) PE9-PA and b) PE21-PA.

conductivity is decreased due to the dilution of the PA in the polymer. The E_A on the other hand, stays rather constant suggesting that the proton hopping might be due to inter chain interactions [LEE 07].

Additionally, one can reveal information about the overall motion of the polymer by comparing VT ^1H with the ^{31}P MAS NMR measurements. If the ^{31}P MAS NMR signal is not affected by the temperature shift there is no increased chain motion. This in turn would mean that a narrowing of the proton corresponding signal is based on local increase of motion. In the case of the ^{31}P MAS NMR spectra two types of motional processes can lead to line narrowing due to reorientation of PA groups or hopping of acidic protons. The latter averages the dipolar coupling between ^{31}P and ^1H and probing this interaction. Lee et al. found evidence that the fast dynamics is most likely based on acidic protons hopping in PVPA [LEE 07]. Figure 4.51b shows ^{31}P MAS NMR for four different temperatures: below T_g (-25°C and 24°C) and above T_g (43°C and 63°C). In the observed temperature range a significant line narrowing of the ^{31}P signal is found, both below and above T_g . Consequently, this shows that in the same temperature range, compared to the analyzed proton signal narrowing, the phosphorous signal does show a similar behavior. Therefore, the activation energy might not exclusively be assigned to fast dynamic proton motion.

Supporting the assumption of cluster formation a single signal at 32 ppm is observed in the ^{31}P NMR spectrum of PE9-PA at 63°C . This may be attributed to a small

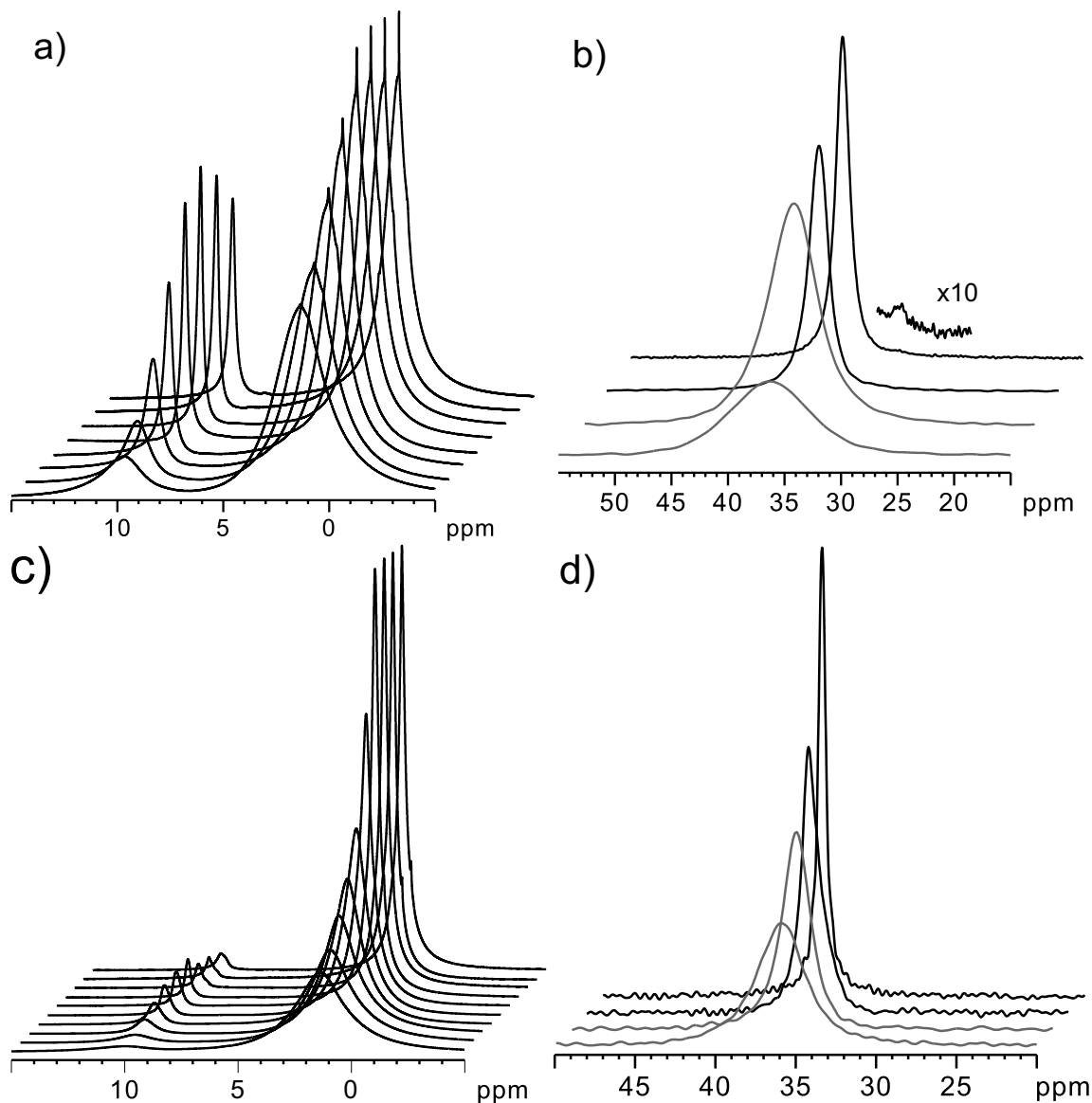


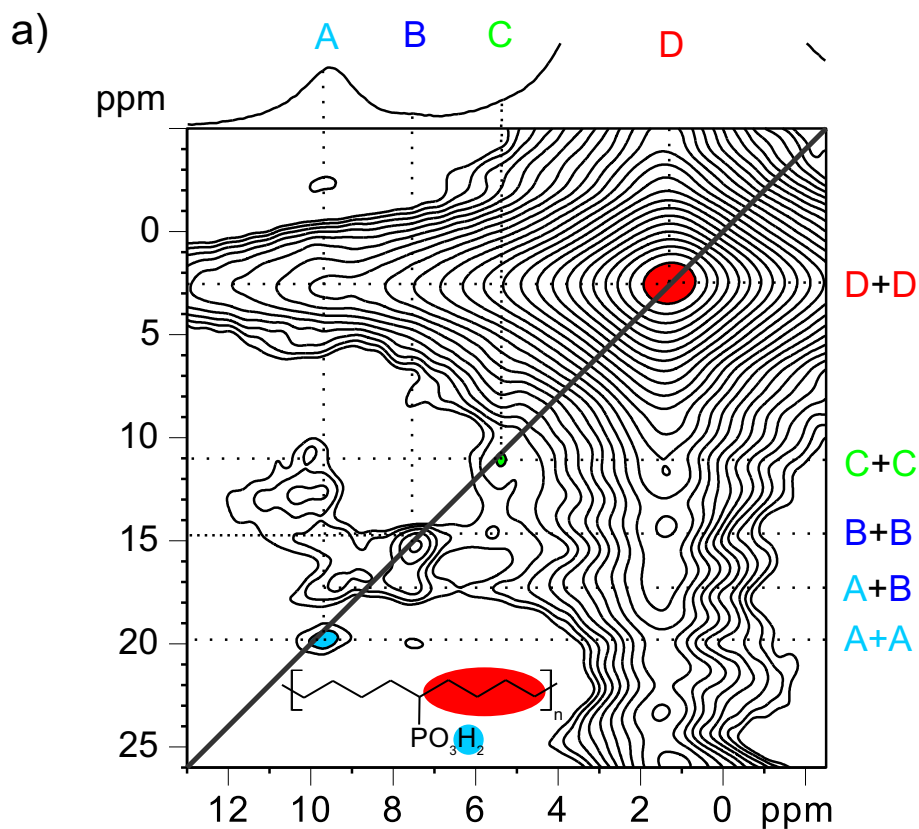
Figure 4.53: Variable temperature experiment for PV9-PA a,b and PV21-PA c,d

- a) ^1H MAS NMR spectra at 30 kHz spinning (850.1 MHz, 19.9 T) starting from the bottom at 13 towards 63°C in steps of 10°C.
- b) ^{31}P MAS NMR spectra at 20 kHz spinning (202.5 MHz, 11.4 T) starting from the bottom at 4 and 24°C (dark grey) until 43 and 63°C (black).
- c) ^1H MAS NMR spectra at 30 kHz spinning (700.1 MHz, 16.4 T) starting from the bottom at 23 towards 63°C in steps of 10°C.
- d) ^{31}P MAS NMR spectra at 20 kHz spinning (202.5 MHz, 11.4 T) starting from the bottom at -25 and 24°C (dark grey), 43 and 63°C (black).

amount of anhydride (0.4%) which could not be anticipated as the dilution is already quite high compared to PVPA. Moreover, PE21-PA does not show this signal supporting the dilution argument. The term "cluster formation" as it is used in this work describes the hydrophilic attempt of the PA groups to arrange close to each other.

Since PE9-PA and PE21-PA show similar line narrowing behavior in the proton spectrum, it seems that the spacer in the chain does not have a significant influence on the E_A . This may be explained in two different ways. Either the determined E_A does not describe the proton hopping or the polymer forms phosphoric acid clusters which enable an internal hopping. Due to the conductivity data discussed above the last assumption seems to be much more probable. A possible formation of a cluster might be similar to that in PE with regularly spaced carboxylic acid side groups [BAUGHMAN 07].

In this model, two PA groups would array face-to-face. This formation could be supported by the $^1\text{H} - ^1\text{H}$ DQF MAS NMR 2D spectrum of PE9-PA at low temperature,



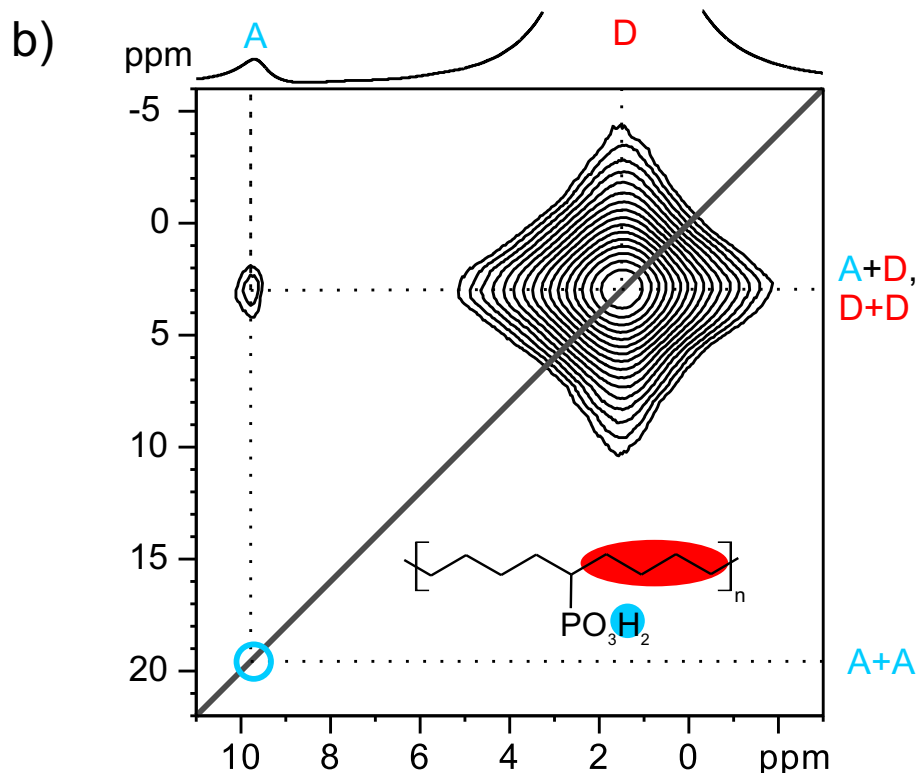


Figure 4.54: $^1\text{H}-^1\text{H}$ DQ-SQ MAS NMR 2D spectrum recorded at 29762 Hz spinning (700.1 MHz, 16.4 T). PE9-PA at a) -15°C and b) 51°C acquired under the following experimental conditions: $\tau_{(\text{exc.})} = 33.6\mu\text{s}$, 2048 t1 increments in the indirect dimension at steps of $16.8\mu\text{s}$, relaxation delay 4 s, 224 transients per increment. Twelve positive contour levels between 0.7% (5.4%) and 96.6% (82.7%) of the maximum peak intensity were plotted. The projection in the direct dimension is shown on the top.

see Figure 4.54a. It shows not only cross peaks between the aliphatic backbone and the PA protons as expected but also include an auto peak of the PA protons. Actually, this spectrum might even reveal three autocorrelation peaks which has not been correlated with different sites yet. The presence of these sites indicates that they are located in different surroundings. X-Ray diffraction might be a starting point for further clarification. While PE9-PA shows these three signals and the auto peak they cannot be found in PE21-PA, as illustrated in Figure 4.55. This is an indication that due to dilution of PA the formation of clusters is not in the detectable range 4.54b.

In addition, the ^{31}P MAS NMR spectrum of PE9-PA shows a resonance with a line width

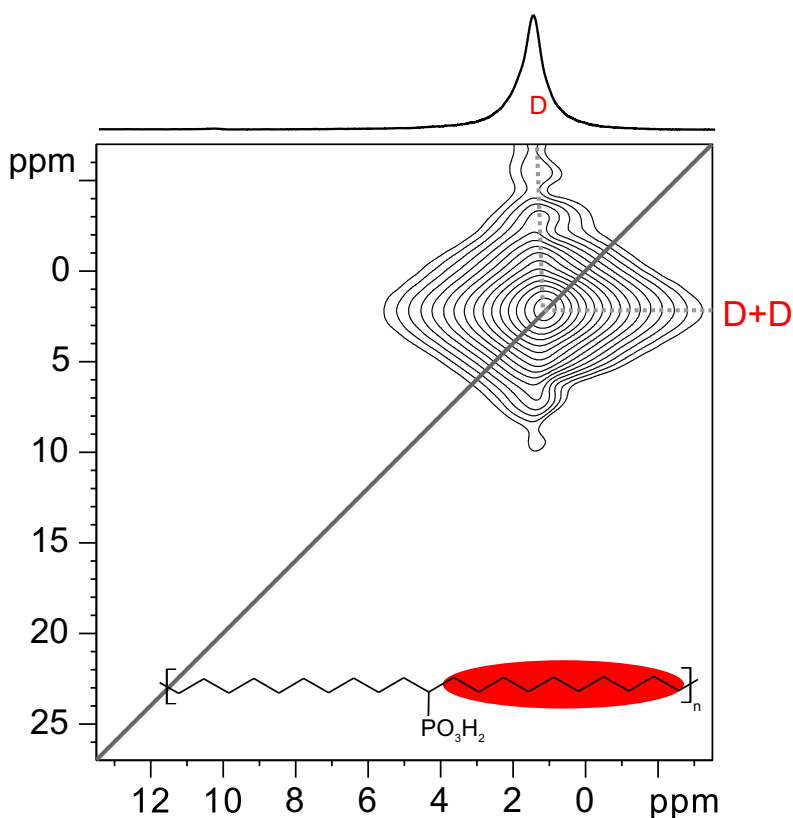


Figure 4.55: $^1\text{H} - ^1\text{H}$ DQ-SQ MAS NMR 2D spectrum recorded at 29762 Hz spinning (850.1 MHz, 19.9 T) of PE21-PA at -15°C acquired under the following experimental conditions: $\tau_{(\text{exc.})} = 33.6\mu\text{ s}$, 2048 t1 increments in the indirect dimension at steps of $16.8\mu\text{ s}$, relaxation delay 4 s, 224 transients per increment. Sixteen positive contour levels between 1.6% and 85.1% of the maximum peak intensity were plotted. The projection in the direct dimension is shown on the top.

of 1050 Hz comparable to that of PVPA with 900 Hz, both recorded at 20°C . This is a further indication that the PE9-PA behaves similarly to PVPA. PE21-PA in contrast has a line width of less than half of it, as shown in Figure 4.51. Again this might be interpreted by the statistical argument of dilution. In contrast to the similarities mentioned, the ^{31}P chemical shift of both samples, PE9-PA and PE21-PA, compared to PVPA is shifted 3 ppm to higher ppm values, see Figure 4.51b. Notably, it is almost identical chemical shift observed in liquid and solid-state ^{31}P MAS NMR spectra, which is not a common observation. In the solid-state ^{31}P MAS NMR spectra presented in chapter 3.1 the

samples showed a shift of about +10 ppm with respect to the liquid state NMR signals [HARRIS 89]. This is a further indication that the spacer *dilutes* the PA in PE.

4.7 Conclusions

The structures of PVBPA-P4VP acid-base copolymer complexes have been studied by various solid-state MAS NMR techniques at different humidity and temperature conditions. Therefore, ^1H and ^{31}P were measured and analyzed. The characterized acid/base copolymer electrolytes provide a new design for achieving proton conductivity. The anhydrous proton conductivities of the copolymers are very low. A minimum is reached at a 1:1 molar ratio of proton donors and acceptor groups in the copolymer. This is at the same time the maximum value of activation energy (E_A) at a 1:1 molar ratio of proton donors and acceptor groups and explains the minimum conductivity. The idea of essentially water free environments at elevated temperatures has to be reviewed since the data show mainly a water dependency. Exposing the sample to controlled relative humidity shows that even small amounts of water in these copolymers can significantly increase the proton conductivity. This is explained by both the increase of the PA mobility and enhancement of the charge carrier density in the polymers due to the water. This has been observed for PVPA where one water molecule is enough to increase the bulk proton conductivity by several orders of magnitude [KALTBEITZEL 07]. Here, the results suggest, that the water acts as intermediate to the PA for the proton transport.

Furthermore, it was outlined how spacers, inserted between protogenic groups in the backbone of a polymer influence the proton conductivity. The information was revealed by applying solid-state NMR methods, such as single-pulse ^1H , ^{13}C , ^{31}P as well as 2D ^1H - ^1H DQ-SQ spectroscopy. The spatial proximity of the acid groups in the polymer was monitored by 2D ^1H - ^1H DQ-SQ NMR. It was found that the dilution in this case decreases the conductivity as expected. Nevertheless, the diluted systems show similar activation energies in both VT ^1H MAS NMR and impedance spectroscopy. Thus, these results suggest that in diluted systems the proton motion is still present with comparable activation energies. Since they form phosphonic acid clusters, this motion is localized and therefore does not contribute to the bulk conductivity.

Chapter 5

Summary

In this work, new proton conducting materials have been characterized in terms of their structure and dynamics using solid-state nuclear magnetic resonance (NMR) spectroscopy and X-ray diffraction. Different structural properties have been analyzed systematically on various materials containing phosphonic acid (PA) as the protogenic group. It is known that the amphoteric character of phosphonic acid enhances the proton conductivity. Therefore, samples possibly suitable as membranes in high-temperature operation of fuel cells ($T > 100^\circ\text{C}$) have been evaluated. Various solid-state NMR methods have been applied to elucidate both the molecular structure and to reveal the mechanism of observable bulk proton conductivity. For this purpose, ^1H and ^{31}P magic angle spinning (MAS) NMR methods have been particularly useful and have provided insight into local connectivities and hydrogen bonding networks. Packing arrangements have been identified by means of heteronuclear dipolar recoupling techniques. In addition, the dynamics of the protogenic PA units have been probed by ^2H MAS NMR.

Ionomers

The central part of this work is devoted to low molecular weight aromatic compounds, containing several units of PA, hence, are called ionomers. Six different geometrical shapes: LINE, TRIANGLE, SCREW, TETRAHEDRON, SQUARE, and HEXAGON, rather crystalline compounds, have been investigated, as shown in Figure 5.1a.

Under dry conditions, both the number and the density of PA in a molecule can affect the bulk proton conductivity by orders of magnitude. By applying humid conditions, however, the number and density of PA is not decisive. The HEXAGON was identified as the most promising geometrical shape with high-temperature bulk proton conductivities in the range of 10^{-3} S/cm. However, impedance spectroscopy, ^1H , ^2H , and ^{31}P MAS NMR data suggest a proton transport assisted by the presence of incorporated water. Additionally, ^{31}P MAS NMR spectra combined with thermal gravimetric analysis connected with mass spectrometer (TGA-MS) data provides the amount of approximately 0.7 incorporated water molecules per PA. Notably, the bulk proton conductivity of the HEXAGON is almost constant at high-temperatures indicating a complex mechanism of proton transport different from a simple vehicle mechanism observed for state-of-the-art membranes, such as Nafion[®].

Thus, the question arises why some geometrical structures lead to better conductivity than others, even though they contain similar chemical moieties. Hence, the current investigation involved the impact of the crystal structure. Notably, structural information from both the TETRAHEDRON and HEXAGON have been obtained. The phosphonic acids of the TETRAHEDRON form tetrameric clusters isolating the mobile protons while the phosphonic acids in the HEXAGON form zigzag-type pathways through the sample, that are connected by water molecules.

Furthermore, a detailed analysis of variable temperature ^1H MAS NMR experiments and several types of ^{31}P MAS NMR methods have been conducted. They revealed the presence of different phosphonic acid sites present in the ionomers. These different sites might be due to different PA-water interactions and explain why the activation energy as observed by NMR is smaller compared to that obtained from impedance spectroscopy. The presented low molecular weight organic crystals are promising materials for polyelectrolyte membranes in the case of automotive applications since they facilitate hydrogen bonding mediated proton conduction, even at high temperature. The structure of the hydrogen bonded networks, however, is very complex.

Acid-base concept

The second part of this work demonstrates how acid-base pairing and the choice of appropriate spacers may influence proton conduction. To investigate this properly, different ratios of the statistical copolymer poly(vinylphosphonic acid) and poly(4-vinylpyridine) (PVBPA-P4VP) have been prepared and characterized, as depicted in Figure 5.1b. Solid-state ^1H and ^{31}P MAS NMR have been measured to reveal information about the local structure and chemical changes. While the anhydrous proton conductivities of all statistical copolymers are rather poor, the conductivity increases to a level of 10^{-2} S/cm when exposing the sample to humidity. Unlike previously found for poly(vinylphosphonic acid) (PVPA), anhydride formation in PVBPA-P4VP at elevated temperature is not reversible even when exposing the sample to a relative humidity of 100%. At the expense of proton conductivity, the anhydride formation is decreased by diluting the phosphonic acid amount. A minimum of proton conductivity and maximum of apparent activation energy of proton motion is reached at an acid-base molar ratio of 1:1. This, indicates that the chosen acid base combination forms a stable salt which most likely inhibits bulk proton conductivity. All copolymers revealed a fairly high bulk proton conductivity at higher levels of water content. However, bulk proton conduction in essentially water free environments at elevated temperatures in this system is apparently not feasible via this approval.

Spacer concept

In the third class of systems the influence of a *spacer* on bulk conductivity and degree of backbone crystallinity was investigated. Spacer can have two main effects in the system. They can increase the local mobility, and via dilution prevent unwanted condensation of the PA groups. Unlike in systems such as poly benzimidazole (PBI), spacers have been inserted between the protogenic groups along the backbone as shown in Figure 5.1c. Solid-state NMR methods, such as ^1H , ^{13}C , ^{31}P and single quantum as well as 1 and 2D ^1H double quantum spectroscopy, revealed information about the backbone crystallinity and spatial proximity of phosphonic acid groups. As expected that dilution of the protogenic groups decreases the conductivity. Nevertheless, the diluted systems exhibit similar apparent activation energies for local motions in both the

variable temperature ^1H MAS NMR and impedance spectroscopy compared to PVPA. These observations suggest the formation of phosphonic acid clusters with high local motion, while this motion does not contribute to the bulk proton conductivity. Additionally, it was shown that gradual changes of the spacer length lead to different morphologies.

Conclusion and Outlook

In summary, combining solid-state NMR techniques like ^1H , ^2H and ^{31}P MAS NMR with X-ray analysis and thermometric measurements, structural and dynamic phenomena in proton conducting materials have been identified on the molecular level. These methods are suitable to prove and develop structural models on the molecular level and monitor hydrogen bond formation, condensation, and structural stability. The results have been discussed with respect to different proton conduction mechanisms and may contribute to a more rational design and allow tailoring of proton conducting membranes. Relating the findings reported here with previous studies of systems with PA groups a scenario emerges, where disorder in the lattice and the incorporation of water in the structure lends to particularly promising proton conduction.

Along these lines future work may incorporate ionomers into a polymer matrix to improve the mechanical properties. Here, the question would be if e.g. the HEXAGON would orientate its aromatic moieties to allow hydrogen bonded networks, as in PVPA or the diluted forms PE9-PA. Another approach might be to increase the number of PA in an ionomer based on a dendritic approach, e.g. using the SCREW geometrical shape.

Appendix A

Additional spectra

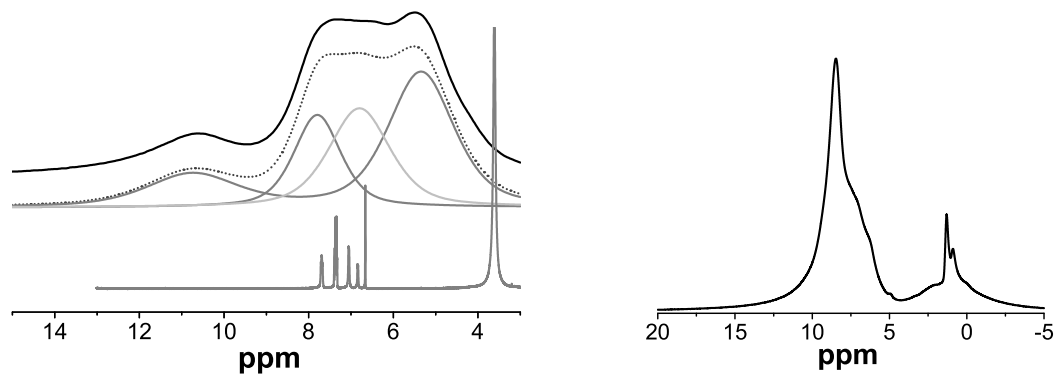


Figure A.1: ^1H solid-state MAS NMR spectra recorded at 30 kHz spinning (700.1 MHz, 16.4 T) is shown on the top, below the deconvoluted peaks are plotted and at the bottom the liquid spectra in DMSO at 100°C (500.2 MHz, 11.7 T) can be seen for a) SCREW b) TETRAHEDRON

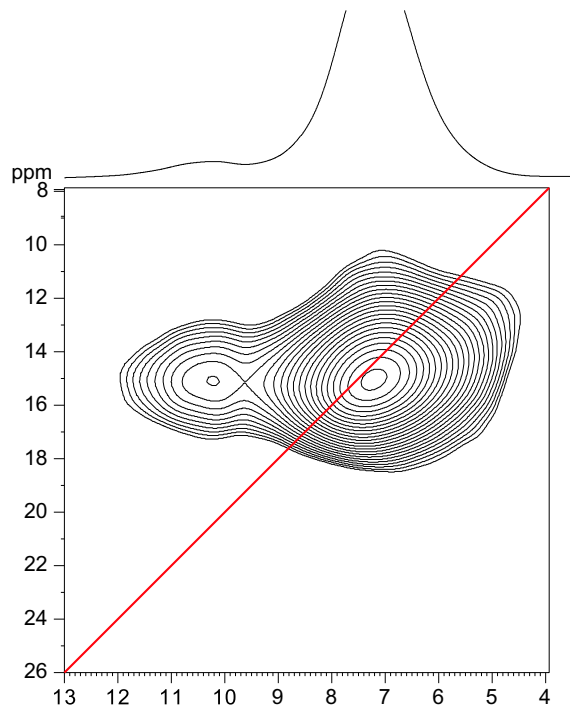


Figure A.2: 2D ${}^1\text{H}$ - ${}^1\text{H}$ MAS NMR DQ-SQ correlation spectra using spinning frequency of 29762 Hz (700.1 MHz, 16.4 T) of the HEXAGON recorded at -15°C and acquired under the following experimental conditions: $\tau_{(\text{exc.})} = 33.6\mu\text{s}$, 2048 t1 increments in the indirect dimension for a time step of $16.8\mu\text{s}$, a relaxation delay of 10 s, and 148 transients per increment. Sixteen positive contour levels are shown between 1% and 95% of the maximum peak intensity are plotted. The projection of the direct dimension is shown on the top.

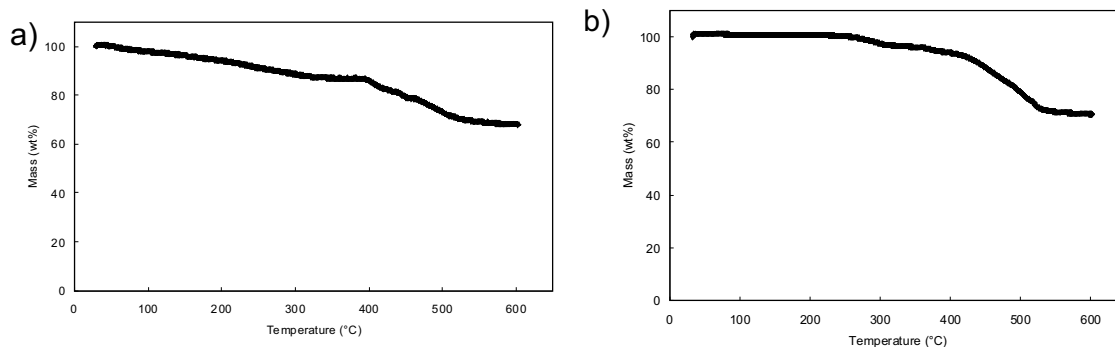


Figure A.3: TGA measurement of the a) SQUARE and the b) SCREW.

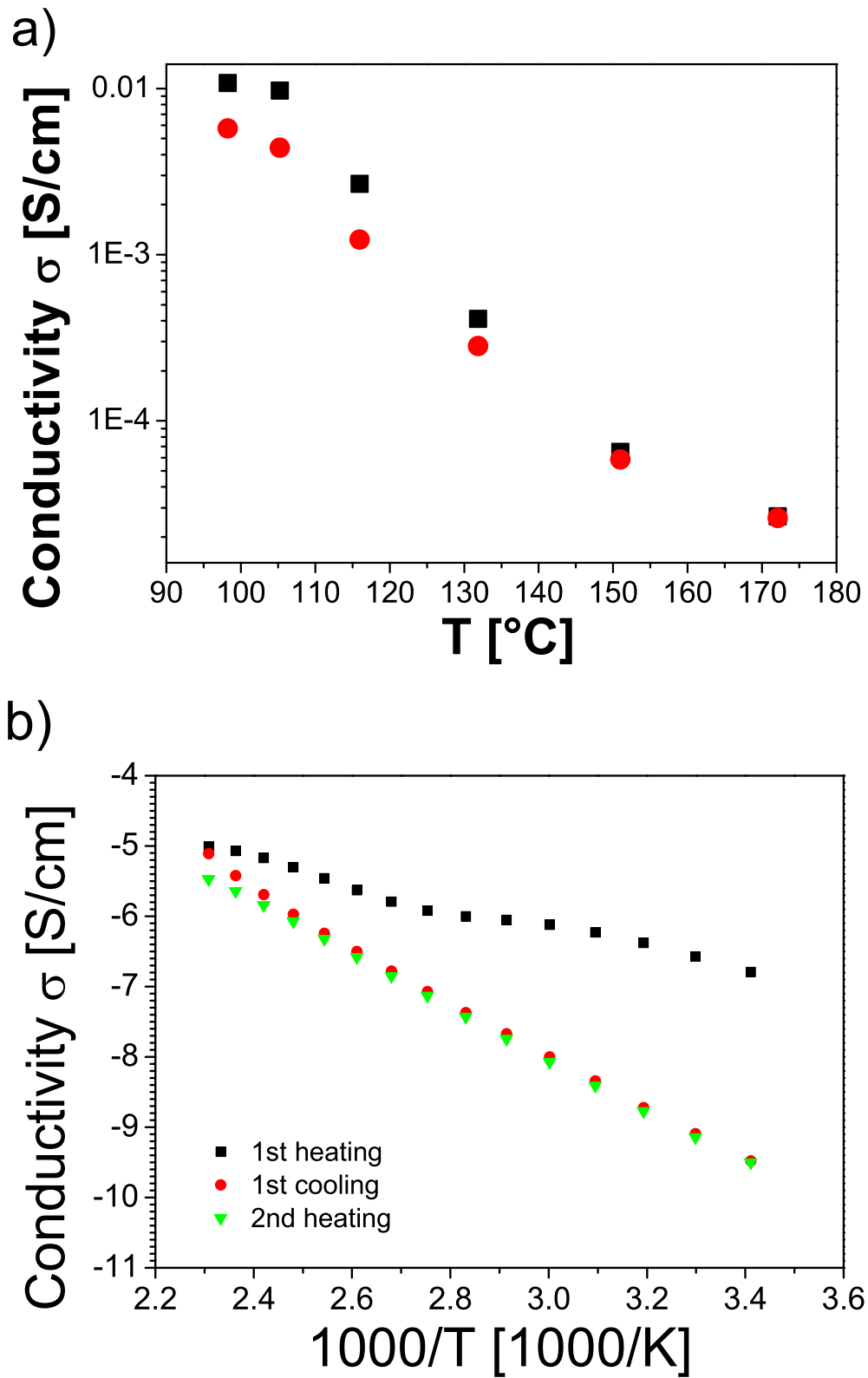


Figure A.4: Conductivity measurements of the SQUARE at a) humid and b) dry conditions.

Appendix B

Methods

Solid State NMR

The ^1H MAS NMR experiments were performed either on a Bruker Avance 700 or Avance-III 850 spectrometer, equipped with a 2.5 mm fast MAS probe. All ^1H MAS NMR spectra were acquired at spinning frequencies of 30 kHz, whereas double quantum requires a rotation of 29762 Hz. ^{31}P MAS NMR experiments were carried out at an operating frequency of 202.5 MHz on a Bruker ASX500 spectrometer, equipped with a 2.5 mm fast MAS probe. The spinning frequencies were either 15 kHz or 20 kHz. ^{13}C CP MAS NMR spectra were acquired at an operating frequency of 125.8 MHz or 213.8 MHz on a Bruker ASX500 or Avance-III 850MHz spectrometer, respectively. Unless stated otherwise, all spectra were collected at room temperature, which leads to a sample temperature up to 40-50°C due to the frictional heat at high spinning frequency. Other temperatures were calculated with the formula in equation B.1.

$$T[K]_{\text{real}} = -12.1 + 1.019 * T[K]_{\text{display}} + 0.62 * \omega_R - 0.0023 * T[K]_{\text{display}} * \omega_R + 0.0364 * \omega_R^2 \quad (\text{B.1})$$

^1H , ^2H , ^{13}C and ^{31}P static and MAS NMR experiments were carried out on Bruker spectrometer as listed in table B.1. In solid-state NMR external references are used to calibrate the chemical shift value.

Each nucleus has commonly used substances with known chemical shifts as listed in table B.2. Three different sizes of rotors were used, 2.5 and 4 mm depending on the kind of experiment. ^1H and double quantum filtered (DQF) NMR spectra were recorded either at 700.1 or 850.1 MHz at a spinning speed of 30 kHz or 29762 Hz respectively. ^2H MAS spectra and static at 107.5 MHz for slow spinning speed at 7 kHz and fast at 20 kHz ^{13}C CP MAS at 125.8 and REPT-HDOR at 213.8 with a spinning speed at 25 kHz. ^{31}P MAS spectra mainly at 202.5 MHz rotating at 20 kHz and static at 121.5 MHz.

ω_L	$\omega(^1\text{H})$	$\omega(^2\text{H})$	$\omega(^{13}\text{C})$	$\omega(^{31}\text{P})$
console				
AV	300.1	46.0	75.5	121.5
ASX	500.1	76.8	125.8	202.5
Avance-I	700.1	107.5	176.1	283.4
Avance-III	850.1	130.5	213.8	344.1

Table B.1: Lamor frequencies for measured nuclei at different spectrometer

nucleus	substance	Reference peak [ppm]	Literature
^1H	TTSS	0.27	MUNTEAN88
^2H	DMS	3.15	HESSE95
^{13}C	Adamantane	29.456	MORKOMBE03
^{31}P MAS	$\text{CaHPO}_4 \cdot 2\text{H}_2\text{O}$	1.4	AUE84
^{31}P static	85% H_3PO_4	0	HESSE95

Table B.2: Reference substances for solid-state NMR spectroscopy

Impedance Spectroscopy

Bulk proton conductivity under defined relative humidity were provided by Anke Kaltbeitzel. Using dielectric spectroscopy covering a frequency range of 10^{-1} to 10^{-6} Hz aligned in a two-electrode geometry and equipped with an SI 1260 impedance/gain-phase analyzer. Proton conductivity depends drastically on the relative humidity (RH) during the measurement. Complete dry measurements were provided after heating the sample under vacuum at 50°C for 4 days. The control of the RH during the measurement was obtained by mixing dry nitrogen with humidity saturated nitrogen and controlled using a Sensiron SHT15 sensor.

For the measurement the samples were pressed to tablets and attached via an E-tek(R) contact to a stainless steel electrodes. Evaluation was done by a BODE plot where conductivity [$\text{S} \cdot \text{cm}^{-1}$] is plotted against frequency [Hz]. Each measurement shows a plateau where the AC conductivity is independent of the frequency. This value extrapolated against $\omega = 0$ which defines the DC conductivity. This showed the same results as obtained by a COLE-COLE plot [COLE 41] which double checks this method. The same analyzer was used for the measurements under dry conditions. This pellets were placed on a gold electrode. The temperature program was set to 10 minutes for the heating and 10 minutes for measuring and it was controlled using dry nitrogen gas. This measurements were provided from Christoph Siebert.

Thermal Gravimetric Analysis TGA

Thermal gravimetric analysis was performed on a TGA/SDTA851 (METTLER TOLEDO) under nitrogen with a heating rate of K/min. The mass spectrometer was set to detect one single molecular weight e.g. 18 g/mol for water. The samples were dried in advance for at least two days in a vacuum oven at 50°C.

Differential Scanning Calorimetric DSC

DSC was performed on a DSC 822 (METTLER TOLEDO) under N₂ with a heating rate of 10 K/min.

Car-Parrinello molecular dynamics

For calculation, a simplified model systems, based on the mentioned X-ray data was built representing several different local packing arrangements. The models were designed for *ab initio* calculations under periodic boundary conditions. This limits the amount of disorder which can be incorporated due to high computational times. We used *ab initio* Car-Parrinello molecular dynamics (CPMD) simulations at a temperatures of -20, 30, 80, and 130°C. Properties required for the calculation of NMR chemical shifts and NICS maps can be computed efficiently in reciprocal space (G space). The fast Fourier transform techniques is used to switch to direct space and vice versa. The BLYP exchange and correlation functional and Goedecker-Teter-Hutter pseudo potentials with the dispersion correction for carbon atoms were used together with a plane-wave cutoff of 70 Ry for all atoms. Large supercells, typically 20 Å x 20 Å x 20 Å or larger, were used to isolate the molecules from their periodic image and to avoid overlay of the NICS fields. Therefore, the NICS maps can be considered to be correct everywhere except at positions closer than about 0.5 Å to heavy atoms. Notably, the time scale reached with the *ab initio* simulations was in the order of ps. Possible conformational fluctuations, however, might have characteristic times of ms or longer. Thus, the CPMD simulations rather yielded a sampling of the local phase space point at which the system was initially prepared. In order to learn about the spectroscopic signatures of the packing motifs full trajectories were sampled with calculations of NMR resonances. For this purpose, 15 snapshots at random times within the trajectory were taken. In addition to the average chemical shifts of the protons and carbon atoms, their standard deviations have been computed. This makes it possible to characterize the strength of the effect of small geometric fluctuations on the distribution of NMR chemical shifts.

Appendix C

Pulse program

Single-Pulse Experiment

```
#include <Avance.incl>
1 ze 2 d1 pl1:f1 3 p1 ph1
go=2 ph31
wr #0
exit
ph0=0
ph1=0 1 2 3
ph31=0 1 2 3
```

Solid Echo

```
10u pl1:f1 1 ze 2 d1 3 1u
(p1 ph1):f1
d6
(p1 ph2):f1
d7
go=2 ph31
wr #0
exit
ph0 = 0
ph1 = 0 3 2 1 0 3 2 1
```

```
ph2 = 3 2 1 0 1 0 3 2
ph31= 3 2 1 0 3 2 1 0
```

CP-Solid Echo

```
;high power cross polarization sequence
;using two proton power levels for CP and decou-
pling
#include <Avance.incl>
;"d3=d2+p11*0.5-de+dw*0.5-4u"
```

```
1 ze 2 d1 do:f2
1m pl1:f1 pl2:f2
(p2 ph1):f2
2u
(p15 ph2):f1 (p15 ph3):f2
d2 pl11:f1
(p11 ph4):f1
d3
2u pl12:f2
2u cpd2:f2
go=2 ph31
2u do:f2
wr #0
exit
```

```
ph1 = 1 3
ph2 = 0 0 1 1 2 2 3 3
ph3 = 0
ph4 = 0 2 1 3 2 0 3 1 1 3 2 0 3 1 0 2 2 0 3 1 0 2 1 3 3
1 0 2 1 3 2 0
ph31= 0 2 1 3 2 0 3 1 2 0 3 1 0 2 1 3
```

CP-RAMP

```
#include <Avance.incl>
1 ze 2 d1 do:f2
3u pl1:f1
3u pl22:f2
```

```
(p3 ph1):f2
2u pl2:f2
(p15:sp0 ph2):f1 (p15 ph3):f2
4u
;2u pl11:f1 ;additional X pulse
;(p1 ph4):f1 ;for adjustment
2u pl12:f2
2u cpd2:f2
go=2 ph31
2u do:f2
wr #0
exit
ph1 = 1 3
ph2 = 0 0 1 1 2 2 3 3
ph3 = 0
ph4 = 1 1 2 2 3 3 0 0
ph31= 0 2 1 3 2 0 3 1
```

BaBa presaturated 1tR.1d

```
;ns=16*n
#include <Avance.incl>
"d3=1s/(2*cnst31)-2*p1"
;d7: z-filter ;p1: 90 pulse ;pl1: proton power
1 ze
1m pl1:f1
2 (p1 ph20):f1 ;saturation comb
13m
(p1 ph21):f1
7m
(p1 ph22):f1
1m
(p1 ph23):f1
3m
lo to 2 times 8
d1
3 p1 ph0 ;exc.
d3
p1 ph2
p1 ph1
```

```
d3
p1 ph3
d0 ;t1
4 p1 ph10 ;rec.
d3
p1 ph12
p1 ph11
d3
p1 ph13
d7 ;z-filter
p1 ph31
go=2 ph30
wr #0
exit ph0 = (8) 0 2 4 6
ph1 = (8) 2 4 6 0
ph2 = (8) 4 6 0 2
ph3 = (8) 6 0 2 4
ph10= 0
ph11= 1
ph12= 2
ph13= 3
ph30= 0 2 0 2 2 0 2 0 1 3 1 3 3 1 3 1
ph31= 0 0 0 0 2 2 2 2 1 1 1 1 3 3 3 3
ph20= 0 1 2 3
ph21= 1 2 3 0
ph22= 2 3 0 1
ph23= 3 0 1 2
```

BaBa presaturated 1tR.2d

```
;ns=16*n ;MC2=States-TPPI
#include <Avance.incl>
"d3=1s/2*cnst31-2*p1"
;cnst31: spinning rate ;p1: high-power pi/2 pulse
;p11: proton power ;d7: z-filter
define loopcounter nfid "nfid=td1/2" ;compute number of t1 increments
1 ze
10u pl1:f1
2 (p1 ph20):f1 ;saturation comb
```

```

13m
(p1 ph21):f1
7m
(p1 ph22):f1
1m
(p1 ph23):f1
3m
lo to 2 times 8
d1
3 p1 ph0 ;exc.
d3
p1 ph2
p1 ph1
d3
p1 ph3
d0 ;t1
4 p1 ph10 ;rec.
d3
p1 ph12
p1 ph11
d3
p1 ph13
d7
p1 ph31
go=2 ph30
10m wr #0 if #0 zd
1m ip0
1m ip1
1m ip2
1m ip3
lo to 2 times 2
1m id0
lo to 2 times nfid
exit
ph0 = (8) 0 2 4 6
ph1 = (8) 2 4 6 0
ph2 = (8) 4 6 0 2
ph3 = (8) 6 0 2 4
ph10= 0
ph11= 1

```

```

ph12= 2
ph13= 3
ph30= 0 2 0 2 2 0 2 0 1 3 1 3 3 1 3 1
ph31= 0 0 0 0 2 2 2 2 1 1 1 1 3 3 3 3
ph20= 0 1 2 3
ph21= 1 2 3 0
ph22= 2 3 0 1
ph23= 3 0 1 2

```

REPT-HSQC.1d

```

#include <Avance.incl>
"p2=p1*2" "d4=1s/(cnst31*2)-p1*2" "d11=1s/(cnst31*2)-
p1*1.5"
"d12=1s/(cnst31*2)-p1*2.5" ;"d0=1s*110/(cnst31)"
; 110 neq 0 -> gated HDOR
1 ze
2 d1 do:f2
10u p11:f1 p12:f2
3 (p1 ph20):f1 ; saturate carbons ...
9m
(p1 ph21):f1
7m
(p1 ph22):f1
1m
(p1 ph23):f1
2.5m
lo to 3 times 4
d5 ; dephase
(p1 ph1):f2 ; excitation
d4
4 (p2 ph6):f1
d4
(p2 ph7):f1
d4
lo to 4 times 11
5 (p2 ph6):f1
d4
lo to 5 times 10
(p2 ph8):f2

```

```

6 d4
(p2 ph6):f1
d4
(p2 ph7):f1
lo to 6 times l1
7 d4
(p2 ph6):f1
lo to 7 times l0
d12
(d0 p1 ph2):f1 (p1 ph3):f2 ; INEPT-transfer
d11
8 (p2 ph6):f2
d4
(p2 ph7):f2
d4
lo to 8 times l2
9 (p2 ph6):f2
d4
lo to 9 times l0
(p2 ph9):f1
d4
10 (p2 ph6):f2
d4
(p2 ph7):f2
d4
lo to 10 times l2
11 (p2 ph6):f2
d4
lo to 11 times l0
(p1 ph4):f1 ; end rec.
d6 pl12:f2 ; set dec. power and dephase;
2u cw:f2
2u cpd2:f2
(p1 ph5):f1 ; read out
go=2 ph31 ; acquire
2m do:f2
30m wr #0
exit
ph1= 0 2 1 3 2 0 3 1 2 0 3 1 0 2 1 3
ph2= 1 3 2 0 3 1 0 2

```

```

ph3= 1 1 2 2 3 3 0 0
ph4= 2 2 3 3 0 0 1 1
ph5 = 0 0 1 1 2 2 3 3 2 2 3 3 0 0 1 1
ph6= 0
ph7= 1
ph8= 1 3 2 0 3 1 0 2 ; central 1H rcpl.refocus
ph9= 2 0 3 1 0 2 1 3 ; central 13C rcpl.refocus
;ph31= 1 1 0 0 3 3 2 2
ph31= 1 1 2 2 3 3 0 0
ph20= 0 1 2 3
ph21= 1 2 3 0
ph22= 2 3 0 1
ph23= 3 0 1 2

```

REPT-HSQC.2d

```

#include <Avance.incl>
''p2 = p1 * 2''''d4 = (0.5s/cnst31) - p1 * 2''
l31 = nuR/10(16Bit - Limit for loop counters)
''d11 = (0.5s/cnst31) - p1 * 1.5''
''l1 = (l5 - 1)/2''''l2 = l1''''l0 = l5 - 1 - l1 * 2''
;l0 : REDOR recoupling time = tr*(2*L1+L0+1)
;l1 : REDOR recoupling time = tr*(2*L1+L0+1)
;l2 : for most cases L2 = L1 unless assymmetric transfer
;l5 : REDOR recoupling time in tr > 0 !!
1 ze 2 d1 do:f2
;1u fq=cnst22:f2
10u pl1:f1 pl2:f2
3 (p1 ph20):f1 ; saturate carbons ...
13m
(p1 ph21):f1
7m
(p1 ph22):f1
1m
(p1 ph23):f1
3m
lo to 3 times 4
d5 ; dephase
(p1 ph1):f2 ; excitation

```



```

d4
4 (p2 ph6):f1 ;  $t_{exc}(L1) = 2 * t_{Rotor} * (L1 + 1)$ 
d4
(p2 ph7):f1
d4
lo to 4 times l1
5 (p2 ph6):f1
d4
lo to 5 times l0
(p2 ph8):f2
6 d4
(p2 ph6):f1
d4
(p2 ph7):f1
lo to 6 times l1
7 d4
(p2 ph6):f1
lo to 7 times l0
d11 ; end excitation
d0 ; t1
(p1 ph2):f1 (p1 ph3):f2 ; reconversion
d11
8 (p2 ph6):f2 ;  $t_{rec}(L1) = t_{exc}(L1)$ 
d4
(p2 ph7):f2
d4
lo to 8 times l2
9 (p2 ph6):f2
d4
lo to 9 times l0
(p2 ph9):f1
d4
10 (p2 ph6):f2
d4
(p2 ph7):f2
d4
lo to 10 times l2
11 (p2 ph6):f2
d4
lo to 11 times l0

```

```

(p1 ph4):f1 ; end rec.
d6 pl12:f2 ; set dec. power and dephase
(p1 ph5):f1 ; read out
go=2 ph31 cpd2:f2 ; acquire
2m do:f2
30m wr #0 if #0 zd
1m id0 ; inc. t1
1m ip3 ; TPPI
lo to 2 times td1
exit
ph1= 0 2 1 3 2 0 3 1 2 0 3 1 0 2 1 3
ph2= 1 3 2 0 3 1 0 2
ph3= 1 1 2 2 3 3 0 0
ph4= 2 2 3 3 0 0 1 1
ph5 = 0 0 1 1 2 2 3 3 2 2 3 3 0 0 1 1
ph6= 0
ph7= 1
ph8= 1 3 2 0 3 1 0 2 ; central 1H rcpl.refocus
ph9= 2 0 3 1 0 2 1 3 ; central 13C rcpl.refocus
ph31= 1 1 0 0 3 3 2 2
ph31= 1 1 2 2 3 3 0 0
ph20= 0 1 2 3
ph21= 1 2 3 0
ph22= 2 3 0 1
ph23= 3 0 1 2

```

REPT-HDOR

```

#include <Avance.incl> "p2=p1*2" "d4=(0.5s/cnst31)-
p1*2"
;l31 = vR / 10 (16 Bit-Limit for loop counters)
"d11=(0.5s/cnst31)-p1"
"d12=(0.5s/cnst31)-p1*1.5"
"d13=0.5*p1" "l1=(15-1)/2"
"l0=l5-1-l1*2" 1 ze
2 d1 do:f2
;l1u fq=cnst22:f2
10u pl1:f1 pl2:f2
3 (p1 ph20):f1 ; saturate carbons ...
13m

```

```

(p1 ph21):f1
7m
(p1 ph22):f1
1m
(p1 ph23):f1
3m
lo to 3 times 4
d5 ; dephase
(p1 ph1):f2 ; excitation
d11
4 (p2 ph6):f1 ; t exc (L1) = 2 * t Rotor * ( L1 +1)
d4
(p2 ph7):f1
d4
lo to 4 times l1
5 (p2 ph6):f1
d4
lo to 5 times l0
(p2 ph8):f2
6 d4
(p2 ph6):f1
d4
(p2 ph7):f1
lo to 6 times l1
7 d4
(p2 ph6):f1
lo to 7 times l0
d12 ; end excitation
(d0 p1 ph2):f1 (p1 ph3):f2 ; transfer
d12 ; reconversion
8 (p2 ph6):f2 ; t rec (L1) = t exc (L1)
d4
(p2 ph7):f2
d4
lo to 8 times l1
9 (p2 ph6):f2
d4
lo to 9 times l0
(p2 ph9):f1
d4

```

```

10 (p2 ph6):f2
d4
(p2 ph7):f2
d4
lo to 10 times l1
11 (p2 ph6):f2
d4
lo to 11 times l0
d13
(p1 ph4):f1 ; end rec.
d6 pl12:f2 ; set dec. power and dephase
(p1 ph5):f1 ; read out
go=2 ph31 cpd2:f2 ; acquire
2m do:f2
30m wr #0 if #0 zd
1m id0 ; incr t1
lo to 2 times td1
exit

ph1= 0 2 1 3 2 0 3 1 2 0 3 1 0 2 1 3
ph2= 1 3 2 0 3 1 0 2
ph3= 1 1 2 2 3 3 0 0
ph4= 2 2 3 3 0 0 1 1
ph5 = 0 0 1 1 2 2 3 3 2 2 3 3 0 0 1 1
ph6= 0
ph7= 1
ph8= 1 3 2 0 3 1 0 2 ; central 1H rcpl.refocus
ph9= 2 0 3 1 0 2 1 3 ; central 13C rcpl.refocus
ph31= 1 1 2 2 3 3 0 0 ;
sat comb ph20= 0 1 2 3
ph21= 1 2 3 0
ph22= 2 3 0 1
ph23= 3 0 1 2

```

SUPER

```

;without toss. ;recoupling of CSA by 2*360deg
pulses ;1d test version
define loopcounter td1half "l4=0"
; initial t1 (??) "p2=2*p1" "p22=(1s/cnst31)*(1.0/24.24)"

```

```

;pulse for 360deg/2 rotations "td1half=td1/2"      d22
; for STATES cosine/sine                          d22
"d21=(1s/cnst31)*0.2464-1u" ; start position of 1u pl23:f2
4*180deg pulses                                  (p22 ph14):f1 ; 360deg/2 pulse
"d22=(0.5s/cnst31)-4*p22-d21-2u"; rest of tR/2 in (p22 ph15):f1 ; 360deg/2 pulse
CSA recoupling                                   (p22 ph12):f1 ; 360deg/2 pulse
"d25=(1s/cnst31)*0.1226-p1" ; TOSS delays         (p22 ph13):f1 ; 360deg/2 pulse
"d26=(1s/cnst31)*0.0773-2*p1" "d27=(1s/cnst31)*0.2136-pl22:f2
2*p1"                                             d21 pl1:f1 ; finish 1 tR
"d28=(1s/cnst31)*1.0433-2*p1" "d29=(1s/cnst31)*0.7144-3 times l4
p1-d13"                                          p1:f1 ph7 ; store
"in6=(1s/cnst31)/l5" "in0=(1s/cnst31)*0.155"     d6 do:f2 ; z-filter and gamma-integral
"d0=(1s/cnst31)*0.155"                          1u cpd2:f2 ; TPPM decoupling during acq.
1 ze                                             1u pl12:f2
2 d1                                             p1:f1 ph8 ; read out
d0 rpp12 ; reset 2*360deg phase supercycles      d25 ; ...
rpp13                                            p2:f1 ph3
rpp14                                            d26
rpp15                                            p2:f1 ph4
10u pl2:f2 pl3:f1                               d27
3u                                               p2:f1 ph5
p3:f2 ph1 ; 1H 90deg                            d28
3u                                               p2:f1 ph6
#ifdef rampCP                                    d29 ; ... TOSS
(p15:sp0 ph2):f1 (p15 ph10):f2 ; CP              go=2 ph31
2u                                               3m do:f2
#endif #ifndef rampCP                            id6
(p15 ph2):f1 (p15 ph10):f2 ; CP                  lo to 2 times l5 ; gamma-integral
#endif                                             4 dd
2u                                               lo to 4 times l5 ; decrement d6 again
; pl1:f1                                          30m wr #0 if #0 zd
2u cw:f2                                          ip7 ; alternate cosine and sine (STATES)
1u pl22:f2                                        lo to 2 times 2
3 d21 pl21:f1                                    iu4 ; increment t1
1u pl23:f2 ; increase 1H dec. power during pulses ip7 ; skip -cosine
(p22 ph12):f1 ; 360deg/2 pulse                   ip7 ; skip -sine
(p22 ph13):f1 ; 360deg/2 pulse                   lo to 2 times td1half
(p22 ph14):f1 ; 360deg/2 pulse                   exit
(p22 ph15):f1 ; 360deg/2 pulse
1u pl22:f2                                       ph0 = 0 ; reference phase ph1 = 1 3 ;+y -y ; 1H

```

```

90deg
ph2 = 0 0 1 1 2 2 3 3 ;+x +x +y +y -x -x -y -y ; 31P
CP
ph3 = 1 1 2 2 3 3 0 0 ;+y +y -x -x -y -y +x +x ; #1
180deg TOSS
ph4 = 3 3 0 0 1 1 2 2 ;-y -y +x +x +y +y -x -x ; #2
ph5 = 1 1 2 2 3 3 0 0 ;+y +y -x -x -y -y +x +x 3 3 0
0 1 1 2 2 ;-y -y +x +x +y +y -x -x ; #3
ph6 = 2 2 1 1 0 0 3 3 ;-x -x +y +y +x +x -y -y 0 0 3
3 2 2 1 1 ;+x +x -y -y -x -x +y +y ; #4
ph7 = 1 1 2 2 3 3 0 0 ;+y +y -x -x -y -y +x +x ;
z-store after t1
ph8 = 3 3 0 0 1 1 2 2 ;-y -y +x +x +y +y -x -x ; read
out after z-filter
ph10= 0 ;+x ; 1H CP
ph12=0 2 1 3 2 0 3 1 0 0 1 1 2 2 3 3
2 1 2 3 0 3 0 1 0 1 2 1 2 3 0 3
3 2 1 2 3 0 3 0 1 0 1 2 1 2 3 0
3 0 2 1 3 2 0 3 1 0 0 1 1 2 2 3

ph13=0 0 1 1 2 2 3 3 0 2 1 3 2 0 3 1
0 1 2 1 2 3 0 3 2 1 2 3 0 3 0 1
1 0 1 2 1 2 3 0 3 2 1 2 3 0 3 0
1 0 0 1 1 2 2 3 3 0 2 1 3 2 0 3

ph14=2 0 3 1 0 2 1 3 2 2 3 3 0 0 1 1
0 3 0 1 2 1 2 3 2 3 0 3 0 1 2 1
1 0 3 0 1 2 1 2 3 2 3 0 3 0 1 2
1 2 0 3 1 0 2 1 3 2 2 3 3 0 0 1

ph15=2 2 3 3 0 0 1 1 2 0 3 1 0 2 1 3
2 3 0 3 0 1 2 1 0 3 0 1 2 1 2 3
3 2 3 0 3 0 1 2 1 0 3 0 1 2 1 2
3 2 2 3 3 0 0 1 1 2 0 3 1 0 2 1

;ph12=+x -x +y -y -x +x -y +y +x +x +y +y -x -
x -y -y ; 180deg for "spin lock" ; -x +y -x -y +x -y
+x +y +x +y -x +y -x -y +x -y ; -y -x +y -x -y +x -y
+x +y +x +y -x +y -x -y +x ; 2nd line shifted by one
; -y +x -x +y -y -x +x -y +y +x +x +y +y -x -x -y ;

```

```

1st line shifted by one
;ph13=+x +x +y +y -x -x -y -y +x -x +y -y -x +x -y
+y ; switch 1st 8 with 2nd 8 ; +x +y -x +y -x -y +x
-y -x +y -x -y +x -y +x +y ; +y +x +y -x +y -x -y +x
-y -x +y -x -y +x -y +x ; +y +x +x +y +y -x -x -y -y
+x -x +y -y -x +x -y
;ph14=-x +x -y +y +x -x +y -y -x -x -y -y +x +x +y
+y ; = -ph12 ; +x -y +x +y -x +y -x -y -x -y +x -y +x
+y -x +y ; +y +x -y +x +y -x +y -x -y -x -y +x -y +x
+y -x ; +y -x +x -y +y +x -x +y -y -x -x -y -y +x +x
+y
;ph15=-x -x -y -y +x +x +y +y -x +x -y +y +x -x +y
-y ; = -ph13 ; -x -y +x -y +x +y -x +y +x -y +x +y -x
+y -x -y ; -y -x -y +x -y +x +y -x +y +x -y +x +y -x
+y -x ; -y -x -x -y -y +x +x +y +y -x +x -y +y +x -x
+y
ph31= 0 2 1 3 2 0 3 1

```

RFDR

```

"d2=1s/(cnst31*2)-p1" #ifdef hahnecho "d4=(1s*14/cnst31)-
p1"
"d7=d4-l5*dw" #endif "d5=(1s*11/cnst31)-p1/2.0"
"p2=2*p1"
"l30=td1/l31" "l6=d6/(2*d2+p2)"

1 ze
10u p11:f1
2 (p1 ph20):f1 ; saturation loop
13m
(p1 ph21):f1
7m
(p1 ph22):f1
1m
(p1 ph23):f1
3m
lo to 2 times 8
d1 rpp10
p1 ph1
d0

```

```
p1 ph2
d5
3 d2
p2 ph10^
d2
lo to 3 times l6
d5
3u trigne1
p1 ph3
#ifdef hahnecho
d4
p2 ph4
d7
#endif hahnecho
go=2 ph31
100m wr #0 if #0
zd
```

```
3m ip1
lo to 2 times l31
1m id0
lo to 2 times l30
exit

ph1 = 0 0 0 0 2 2 2 2
ph2 = 0
ph3 = 0 1 2 3
ph4 = 1 2 3 0
ph10= 0 1 0 1 1 0 1 0
ph31= 0 1 2 3 2 3 0 1
ph20= 0 1 2 3
ph21= 1 2 3 0
ph22= 2 3 0 1
ph23= 3 0 1 2
```


List of Figures

2.1	Energy level diagram	8
2.2	Theoretical ^2H static NMR line shape	11
2.3	The single-pulse experiment	13
2.4	Hahn spin echo and solid echo sequence	14
2.5	The cross-polarization experiment	15
2.6	^1H NMR spectra of variable temperature measurement	17
2.7	Basic structure of a multiple-quantum experiment.	19
2.8	Pulse sequence of a BaBa experiment.	20
2.9	Schematic representation of a two-dimensional rotor-synchronised BABA spectrum	21
2.10	Principles of recoupling using a pulse train	22
2.11	Pulse sequences for heteronuclear correlation spectra based on REDOR	23
3.1	Schematic picture of a PEM fuel cell.	26
4.1	Different geometrical structures of the investigated ionomers.	38
4.2	Macroscopic proton conductivity of the ionomers at dry conditions	40
4.3	Macroscopic proton conductivity of the ionomers at 1 bar RH	41
4.4	^1H solid-state MAS NMR spectra of ionomers	45

4.5	Comparison of ^1H DQF MAS NMR spectra at variable temperature . . .	47
4.6	Comparison of ^1H DQF MAS NMR spectra at variable temperature . . .	48
4.7	VT ^1H MAS NMR spectra of HEXAGON and SCREW	49
4.8	^1H VT NMR spectra of TRIANGLE and TETRAHEDRON	51
4.9	VT ^1H MAS NMR spectra of LINE and SQUARE	52
4.10	ARRHENIUS plot to obtain the E_A of the ionomers	53
4.11	Water uptake graph of the HEXAGON.	56
4.12	Comparison of the ^1H and the ^{31}P MAS NMR spectra of HEXAGON . . .	58
4.13	VT ^1H and ^{31}P MAS NMR spectra of HEXAGON stored at 100%RH . . .	59
4.14	^1H VT NMR spectra of HEXAGON stored at ambient conditions and E_A .	60
4.15	Comparison of ^1H and ^2H MAS NMR of the HEXAGON	63
4.16	Static deuterium spectra of the HEXAGON	64
4.17	^2H MAS NMR spectra at slow spinning speed of the HEXAGON	65
4.18	^{31}P liquid NMR spectra of all ionomers	67
4.19	^{31}P solid-state MAS NMR spectra of the LINE and the HEXAGON	68
4.20	^{31}P MAS NMR of the different geometrical structures	69
4.21	^{31}P MAS NMR behavior of the HEXAGON under wet conditions.	71
4.22	TGA and ^{31}P MAS NMR behavior of the HEXAGON	72
4.23	Anhydride and free phosphoric acid formation shown for PhPA	73
4.24	VT ^{31}P static NMR spectra of the HEXAGON and SQUARE	74
4.25	^{31}P static NMR spectra of the LINE and SQUARE at different RH	75
4.26	Filament extrusion WAXS data from the HEXAGON	76
4.27	2D WAXS powder pattern data from the SCREW and the SQUARE	77

4.28	Comparison of the X-ray data of the HEXAGON	78
4.29	Possible crystal structure of the HEXAGON obtained from calculation . . .	79
4.30	^1H and DQF MAS NMR of SQUARE at different temperatures.	81
4.31	DSC and ^1H MAS NMR of SQUARE at 110°C	82
4.32	WAXS powder spectra of the SQUARE before and after annealing	83
4.33	NICS map of the SQUARE.	84
4.34	$^{13}\text{C}\{^1\text{H}\}$ CP and ^{31}P MAS NMR spectra of the SQUARE and SCREW before and after annealing	85
4.35	3D structure of the SCREW in the gas phase	86
4.36	^{31}P NMR SUPER spectrum of the SCREW	88
4.37	^{31}P NMR RFDR spectra of the SCREW	89
4.38	^1H solid-state MAS NMR spectra of LINE and SQUARE.	91
4.39	NICS maps of the HEXAGON and the TRIANGLE.	92
4.40	^1H solid-state MAS NMR spectra of TRIANGLE and HEXAGON	93
4.41	2D DQF spectrum of the LINE.	95
4.42	Double quantum filtered 2D spectra of the SQUARE.	96
4.43	2D DQF spectra of the TRIANGLE and the SCREW.	98
4.44	3D structure of the LINE.	99
4.45	^{13}C CP MAS and REPT-HSQC solid-state NMR spectra of LINE	100
4.46	$^{13}\text{C}\{^1\text{H}\}$ CP MAS and REPT-HSQC NMR spectra of the HEXAGON . . .	101
4.47	^{13}C REPT-HSQC MAS solid-state NMR spectra of SCREW and SQUARE	103
4.48	REPT-HDOR fit of the ionomers	106
4.49	Drawn spacer concept	110

4.50	$^{13}\text{C}\{^1\text{H}\}$ CP MAS NMR spectra of PVPA, PE21-PA, PE9-PA, PE21-Me, PE9-Me and PE	114
4.51	^1H MAS NMR of different PA containing polymers	116
4.52	Arrhenius plot of PE9-PA and PE21-PA.	117
4.53	Variable temperature experiment for PV9-PA and PV21-PA	118
4.54	Double quantum - single quantum correlation experiment	120
4.55	Double quantum - single quantum correlation experiment	121
5.1	Overview of the investigated proton conducting systems.	127
A.1	^1H solid-state MAS NMR spectra of SCREW and TETRAHEDRON	131
A.2	2D DQF spectra of the HEXAGON.	132
A.3	TGA measurement of the SQUARE and the SCREW	132
A.4	Conductivity measurements of the SQUARE at humid and dry conditions. .	133

List of Tables

3.1	Overview of different fuel cells	27
3.2	Mobility of cations in aqueous solution and ion diameter.	30
4.1	Abbreviation for ionomers	36
4.2	Activation energy and chemical shift values	52
4.3	$^{13}\text{C}\{^1\text{H}\}$ REPT-HDOR results for the CH protons in the ionomers	105
4.4	List of the investigated polymers including their abbreviation due to the spacer extended poly(vinylphosphonic acid).	111
4.5	Glass transition T_g , melting point T_m and electronegativity EN of the different polymers	115
B.1	Lamor frequencies for measured nuclei	136
B.2	Reference substances for solid-state NMR spectroscopy	136

Bibliography

- [AFFOUNE 05] Affoune, A. M.; Yamada, A.; Umeda, M.; *J. of Power Sources* **2005**, *1484*, 9-17
- [AGMON 95] Agmon, N.; *Chem. Phys. Let.* **1995**, *244*, 456-462
- [AKBEY 08] Akbey, Ü.; Graf, R.; Peng, Y. B., Chu P. P.; Spiess, H. W.; *J. Polym. Science Part B* **2008**, *47*, 138-155
- [AKBEY 09] Akbey, Ü.; Granados-Focil, S.; Coughlin, E. B.; Graf, R.; Spiess, H. W.; *J. Phys. Chem. B* **2009**, *113*, 9151-9160
- [ALAMO 08] Alamo, R. G.; Jeon, K.; Smith, R. L.; Boz, E. Wagener, K. B.; Bockstaller, M. R.; *Macromolecules* **2008**, *41*, 7141-7151
- [ANDREW 58] Andrew, E. R.; Bradbury, A.; Bades, R. G. *Nature* **1958**, *182*, 1659
- [ASENSIO 05] Asensio, J. A.; Gomez-Romero, P.; *Fuel Cells* **2005**, *3*, 336-344
- [AUE 84] Aue, W. P.; Roufousse, A. H.; Glimcher, M. J.; Griffin, R. G.; *Biochemistry* **1984**, *23*, 6110-6114
- [BAUGHMAN 07] Baughman, T. W.; Chan, C. D.; Winey, K. I.; Wagener, K. B.; *Macromolecules* **2007**, *40*, 6564-6571
- [BENNETT 92] Bennett, A. E.; Ok, J. H.; Griffin, R. G.; Vega, S.; *J. Chem. Phys.* **1992**, *986*, 8624-8627
- [BENNETT 95] Bennett, A. E.; Rienstra, C. M.; Auger, M.; Lakshmi, V. K.; Griffin, R. G.; *J. Chem. Phys.* **1995**, *103*, 6951-6958
- [BERGLUND 80] Berglund, B.; Vaughan, R. W.; *J. Chem. Phys.* **1980**, *73*, 2037-2043
- [BERNAL 33] Bernal, J. D.; Fowler, R. H.; *J. Chem. Phys.* **1933**, *1*, 515-547
- [BINGOEL 06] Bingoel, B.; Meyer, W. H.; Wagner, M.; Wegner, G.; *Macromol. Rapid Commun.* **2006**, *27*, 1719-1724
- [BINGOEL 07] Bingoel, B.; *Dissertation* **2007**, Mainz
- [BISCHOFF 06] Bischoff, M.; *J. of Power Sources* **2006**, *160*, 842-845
- [BLOCH 46] Bloch, F.; *Phys. Rev.* **1946**, *70*, 460-474

- [BOFFA 00] Boffa, L. S.; Novak, B. M.; *Chem. Rev.* **2000**, *100*, 1479-1493
- [BOLUFER 08] Bolufer, P.; *Energia* **2008**, *204*, 72-77
- [BROECK 93] Van den Broeck, H.; *Fuel Cell Syst.* **1993**, *245*
- [BROWN 01] Brown, S. P.; Spiess, H. W.; *Chem. Rev.* **2001**, *101*, 4125-4155
- [BROWN 07] Brown, S. P.; *Prog. in Nucl. Magn. Reson. Spectr.* **2007**, *59*, 199-251
- [BRUNKLAUS 09] Brunklaus, G.; Schauff, S.; Markova, D.; Klapper, M.; Müllen, K.; Spiess, H. W.; *J. Phys. Chem. B* **2009**, *113*, 6674-6681
- [BRUNNER 98] Brunner, E.; Sternberg, U.; *J. Phys. Chem. B* **1998**, *23*, 21-57
- [BUELL 36] Büll, R.; *Angew. Chem.* **1936**, *49*, 145-158
- [CARETTE 01] Carette, L.; Friedrich, K. A.; Stimming, U.; *Fuel Cells* **2001**, *1*, 5-39
- [CHESNUT 05] Chesnut, D. B.; *J. Phys. Chem. A* **2005**, *109*, 11962-11966
- [COLE 41] Cole, K. S.; *J. Chem. Phys* **1941**, *9*, 341-351
- [CONWAY 64] Conway, B. E.; *Modern aspects of electrochemistry* **1964**, Vol. 3, eds. Bockris, J. O'M.; Conway, B. E.; Butterworths, London, 43ff
- [DENSMORE 05] Densmore, C. G.; Rasmussen, P. G.; Goward, G. R.; *Macromolecules* **2005**, *38*, 416-421
- [DITCHFIELD 74] Ditchfield, R; *Mol. Phys.* **1974**, *27*, 789-807
- [DRACINSKY 09] Dracinsky, M.; Kaminsky, J.; Bour, P.; *J. Phys. Chem. B* **2009**, *113*, 14698-14707
- [DZIEMBOWSKA 01] Dziembowska, T.; Rozwadowski, Z.; *Cur. Org. Chem.* **2001**, *5*, No.3
- [DUER 04] Duer, M. J.; *Introduction into Solid State NMR Spectroscopy* **2004**, *1*, Blackwell,
- [EIGEN 64] Eigen, M.; *Ang. Chem. Intern.* **1964**, *3*, 1-19
- [ERNST 87] Ernst, R. R.; Bodenhausen, G.; Wokaun, A.; *Principles of Nuclear Magnetic Resonance in One and Two dimensions.* Clarendon Press, Oxford **1987**
- [FEIKE 96] Feike, M.; Demco, D. E.; Graf, R.; Gottwald, J.; Hafner, S.; Spiess, H. W. ; *J. Magn. Reson. A.* **1996**, *122*, 214-221
- [FISCHER 04] Fischer, M.; Lieser, G.; Rapp, A.; Schnell, I.; Mamdouh, W.; De Feyter, S.; De Schryver, F. C.; Höger, S.; *J. Am. Chem. Soc.* **2004**, *126*, 214-222
- [FONTANELLA 98] Fontanella, J. J.; Wintersgill, M. C.; Wainright, J. S.; Savinell, R. F.; Litt, M.; *Electrochimica Acta* **1998**, *43*, 1289-1294
- [FUNKE 86] Funke, K.; *Solid State Ionics* **1986**, *18*, 183-190
- [FREY 01] Frey, P. A.; *Magn. Reson. Chem.* **2001**, *39*, S190-S198
- [FUNKE 90] Funke, K.; Hoppe, R.; *Solid State Ionics* **1990**, *40*, 200-204

- [GAJDA 08] Gajda, J.; Olejniczak, S.; Bryndal, I.; Potrzebowski, M. J.; *J.Phys. Chem.* **2008**, *112*, 14036-14044
- [GARROW 98] Garbow, J. R.; Goetz, J.; Asrar, J.; *Macromolecules* **1998**, *31*, 3925-3930
- [GERVAIS 04] Gervais, C.; Profeta, M.; Lafond, V.; Bonhomme, C.; Azais, T.; Mutin, H.; Pickard, C. J.; Mauri, F.; Babonneau, F.; *Magn. Reson. Chem.* **2004**, *42*, 445-452
- [GOLUBEV 09] Golubev, N. S.; Dtering, C.; Smirnov, S. N.; Shenderovich, I. G.; Denisov, G. S.; Limbach, H.-H.; Tolstoy, P. M.; *Phys. Chem. Chem. Phys.* **2009** *11*, 5154-5159
- [GOMES 01] Gomes, J. A. N. F.; Mallion, R. B.; *Chem. Rev.* **2001** *101*, 1349-1384
- [GOWARD 02] Goward, G. R.; Schuster, M. F. H.; Sebastiani, D.; Schnell, I.; Spiess, H. W.; *J. Phys. Chem. B* **2002** *112*, 14036-14044
- [GREIN 02] Grein, F.; *J.Phys. Chem. A* **2002**, *106*, 3823-3827
- [GROT 75] Grot, W.; *Chem. Ing. Tech.* **1975**, *47*, 617-618
- [GROTTHUSS 06] Grotthuss, C. J. T; *Ann. Chim.* **1906**, *58*, 54-73
- [GULLION 89] Gullion, T.; Schaefer, J.; *J. Magn. Reson.* **1989**, *81*, 196-200
- [GUARAU 00] Guarau, V.; Barbir, F.; Liu, H.; *J. Electrochem. Soc.* **2000**, *147*, 2468-2477
- [GRAF 07] Graf, R.; Ewen, B.; Spiess, H. W.; *J. Chem. Phys.* **2007**, *126*, 041104-1
- [HAHN 50] Hahn, E. L.; *Physical Review* **1950**, *80*, 580-594
- [HALGREN 96] Halgren, T. A.; *J. Comp. Chem.* **1996**, *17*, 490-519
- [HARRIS 88] Harris R. K.; Jackson, P.; Lawrence, H. M.; Say, B. S.; Hägele, G.; *J. Chem. Soc. Faraday Trans 1* **1988**, *84*, 3649-3672
- [HARRIS 89] Harris, R. K; Merwin, L. H.; Hägele, G.; *J. Chem. Soc. Faraday Trans 1* **1989**, *85*, 1409-1423
- [HARRIS 01] Harris, R. K; Becker, E. D.; Cabral de Menezes, S. M.; Goodfellow, R.; Granger, P.; *Pure Appl. Chem.* **2001**, *73*, 1795-1818
- [HARRIS 03] Harris, R. K; Ghi, P. Y.; Hammond, R. B.; Ma, C.-Y.; Roberts, K. J.; *Chem. Commun.* **2003**, 2834-2835
- [HEITNER-WIRGUIN 96] Heitner-Wirguin, C.; *J. Membr. Sci.* **1996**, *120*, 1-33
- [HENTSCHEL 81] Hentschel, R.; Sillescu, H.; Spiess, H. W.; *Polymer* **1981**, *22*, 1516-1521
- [HERZ 03] Herz, H. G.; Kreuer, K. D.; Maier, J.; Scharfenberger, G.; Schuster, M. F. H.; Meyer, W. H.; *Electrochim. Acta* **2003**, *48*, 2165-2171
- [HERZFELD 80] Herzfeld, J.; Berger, A. E.; *J. Chem. Phys.* **1980**, *73*, 6021-6030

- [HESSE 95] Hesse, M.; Meier, H.; Zeeh, B.; *Spektroskopische Methoden in der organischen Chemie* **1995**, *6*, Thieme, Stuttgart
- [HICKNER 04] Hickner, M. A.; Ghassemi, H.; Kim, Y. S.; Einsla, B. R.; McGrath, J. E; *Chem. Rev.* **2004**, *104*, 4587-4612
- [HINOKUMA 01] Hinokuma, K.; Ata, M.; *Chem. Phys. Lett.* **2001**, *341*, 442-446
- [HU 01] Hu, J. Z.; Solum, M. S.; Taylor, C. M. V.; Pugmire, R. J.; Grant, D. M.; *Energy Fuels* **2001**, *15*, 14-22
- [IRONSIDE 07] Ironside, M. S.; Stein, R. S.; Duer, M. J.; *J. Magn. Reson.* **2007**, *188*, 49-55
- [JIANG 08a] Jiang, F.; Kaltbeitzel, A.; Pu, H.; Meyer, W. H.; Wegner, G.; *Macromolecules* **2008**, *41*, 3081-3085
- [JIANG 08b] Jiang, F.; Kaltbeitzel, A.; Fassbender, B.; Brunklaus, G.; Pu, H.; Meyer, W. H.; Spiess, H. W.; Wegner, G.; *Macromol. Chem. Phys.* **2008**, *209*, 2494-2503
- [JIANG 09] Jiang, F.; *Dissertation* **2009**, Mainz
- [JIMÉNEZ 09] Jiménez García, L.; Kaltbeitzel, A.; Pisula, W.; Gutmann, J. S.; Klapper, M.; Müllen, K.; *Angew. Chem. Int. Ed.* **2009**, *48*,
- [JOHANSSON08] Johansson, M. P.; Olsen, J.; *J. Chem. Theory Comput.* **2008**, *4*, 1460-1471
- [JONES06] Jones, K. M. E.; Mahmoudkhani, A. H.; Chandler, B. D.; Shimizu, G. K. H. *CrystEngComm* **2006**, *8*, 303-305
- [KALTBEITZEL 07] Kaltbeitzel, A.; Schauff, S.; Steininger, H.; Bingöl, B.; Brunklaus, G.; Meyer, W. H.; Spiess, H. W.; *Solid State Ionics* **2007**, *178*, 469-474
- [KARIMI 08] Karimi-Varzaneh, H. A.; Carbone, P.; Mueller-Plathe, F.; *J. Chem. Phys.* **2008**, *129*, 154904
- [KEELER 06] Keeler, J.; *Understanding NMR Spectroscopy*, John Wiley & Sons Ltd, West Sussex **2006**
- [KERRES 99] Kerres, J.; Ullrich, A.; Meier, F.; Haring, T.; *Solid State Ionics* **1999**, *125*, 243-249
- [KOBAYASHI 00] Kobayashi, K.; Shirasaka, T.; Horn, E.; Furukawa, N.; *Tetrahedron Letters* **2000**, *41*, 89-93
- [KREUER 96] Kreuer, K.-D.; *Chem. Mater.* **1996**, *8*, 610-641
- [KREUER 98] Kreuer, K.-D.; Fuchs, A.; Ise, M.; Spaeth, M.; Maier, J.; *Electrochim. Acta* **1998**, *43*, 1281-1288
- [KREUER 00] Kreuer, K.-D.; *Solid State Ionics* **2000**, *456*, 136-137
- [KREUER 04] Kreuer, K.-D.; Paddison, S.-J.; Spohr, E.; Schuster, M.; *Chem. Rev.* **2004**, *104*, 4637-4678
- [KUMURA 04] Kumura, M.; *Materials Integration* **2004**, *17*, 17-21
- [LAWS 02] Laws, D. D.; Bitter, H.-M. L.; Jerschow, A.; *Angew. Chem. Int. Ed.* **2002**, *41*, 3096-3129

- [LAZZERETTI 00] Lazzeretti, P.; *Prog. Nuc. Mag. Reson. Spec.* **2000**, *36*, 1-88
- [LEE 07a] Lee, Y.-J.;Bingoel, B.; Murakhtina, T.; Sebastiani, D.; Meyer, W.-H.;Wegner, G.; Spiess, H. W.; *J. Phys. Chem. B* **2007**, *111*, 9711-9721
- [LEE 07b] Lee, Y.-J.; Murakhtina, T.; Sebastiani, D.; Spiess, H. W.; *J. Amer. Chem. Soc.* **2007**, *129*, 12406-12407
- [LETELLIER 98] Letellier, M.; *Magn. Reson. Imaging* **1998**, *16*, 505-510
- [LEVITT 01] Levitt, M.; *Spin Dynamics. Wiley, Weinheim* **2001**,
- [LIU 02] Liu, S-F.; Mao, J-D.; Schmidt-Rohr, K.; *J. Mag. Reson.* **2002**, *155*, 15-28
- [LOWE 59] Lowe, I.; *Phys. Rev. Lett.* **1959**, *2*, 285-287
- [MA 04] Ma, Y.-L.; Wainright, J. S.; Litt, M. H.; Savinell, R. F.; *J. Electrochem. Soc.* **2004**, *151*, A8
- [MACHO 01] Macho, V.; Brombacher, L.; Spiess, H. W.; *Appl. Magn. Res.* **2001**, *20*, 405-432
- [MAHMODUDKHANI 02] Mahmududkhani, A. H.; Langer, V.; *J. Mol. Struct.* **2002**, *609*, 97-108
- [MALY 07] Maly, K. E.; Gagnon, E.; Maris, T.; Wuest, J. D.; *J. Am. Chem. Soc.* **2007**, *129*, 4306-4322
- [MARICQ 79] Maricq, M. M.; Waugh, J. S.; *J. Chem. Phys.* **1979**, *70*, 3300-3316
- [MARION 83] Marion, D.; Wüthrich, K.; *Proteins. Biochem. Biophys. Res. Commun.* **1983**, *113*, 967-974
- [MARION 89] Marion, D.; Ikura, R.; Tschudin, A.; *J. Magn. Res.* **1989**, *85*, 393-399
- [MASSIOT 02] Massiot, D.; Fayon, F.; Capron, M.; King, I.; Le Clavé, S.; Alonso, B.; Durand, J.-O.; Bujoli, B.; Gan, Z.; Hoatson, G.; *Magn. Res. Chem.* **2002**, *40*, 70-76
- [METZ 94] Metz, G.; Xiaoling, W.; Smith, S. O.; *J. Magn. Reson. A.* **1994**, *110*, 219-227
- [MIERZWA 02] Mierzwa, M.; Floudas, G.; Neidhöfer, M.; Graf, R.; Spiess, H. W.; Meyer, W. H.; Wegner, G.; *J. Chem. Phys* **2002**, *117*, 6298-6299
- [MOLOGIN 02] Mologin, D. A.; Khalatur, P. G.; Khokhlov, A. R.; *Macromol. Theory Simul.* **2002**, *11*, 587-607
- [MORKOMBE 03] Morkombe, C. R.; Zilm, K.; *J. Magn. Reson.* **2003**, *162*, 479-486
- [MUNOWITZ 88] Munowitz, M.; *Coherence and NMR* **1988**, John Wiley & Sons
- [MUNSON 64] Munson, R. A.; *J. Phys. Chem.* **1964**, *68*, 3374
- [MUNTEAN 88] Muntean, J. V.; Stock, L. M.; Botto, R. E.; *J. Magn. Reson.* **1988**, *76*, 540-542
- [NARAYANAN06] Narayanan, S. R.; Yen, S.-P.; Liu, L.; Greenbaum, S. G.; *J. Phys. Chem. B* **2006**, *110*, 3942-3948
- [ORR 05] Orr, R. M.; Duer, M. J.; Ashbrook, S. E.; *J. Magn. Reson.* **2005**, *174*, 301-309
- [PADDISON 06] Paddison, S. J.; Kreuer, K. D.; Maier, J.; *Phys. Chem. Chem. Phys.* **2006**, *8*, 4530-4542

- [PAKE 48] Pake, G. E.; *J. Chem. Phys.* **1948**, *16*, 327-336
- [PEREIRA 06] Pereira, R. P.; Felisberti, M. I.; Rocco, A. M.; *Polymer* **2006**, *47*, 1414-1422
- [PERRSON 03] Perrson, J. C.; Jannasch, P.; *Chem. Mater.* **2003**, *15*, 3044-3045
- [PFROMMER 00] Pfrommer, B. G.; Mauri, F.; Louie, S.; *J. Amer. Chem. Soc.* **2000**, *122*, 123-129
- [PINES 73] Pines, A.; Gibby, M. G.; Waugh, J. S.; *J. Chem. Phys.* **1973**, *59*, 569-590
- [PISULA 05] Pisula, W.; Tomovic, Z.; Simpson, C.; Kastler, M.; Pakula, T.; Müllen, K.; *Chemistry of Materials* **2005**, *17*, 4296-4303
- [PURCELL 46] Purcell, E. M.; Torrey, R. V.; Pound, R. V.; *Phys. Rev.* **1946**, *69*, 37-38
- [RADEV 08] Radev, I.; Georgiev, G.; Sinigersky, V.; Salvcheva, E.; *Int. J. Hydrogen Energy* **2008**, *33*, 4849-4855
- [RAGER 07] Rager, T.; Schuster, M.; Steininger, H.; Kreuer, K. D.; *Adv. Mater.* **2007**, *19*, 3317-3321
- [RAPP 03] Rapp, A.; Schnell, I.; Sebastiani, D.; Brown, S. P.; Percec, V.; Spiess, H. W.; *J. Am. Chem. Soc.* **2003**, *125*, 13284-13297
- [RHIM 79] Rhim, W. K.; Burum, D. P.; Elleman, D. D.; *J. Chem. Phys.* **1979**, *71*, 3139-3141
- [RIEDEL 99] Riedel, E.; *Anorganische Chemie* **1999**, *4. Auflage*, 75
- [SAALWÄCHTER 01a] Saalwächter, K.; Spiess, H. W.; *J. Chem. Phys.* **2001**, *114*, 5707-5728
- [SAALWÄCHTER 01b] Saalwächter, K.; Graf, R.; Spiess, H. W.; *J. Magn. Reson.* **2001**, *148*, 398-418
- [SAALWÄCHTER 02] Saalwächter, K.; Schnell, I.; *Solid State Nucl. Magn* **2002**, *22*, 154-187
- [SCHAUFF 07] Schauff, S.; *PhD thesis at Max Planck Institute for Polymer Research* **2007**
- [SCHMIDT 05] Schmidt, J.; *PhD thesis at Max Planck Institute for Polymer Research* **2005**
- [SCHMIDT-ROHR 94] Schmidt-Rohr, K.; Spiess, H. W.; *Multidimensional Solid-State NMR and Polymers. Academic Press, London* **1994**
- [SCHNELL 01] Schnell, I.; Spiess, H. W.; *J. Magn. Reson.* **2001**, *151*, 153-227
- [SCHUSTER 01] Schuster, M. F.; Meyer, W. H.; Wegner, G.; Herz, H. G.; Ise, M.; Kreuer, K. D.; Maier, J.; *Solid State Ionics* **2001**, *145*, 85-92
- [SCHUSTER 05] Schuster, M.; Rager, T.; Noda, A.; Kreuer, K. D.; *Fuel Cells* **2005**, *5*, 355-365
- [SEBASTIANI 05] Sebastiani, D.; *Chem. Phys. Chem.* **2005**, *7*, 164-175
- [SEVIL 04] Sevil, F.; Bozkurt, A.; *J. Phys. Chem. Solid* **2004**, *65*, 1659-1662
- [SHOJI 89] Shoji, A.; Ozaki, T.; Fujito, T.; Deguchi, K.; Ando, S.; Ando, I.; *Macromolecules* **1989**, *22*, 2860-2863
- [SPIESS 81] Spiess, H. W.; Sillescu, H.; *J. Magn. Reson.* **1981**, *42*, 381-389

- [SPIESS 85] Spiess, H. W.; *Adv. Polym. Sci.* **1985**, *66*, 23-58
- [STEININGER 07] Steininger, H.; Schuster, M.; Kreuer, K. D.; Kaltbeitzel, A.; Bingol, B.; Meyer, W. H.; Schauff, S.; Brunklaus, G.; Maier, J.; Spiess, H. W.; *Phys. Chem. Chem. Phys.* **2001**, *9*, 1764-1773
- [TUCKERMAN 97] Tuckermann, M. E.; Marx, D.; Klein, M. L.; Parinello, M.; *Science* **1997**, *275*, 817
- [TYCKO 89] Tycko, R.; Dabbagh, G.; Mirau, P.; *J. Magn. Reson.* **1989**, *85*, 265
- [WALRAFEN 86] Walrafen, G. E.; Fischer, M. R.; Hokmabadi, M. S.; Yang, W.-H.; *J. Chem. Phys.* **1986**, *85*, 6970-6982
- [WATSON 01] Watson, M. D.; Fechtenkötter, A.; Müllen, K.; *Chem. Rev.* **2001**, *101*, 1267-1300
- [WAUGH 56] Waugh, J. S.; Fessenden, R. W.; *J. Am. Chem. Soc.* **1956**, *79*, 846-
- [WEAKLEY 76] ; Weakley, T. J. R.; *Acta Crystallo., Sect. B: Struct. Crystallogr. Cryst. Chem.* **1976**, *32*, 2889-2890
- [WEBER 08] Weber, J.; Kreuer, K.-D.; Maier, J.; Thomas, A.; *Adv. Mater.* **2008**, *20*, 2595-2598
- [WEI 09] Wei, Y.; Graf, R.; Sworen, J. C.; Cheng, C.-Y.; Bowers, C. R.; Wagener, K. B.; Spiess, H. W.; *Angew. Chem. Int. Ed.* **2009**, *48*, 4617-4620
- [WIND 01] Wind, M.; Wiesler, U.-M.; Saalwächter, K.; Müllen, K.; Spiess, H. W.; *Adv. Mater.* **2001**, *13*, 752-756
- [WINTER 04] Winter, M.; Brodd, R. J.; *Chem. Rev.* **2004**, *104*, 4245-4269
- [XIAO 05] Xiao, L.; Zhang, H.; Choe, E. W.; Rogers, D.; Apple, T.; Benicewicz, B. C. ; *Chem. Mater.* **2005**, *17*, 5328-5333
- [YAMADA 06] Yamada, M.; Honma, I.; *Chem Phys. Lett.* **2006**, *402*, 324-328
- [YAMAUCHI 00] Yamauchi, K.; Kuroki, S.; Fujii, K.; Ando, I.; *Chem Phys. Lett.* **2000**, *324*, 435-439
- [YAO 07] Yao, Y.-F.; Graf, R.; Spiess, H. W.; Lippits, D. R.; Rastogi, S.; *Phys. Rev. E* **2007**, *76*, 060801
- [YE 06] Ye, G.; Nanzen, N.; Goward, G. R.; *Macromolecules* **2006**, *39*, 3283-3290
- [YOZA 94] Yoza, N.; Ueda, N.; Nakashima, S.; *Fresenius J. Anal. Chem.* **1994**, *348*, 633-638
- [ZUNDEL 86] Zundel, G.; Fritsch, J.; *The chemical physics of solvation* **1986**, Vol. 2, eds. Dogonadze, R. R.; Kálmán, E.; Kornyshev, A. A.; Ulstrup, J.; Elsevier, Amsterdam

